Multiscale modeling of metal-organic frameworks

Heinen, J.

Publication date
2018

Document Version
Final published version

License
Other

Link to publication

Citation for published version (APA):
Heinen, J. (2018). *Multiscale modeling of metal-organic frameworks*. [Thesis, fully internal, Universiteit van Amsterdam].

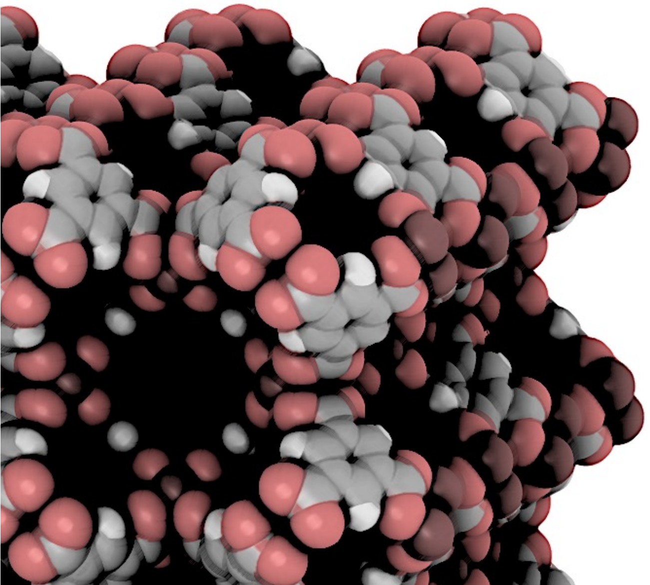

MULTISCALE MODELING OF METAL-ORGANIC FRAMEWORKS

Jurn Heinen

MULTISCALE MODELING OF METAL-ORGANIC FRAMEWORKS

Jurn Heinen

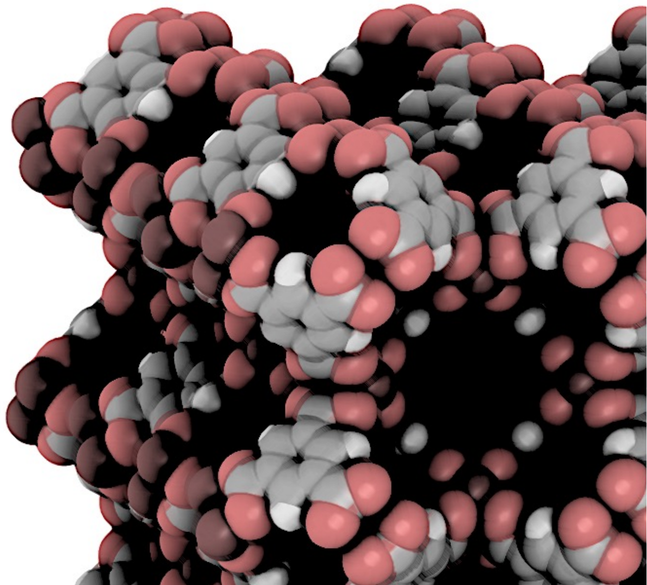

Multiscale modeling of metal-organic frameworks

ACADEMISCH PROEFSCHRIFT

ter verkrijging van de graad van doctor
aan de Universiteit van Amsterdam
op gezag van de Rector Magnificus
prof. dr. ir. K.I.J. Maex
ten overstaan van een door het College voor Promoties ingestelde commissie,
in het openbaar te verdedigen in de Agnietenkapel

op dinsdag 16 oktober 2018, te 14.00 uur

door

Jurn Heinen

geboren te Amsterdam

Promotiecommissie

Promotor:	prof. dr. E.J. Meijer	Universiteit van Amsterdam
Copromotor:	dr. D. Dubbeldam	Universiteit van Amsterdam
Overige leden:	prof. dr. P.G. Bolhuis	Universiteit van Amsterdam
	prof. dr. B. de Bruin	Universiteit van Amsterdam
	dr. N.C. Burtch	Sandia National Laboratories
	prof. dr. C. Fonseca Guerra	Vrije Universiteit Amsterdam
	dr. S. Grecea	Universiteit van Amsterdam
	prof. dr. ir. T.J.H. Vlugt	Technische Universiteit Delft
	prof. dr. K.S. Walton	Georgia Institute of Technology

Faculteit der Natuurwetenschappen, Wiskunde en Informatica
Amsterdam Center for Multiscale Modeling

The work described in this thesis was financially supported by the Netherlands Research Council for Chemical Sciences (NWO-CW) through a VIDI grant (Dr. D. Dubbeldam). SURFSARA (The Dutch Foundation of Computer Facilities) is kindly acknowledged for the use of supercomputer facilities. This work was carried out at the Van 't Hoff Institute for Molecular Sciences, University of Amsterdam. Part of this work was conducted at the Georgia Institute of Technology and Sandia National Laboratories.

ISBN: 978-94-028-1163-6
Cover illustration: Van der Waals representation of HKUST-1

"*That's what I do: I drink and I know things.*"
Tyrion Lannister

Contents

List of Symbols

Latin symbols	
a	lattice parameter
A_c	area function of indenter tip
B_0	bulk modulus
c_j	coefficients of basis function
C_t	heat capacity at constant stress
$\mathcal{C}_{ij}$	elastic tensor in Voigt notation
$\mathcal{D}_s$	self-diffusivity
e	elementary charge
E	Young's modulus
E'	storage modulus
E''	loss modulus
f_s	total force of the system
f	fugacity
f_i	force acting on particle i
F	Helmholtz free energy
$\boldsymbol{F}$	deformation gradient
G	shear modulus
$\boldsymbol{G}$	reciprocal lattice vectors
h	Planck's constant
$\hbar$	reduced Planck's constant
h_c	displacement of indenter tip
$\boldsymbol{h}$	transformation matrix
$\hat{\mathscr{H}}$	electronic and nuclear Hamiltonian
$\hat{\mathscr{H}}_e$	electronic Hamiltonian
$\hat{\mathscr{H}}_{\mathsf{HVD}}$	Heisenberg-Vleck-Dirac Hamiltonian

$\mathcal{H}_{ij}$	Hessian
$\mathcal{H}_g$	generalized Hessian
$\mathcal{H}$	classical Hamiltonian
H	hardness
I	indentation modulus
J	magnetic coupling constant
k_B	Boltzmann constant
$\boldsymbol{k}$	reciprocal wave-vector
K_i	Langmuir constant
m_i	mass of particle i
m_e	mass of electron
M_I	mass of nuclei I
M_s	spin quantum number
n_d	number of degrees of freedom
n_i	heterogeneity index
N	number of particles
$\boldsymbol{p}_i$	generalized momenta of particle i
p	pressure
P	applied load of indenter tip
$\mathcal{P}$	probability density function
$\boldsymbol{q}_i$	generalized position of particle i
$\tilde{\boldsymbol{q}}_i$	reference generalized position of particle i
q	loading
q_i	partial atomic charge of particle i
Q_x	partition function in the x-ensemble
$\boldsymbol{r}_i$	Cartesian position of particle i
R	Ray potential
$\boldsymbol{s}_i$	fractional position of particle i
S_{BET}	BET surface area
S	entropy
$\mathcal{S}_{ij}$	elastic compliance in Voigt notation
t	time
T	temperature
u_{ij}	pair interaction potential
$\mathcal{U}$	internal energy
v_i	velocity of particle i
v_{ext}	external potential due to nuclei
v_{XC}	functional derivative of exchange-correlation functional
V	unit cell volume
Z_I	nuclear charge

Greek symbols

α_l	linear coefficient of thermal expansion
α_V	volumetric coefficient of thermal expansion

β	inverse temperature
β_c	linear compressibility
β_g	geometric constant for indenter tip
γ	Grüneisen parameter
Γ	irreducible representation
δ	phase shift
δ_{ij}	Kronecker delta
Δt	time-step in MD-simulation
ϵ_i	Lagrangian strain
ϵ_{ij}	effective-interaction Lennard-Jones parameter
ϵ_0	electric permittivity of vacuum
ε	energy density of overall molecule
ε_i	energy density of fragment i
λ	order parameter
λ_i	eigenvalue of elastic tensor
Λ	thermal de Broglie wavelength
μ	chemical potential
ν	Poisson's ratio
π	spreading pressure
ρ_e	electron density
ρ	particle density
σ_i	Cauchy stress
σ_{ij}	effective-size Lennard-Jones parameter
χ	Slater-type orbital
ψ_i	electronic wavefunction
Ψ	nuclear and electronic wavefunction
Ω	osmotic potential

General introduction

Metal-organic frameworks

In 2016 Sholl and Lively highlighted seven chemical separations, which upon improving would lead to great global benefits.[1] Examples of these separations are hydrocarbons from crude oil, uranium from seawater, alkenes from alkanes and greenhouse gases from dilute emissions. About 10-15% of the world's energy consumption is due to the separation of these type of industrial mixtures,[2,3] whereby 90% of these industrial separations are performed by means of expensive distillation techniques.[4] Clearly, these numbers illustrate the need for alternative, energy-efficient, separation methods. A very promising method is adsorptive separation.

In adsorptive separation, a N-component mixture is passed over a packed bed containing nanoporous crystallites, which act as a sorbent material. One component of the mixture will adsorb better than the others. When the sorbent is saturated, the inward flow is stopped and the bed is replaced or regenerated. Regeneration of the sorbent occurs via temperature or pressure-induced desorption.[5]

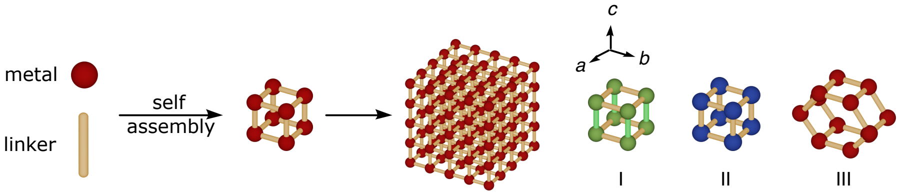

Figure 1: *Metal-organic frameworks consist of organic linkers and metals that through the process of self-assembly form crystalline nanoporous materials. The chemical diversity can be substantial due to modification of: I) linkers, II) metals and III) topology.*

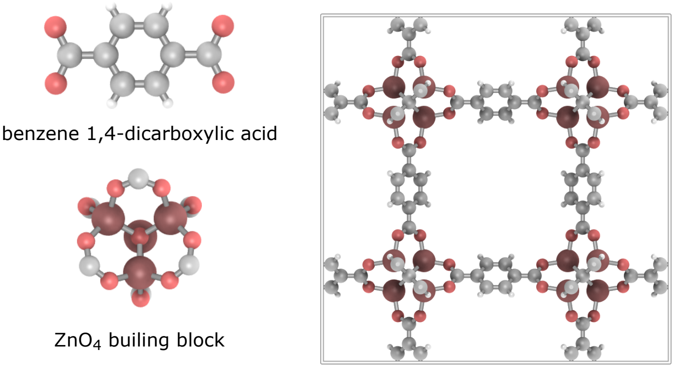

Figure 2: *IRMOF-1, first reported in 1999, consists of Zn_4O units interconnected by benzene 1,4-dicarboxylate linkers with lattice parameter a = 25.832 Å.*[9] *Color legend: C (gray), O (red), H (white), Zn (brown).*

One of the challenges in designing these so-called *pressure/temperature swing adsorption* processes is the choice of the crystallites. For a long time, zeolites have been considered and used as sorbent materials.[4] About two decades ago, a new class of nanoporous materials has emerged, which are known as porous coordination polymers or *metal-organic frameworks* (MOFs).[6–8]

MOFs consist of metal nodes interconnected by organic linker molecules that self-assemble into a crystalline material as shown schematically in Figure 1. For example, benzene 1,4-dicarboxylic acid (BDC) and zinc nitrate hydrate dissolved in dimethylformamide (DMF) produce the isoreticular metal-organic framework IRMOF-1 as shown in Figure 2.[9] IRMOF-1 is a cubic MOF that crystallizes into space group $Fm\bar{3}m$ with a lattice parameter of a = 25.6990 Å and a Brunauer-Emmett-Teller (BET) surface area of $S_{\mathrm{BET}} = 3800\ \mathrm{m}^2/\mathrm{g}$.[10] Given the large variety of metals found in the periodic table and a diverse selection of organic linkers, the amount of possible MOF structures is enormous. Recently, 137.953 hypothetical structures have been generated of which 300 have excellent methane-storage capacity.[11] Also, high-throughput screening of 4700 experimental structures was used for assessing methane adsorption.[12] Based on this large versatility, it is argued that it should be possible to 'design' a MOF for certain applications by, for example, functionalization of the organic linkers with substituents.[13]

Among the unique features of MOFs are their large pores and high surface area's, which make MOFs suitable for separation and storage applications. The current porosity record-holder is NU-110 with a surface area of 7140 m^2/g and a porosity of 93%.[14] For separation processes there is a trade-off to be made between the storage capacity (associated with the pore volume) and the adsorption selectivity, which has led to the development of *entropic* separation mechanisms.[15,16] For example, by exploiting the channel dimensions of MAF-x8, higher adsorption capacities of p-xylene could be obtained compared to the commercially-used BaX due

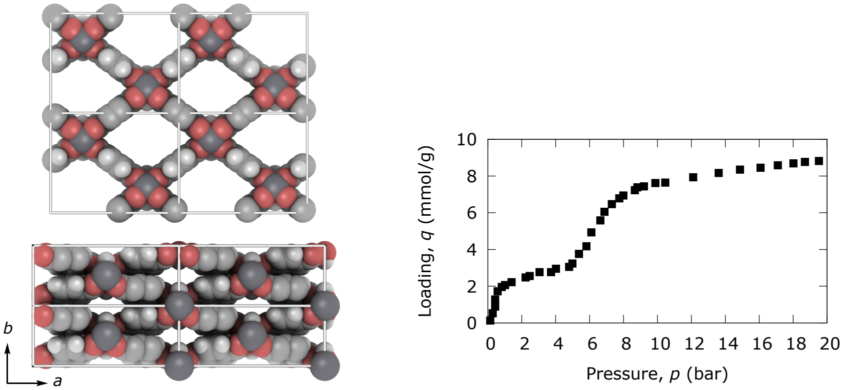

(a) **(b)**

Figure 3: *MIL-53(Cr) exhibits a phase transition upon CO_2 adsorption. (a) Unit cells (2 x 2 x 1) of MIL-53(Cr) along the c-direction with the large pore phase (top, V = 1486.14 Å^3) and the narrow pore phase (bottom, V = 1012.64 Å^3). Color legend: C (light gray), O (red), H (white), Cr (dark gray). (b) Experimental CO_2 adsorption isotherm.*[28]

to commensurate stacking.[17] More recently, sol-gel monolithic HKUST-1 reached a methane storage capacity of 259 cm^3 (STP) cm^{-3} at room temperature and 65 bar, in close agreement with the US Department of Energy (DOE) volumetric storage target of 263 cm^3 (STP) cm^{-3}.[18] Besides separation and storage applications, MOFs have also been considered as candidate materials for other applications including, but not limited to, catalysts,[19] drug delivery[20] and sensor devices.[21]

Intriguingly, some MOFs exhibit exceptional large-scale flexible behavior.[22–24] One of the most illustrative flexible modes is the *breathing* mode in MIL-53(Cr) [$(Cr(OH)(COO_2)_2)_n$-chains connected with BDC-linkers] upon external stimuli as shown in Figure 3a.[25,26] This material undergoes a phase transition from a large pore phase (space group: $Imcm$) to a narrow pore phase (space group: $C12/c1$) upon CO_2 adsorption, associated with a relative change of 32% in the unit cell volume. The opening and closing of the pore causes a distinctive shape of the adsorption isotherm as shown in Figure 3b. This reversible behavior is of particular interest in selective gas adsorption and progressive release of drugs.[27]

Another fascinating consequence of the flexibility of MOFs is *negative thermal expansion* (NTE). Nearly all materials have a positive coefficient of thermal expansion and thus expand upon increasing temperatures.[29] However, most MOFs have a negative coefficient of thermal expansion and thus the unit cell contracts upon heating. HKUST-1 is a typical example of a NTE MOF with a linear coefficient of thermal expansion of $-4.9 \cdot 10^{-6}$ K^{-1}.[30,31] The underlying mechanisms for NTE in HKUST-1 are different from the NTE mechanisms found in condensed matter materials. Several factors have been argued in literature that are important contributions for NTE to occur in HKUST-1: i) translation and ii) libration modes of the organic linker and iii) asymmetric distortions of the metal nodes.[30] Density functional theory (DFT) calculations of a representative distorted paddlewheel-cluster ($Cu_2(O_2C_7H_5)_4$), showed favorable delocalization of the sixth level below the highest-occupied molecular orbital (HOMO-6) and thereby changing the Cu-O distance from 1.9832 Å in the minimum-energy configuration to 1.9818-1.9866 Å in the distorted configuration.[31] More recently, synchrotron far-infrared spectroscopy revealed that low-lying vibrational modes at 58 cm^{-1} (1.7 THz) and 81 cm^{-1} (2.4 THz) might explain the origin of NTE.[32,33]

There is still considerable debate in literature on the origin of these large flexible modes in MOFs. Tensorial analysis of the *ab initio* calculated elastic constants showed large anisotropy and it has been argued to be a major contributor to framework flexibility.[34,35] Single crystal nanoindentations confirmed these theoretical findings for DMF-solvated Zn-DMOF-1 [Zn_2(1,4-BDC)$_2$(DABCO); DABCO = 1,4-diazabicyclo[2.2.2]octane], revealing an anisotropy of 4.5 for the Young's modulus.[36] The elastic constants tensor $\mathcal{C}_{\alpha\beta\mu\nu}$ relates the stress tensor $\sigma_{\alpha\beta}$ to the strain tensor $\epsilon_{\mu\nu}$ within the *Hookean* limit

$$\sigma_{\alpha\beta} = \mathcal{C}_{\alpha\beta\mu\nu}\epsilon_{\mu\nu} \tag{1}$$

where the summation convention is adapted. Greek indices denote Cartesian coordinates ($\alpha = \{x, y, z\}$). The elastic tensor has 81 components but reduces to 36 due to symmetric stress and strain tensors.[37] Depending on the crystal symmetry, the amount of unique components reduces further. For example, an orthorhombic unit cell has nine independent components of the elastic tensor, given in Equation (2).

$$\mathcal{C}_{ij} = \begin{pmatrix} \mathcal{C}_{11} & \mathcal{C}_{12} & \mathcal{C}_{13} & 0 & 0 & 0 \\ \mathcal{C}_{12} & \mathcal{C}_{22} & \mathcal{C}_{23} & 0 & 0 & 0 \\ \mathcal{C}_{13} & \mathcal{C}_{23} & \mathcal{C}_{33} & 0 & 0 & 0 \\ 0 & 0 & 0 & \mathcal{C}_{44} & 0 & 0 \\ 0 & 0 & 0 & 0 & \mathcal{C}_{55} & 0 \\ 0 & 0 & 0 & 0 & 0 & \mathcal{C}_{66} \end{pmatrix} \tag{2}$$

Here, the Voigt notation is adapted ($1 = xx$, $2 = yy$, $3 = zz$, $4 = yz$, $5 = xz$, $6 = xy$).[38] The first three diagonal components of the elastic tensor $\mathcal{C}_{11}$, $\mathcal{C}_{22}$ and $\mathcal{C}_{33}$ represent the stiffness along the principal crystal axes. The other diagonal components $\mathcal{C}_{44}$, $\mathcal{C}_{55}$ and $\mathcal{C}_{66}$ are the shear coefficients that determine the resistance against angular deformation due to shear strain. The off-diagonal components $\mathcal{C}_{12}$, $\mathcal{C}_{13}$ and $\mathcal{C}_{23}$ are the tensile-coupling interactions between two principal axes.

For MOF-materials, the full elastic tensor has only been measured experimentally for ZIF-8 using Brillouin scattering. An extremely low shear modulus of $G_{\text{min}} =$ 0.967 GPa was observed and attributed to cooperative Zn-imidazole-Zn (bridging) and N-Zn-N (tetrahedral) bonding angles.[39] Although, large anisotropy might be crucial for flexible behavior of MOFs, the absolute values, such as the shear modulus in ZIF-8, are small compared to *e.g.*, zeolites. The mechanical properties of

MOFs can be fascinating but also present challenges for their implementation in technological applications.[40–43] Currently, the low mechanical stability of MOF-materials is a key reason that forms an obstacle in their commercialization.[44]

Multiscale modeling

The use of computational techniques (modeling) is nowadays widely accepted in chemistry, physics and materials sciences. In the list of the top 100 most cited scientific articles of all time published in 2014 by *Nature*, 15 out of 100 articles are in the field of computational chemistry/physics.[45] Also, the Chemistry Nobel Prizes awarded to computational chemists in 1998 and 2013, illustrate the impact of computational techniques.[46]

There are various levels of theory for materials modeling, which can be classified in terms of time-scales and length-scales as shown in Figure 4. The smallest time-scale, relevant for chemists and materials scientists, are *electronic structure* calculations, which rely on a quantum mechanical description. A step up the ladder of multiscale modeling are molecular mechanics or *force field* simulations. Here, classical mechanics is applied at the molecular level. Longer time-scales - not discussed in this thesis - are mesoscale (coarse grained) simulations and continuum mechanics simulations.

In Figure 5, two examples are shown of what can be modeled nowadays regarding materials properties and related applications. Figure 5a shows the adsorption isotherm of ethane in HKUST-1 measured experimentally and calculated using grand-canonical Monte Carlo simulations. By visualizing the isotherm in semi-logarithmic scale, the overall shape of the isotherm becomes visible, showing that the energetic-dominated region is captured correctly. Figure 5b shows an *ab initio*

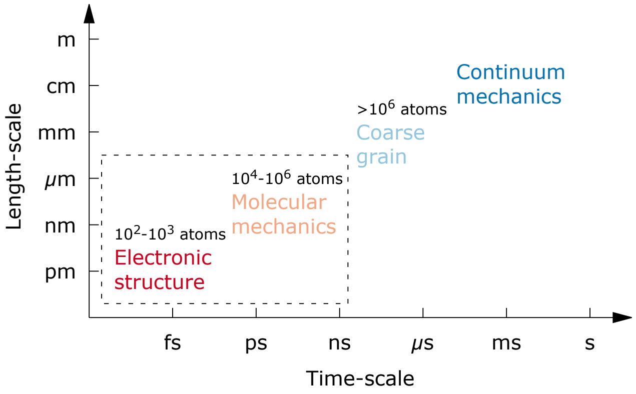

Figure 4: *Length-scale vs. time-scale showing multiscale modeling. In this thesis, electronic structure and molecular mechanics simulations are performed.*

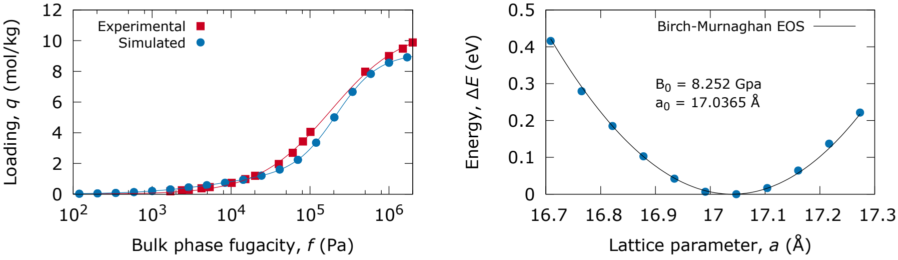

(a) *Adsorption isotherm* **(b)** *Equation of state*

Figure 5: *Materials properties that can be computed using multiscale modeling. (a) Ethane adsorption isotherm in HKUST-1 at 323 K, simulated using grand-canonical Monte Carlo simulations. (b) Birch-Murnaghan energy-volume equation of state for ZIF-8 obtained from density functional theory calculations.*

calculated Birch-Murnaghan equation of state for ZIF-8. The calculated equilibrium lattice parameter of $a = $ 17.0365 Å at 0 K is in good agreement with the experimental lattice parameter of 16.990 Å obtained from neutron diffraction at 3.5 K.[47] The bulk modulus extracted from the equation of state $B_0 = $ 8.252 GPa compares well to 9.2293 GPa and 7.7508 GPa obtained from B3LYP DFT calculations and Brillouin scattering experiments.[39] Table 1 presents various materials properties of ZIF-8 from experiments and simulation. Overall, the agreement between experiment and simulation is good.

Generally, the type of calculations involved in materials modeling requires demanding numerical operations. For this reason, large computer power is needed. To illustrate the type of machinery that is typically used for materials modeling, the processing power of a regular all-day laptop is compared with that of a supercomputer. The computer on which this thesis was mainly written (MacBook Air, Early 2014) is running on an Intel Core i7-4650U (Haswell architecture) with a clock frequency of 1.7 GHz per core and 8 GB internal RAM. Theoretically, this machine, more specifically the processor, has a computer power of 218$\cdot 10^9$ floating points operations per second (flops) and a power consumption of 45 W. The world's most powerful supercomputer according to the Top500.org list, the Summit IBM Power System AC922 (Oak Ridge National Laboratory, Unites States), runs at 122$\cdot 10^{15}$ flops.[48] The amount of power to maintain such a computer cluster is around 8.8 MW (solely the processor, memory, and interconnect network, excluding any cooling systems). This is enough to power a small city of around 6.000 households.[49]

These are exciting times for computational scientists, and science in general, as recent developments in computer science, such as quantum computing and machine learning, have already shown to be applicable in the field of computational chemistry.[51,52]

Table 1: *Lattice parameter a (Å), elastic constants $\mathcal{C}_{ij}$ (GPa) and bulk modulus B_0 (GPa) of ZIF-8 obtained from DFT calculations, experiments and force field calculations. The temperature is denoted in parenthesis. * This work.*

	a	$\mathcal{C}_{11}$	$\mathcal{C}_{12}$	$\mathcal{C}_{44}$	B_0
B3LYP-D (0 K)[39]	17.0630	11.038	8.325	0.943	9.229
PBE-D3 (0 K)*	17.0365	9.484	8.250	2.361	8.252
Brillouin scattering (295 K)[39]	-	9.523	6.865	0.967	7.751
Single crystal (293 K)[50]	16.992	-	-	-	-
Neutron diffraction (3.5 K)[47]	16.990	-	-	-	-
Force field (0 K)*	16.274	10.087	8.578	0.899	9.081

Outline of this thesis

Metal-organic frameworks containing open-metal sites are potential sorbent materials for adsorptive separations of olefin/paraffin mixtures. Therefore, considerable theoretical work exists on the adsorption of guest molecules at the open-metal site. Underlying molecular orbital interactions play a dominant role in these adsorption processes, which can be studied using molecular orbital theory. From knowledge of the electronic interactions, accurate predictions can be made of the multicomponent adsorption behavior of olefin/paraffin mixtures. Although MOFs are promising, their large porosity has consequences regarding their mechanical stability.

The main scope of this thesis is to demonstrate that multiscale modeling is an important tool to study the adsorptive separation and mechanical properties in MOFs. A combination of quantum chemical and classical simulation methodology, complemented with experiments, is used.

In Chapter 2, molecular orbital theory, in the framework of Kohn-Sham DFT is used to elucidate electronic and geometric changes occurring in HKUST-1 upon water adsorption. Various exchange-correlation functionals are compared to assess their performance. Chapter 3 shows that the incorporation of an *ab initio* derived force field potential is crucial to describe the correct multicomponent adsorption behavior as ideal adsorbed solution theory fails. Part of the work described in Chapter 3 was conducted at the Georgia Institute of Technology.

Chapter 4 reviews the state-of-art flexible force fields models specifically developed for MOFs, which form an essential tool to study mechanical properties. In Chapter 5, a new scheme for constructing flexible force fields is presented. Here, force field potentials are fitted on the *ab initio* calculated elastic tensor. Chapter 6 presents, for the first time, experimental work on thermomechanical and creep properties of HKUST-1. The Young's modulus and hardness decrease with increasing temperature. This is consistent with classical molecular dynamics simulations that show a reduced of the isothermal elastic constants. The work reported in Chapter 6 was conducted at Sandia National Laboratories (Livermore).

CHAPTER 1

Computational methodology

The fundamental quantity in quantum mechanics that describes all electronic and nuclear properties of any material is the many-body wavefunction Ψ.[53] The Born interpretation of the wavefunction states that probability density function for a volume element $\mathrm{d}V$ is given by the wavefunction multiplied with its complex conjugate.[54] At the heart of quantum mechanics is the non-relativistic time-independent Schödinger equation[55]

$$\hat{\mathscr{H}}\Psi(\boldsymbol{x_1},\ldots,\boldsymbol{x_N},\boldsymbol{R_1}\ldots,\boldsymbol{R_M}) = E\Psi(\boldsymbol{x_1},\ldots,\boldsymbol{x_N},\boldsymbol{R_1},\ldots,\boldsymbol{R_M}) \tag{1.1}$$

where N is the number of electrons, M the number of nuclei, $\boldsymbol{x}_i$ denotes the spatial coordinates $\boldsymbol{r}_i$ and the spin s_i of the electron and R_I are the positions of the nuclei. The Hamiltonian of such a system is defined according to

$$\begin{aligned}\hat{\mathscr{H}} = \frac{-\hbar^2}{2m_e}\sum_{i}^{N}\hat{\nabla}_i^2 - \sum_{i,I}^{N,M}\frac{Z_I e^2}{|\boldsymbol{r_i}-\boldsymbol{R_I}|} + \frac{1}{2}\sum_{i\neq j}^{N}\frac{e^2}{|\boldsymbol{r_i}-\boldsymbol{r_j}|}\\ -\sum_{I}^{M}\frac{\hbar^2}{2M_I}\hat{\nabla}_I^2 + \frac{1}{2}\sum_{I\neq J}^{M}\frac{Z_I Z_J e^2}{|\boldsymbol{R_I}-\boldsymbol{R_J}|}\end{aligned} \tag{1.2}$$

with $\hbar$ the reduced Planck's constant, subscripts i and I are electron and nuclei indices, respectively, m_e and M_I are the masses of an electron and nuclei, Z_I the formal charge of the nuclei, e the elementary charge and $\hat{\nabla}$ is the gradient operator. Here, the first term is the electron kinetic energy, the second term is the electron-nuclei potential energy, the third term is the electron-electron potential energy, the fourth term is the nuclear kinetic energy and the last term is the nuclei-nuclei potential energy. By invoking the Born-Oppenheimer (BO) principle, it is assumed that the nuclear motion is stationary compared to the electronic motion.[56] As a result, the second-last term of the Hamiltonian drops out and the potential energy between the nuclei becomes constant. The Hamiltonian reduces to the electronic Hamiltonian

$$\hat{\mathscr{H}}_e = \frac{-\hbar^2}{2m_e}\sum_{i}^{N}\hat{\nabla}_i^2 - \sum_{i,I}^{N,M}\frac{Z_I e^2}{|\boldsymbol{r_i} - \boldsymbol{R_I}|} + \frac{1}{2}\sum_{i\neq j}^{N}\frac{e^2}{|\boldsymbol{r_i} - \boldsymbol{r_j}|}. \tag{1.3}$$

The eigenvalues of the electronic Hamiltonian defines the *potential energy surface* (PES).[57] Configurations that are a (global) minimum on the PES contribute predominantly to physical observables. Energy minimization algorithms are therefore commonly used to vary atomic coordinates (and lattice parameters) in order to obtain a minimum on the PES. Various algorithms exists that use, in order of computational demand, i) the energy (simplex method), ii) the energy and the first derivative of the energy (steepest decent and conjugate gradient), iii) the energy, first derivative and approximate second derivative of the energy (Quasi-Newton) and iv) and the energy, first derivative and exact second derivative of the energy (Newton-Raphson).[58] Once a set of atomic coordinates is found that minimizes the energy, various properties can be calculated from derivatives of the energy (see for example, Table 10.0 in reference[57]).

There are scenario's for which the aforementioned static results are not sufficient. For example, temperature-dependent elastic constants are calculated from fluctuations in the strain or stress tensor. This calculation requires that the atoms and lattice undergo dynamic movement by moving along the PES. From the negative gradient of the PES, a trajectory can be generated. These so-called *first-principles* or *ab initio* molecular dynamics simulations are computationally demanding and are for the scope of this thesis not feasible. Instead, the potential energy surface is constructed *a priori* by defining pair-interaction potentials, which reduce the computational cost considerably.

1.1 Density functional theory calculations

Electronic structure theory attempts to find a solution for the many-body electronic Schrödinger equation. The most widely used method to solve the many-body Schrödinger equation is density functional theory (DFT).[59] The two fundamental theorems of DFT were postulated by Hohenberg and Kohn which state that i) for each external potential V_{ext} there exists a uniquely defined ground state density $\rho_e(\boldsymbol{r})$ and ii) the ground state energy can be found variationally.[60] The challenge of DFT is to find an electron density $\rho_e(\boldsymbol{r})$ that minimizes the energy functional $E[\rho_e(\boldsymbol{r})]$. Kohn and Sham introduced a set of solvable equations from which the electron density could be derived in a self-consistent field manner.[61] They proposed a non-interacting reference system with the same electron density $\rho_e(\boldsymbol{r})$

as the real interaction system and by solving the Kohn-Sham equations iteratively

$$\left(\frac{-\hbar^2}{2m_e}\nabla^2 + v_{\text{ext}}(\boldsymbol{r}) + \frac{1}{2}\int \mathrm{d}\boldsymbol{r'}\,\frac{\rho_e(\boldsymbol{r'})}{|\boldsymbol{r}-\boldsymbol{r'}|} + v_{\text{XC}}(\boldsymbol{r})\right)\psi_j = \epsilon_j\psi_j \tag{1.4}$$

the electron density can be calculated according to $\rho_e(\boldsymbol{r}) = \sum \psi_j^*\psi_j$. Here, ψ_j are the one-electron Kohn-Sham orbitals and ϵ_j are the corresponding energy levels. In Equation (1.4), the first term on the left hand side is the kinetic energy of the electrons in the non-interaction framework, the second term is the external potential due to the presence of the nuclei, the third term is the classical Coulomb interaction and the fourth term is the functional derivative of the exchange-correlation (XC) functional. The XC-functional represents the difference between exact kinetic energy and kinetic energy in the non-interaction framework (kinetic correlation energy) and the potential correlation and exchange energy.[57] The challenge of Kohn-Sham DFT is to find suitable expressions for the unknown XC-functional. It is not straightforward to classify XC-functionals based on accuracy or quality but the Perdew's Jacob's ladder is commonly used.[62] Currently, there are over 200 available XC-functionals and their use and development remains an active field of research.[63–68]

Plane wave pseudopotential method

A convenient choice of the basis set for the one-electron Kohn-Sham orbitals in periodic systems are orthogonal plane wave basis functions as stated by *Bloch's theorem*.[55] At each $\boldsymbol{k}$-point, the one-electron Kohn-Sham orbital is written as

$$\psi_j = \sum_{\boldsymbol{G}} c_{j,(\boldsymbol{k}+\boldsymbol{G})} \exp\Big[i(\boldsymbol{k}+\boldsymbol{G})\cdot\boldsymbol{r}\Big] \tag{1.5}$$

with j being the band number, $\boldsymbol{k}$ the wave-vector in reciprocal space, $\boldsymbol{G}$ are the reciprocal lattice vectors and $c_{j,(\boldsymbol{k}+\boldsymbol{G})}$ are the Fourier coefficients.

It is impractical to sum over all reciprocal lattice vectors, which would require an infinite plane wave basis set. By truncating the basis set by a predefined kinetic cut-off, only plane waves with a low kinetic energy (valence electrons) are considered.[69] For the computation of physical properties, integrals in $\boldsymbol{k}$-space are performed over the smallest primitive cell, known as the *Brillouin zone*. A consequence of Bloch's theorem is that only a finite number of $\boldsymbol{k}$-points have to be sampled. The integral of a function $f(\boldsymbol{k})$ can therefore be replaced as a discrete summation over a limited number of $\boldsymbol{k}$-points

$$\int_{\text{BZ}} \mathrm{d}\boldsymbol{k}F(\boldsymbol{k}) = \frac{1}{V}\sum_i \omega_i F(\boldsymbol{k}_i) \tag{1.6}$$

where $F(\boldsymbol{k})$ is the Fourier transform of $f(\boldsymbol{k})$, V the unit cell volume and ω_i are weighting functions. The sampling of $\boldsymbol{k}$-space within the Brillouin zone can be done by using the Monkhorst-Pack scheme.[70]

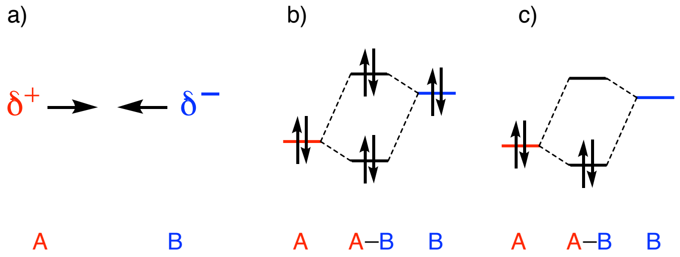

Figure 1.1: *The three components of the energy decomposition analysis that contribute to the interaction energy between fragments A and B: (a) electrostatic interaction* ΔV_{elstat}*, (b) Pauli repulsion* ΔE_{Pauli} *and (c) orbital interaction* ΔE_{oi}*.*

However, Kohn-Sham states fluctuate heavily near the nuclei due to high kinetic energy (core region). Moreover, core-electrons are typically not affected upon a change in chemical bonding. Therefore, it is common to replace the core-valence electronic interactions with a smooth pseudopotential. Different types of pseudopotentials exist such as the norm-conserving,[71] ultrasoft[72] and Trouiller-Martins pseudopotentials.[73] In this thesis, the Projected Augmented Wave (PAW) method as implemented in the Vienna Ab Initio Simulation Package (VASP) code is used.[74–77]

Kohn-Sham molecular orbital method

Kohn-Sham molecular orbital theory and an accompanying energy decomposition analysis scheme can reveal insights into chemical bonding and will be used to elucidate electronic interactions of adsorption of guest molecules at specific adsorption sites in MOFs. In this thesis, the Amsterdam Density Functional (ADF) package[78–80] is used to describe nonperiodic systems. In ADF, linear combinations of Slater-Type Orbitals (STOs) χ_μ are used as basis functions for the one-electron Kohn-Sham orbitals[81]

$$\psi_j = \sum_\mu c_{j\mu}\chi_\mu \tag{1.7}$$

with

$$\chi_\mu = N Y_{l,m}(\theta,\phi) r^{n-1} \exp\left[-\zeta r\right] \tag{1.8}$$

where N is a normalization constant, $Y_{l,m}$ being a spherical harmonic function and ζ a characteristic exponent coefficient that determines the long-range decay.

ADF builds molecular entities from user-defined fragments. From linear combinations of the symmetrized fragment orbitals, the molecular orbitals are constructed. The total bond energy ΔE with respect to the fragments is given by

$$\Delta E = \int \mathrm{d}\boldsymbol{r} \left(\varepsilon[\rho_e, \boldsymbol{r}] - \sum_i \varepsilon_i[\rho_e, \boldsymbol{r}] \right) \tag{1.9}$$

with $\varepsilon[\rho_e, \boldsymbol{r}]$ and $\varepsilon_i[\rho_e, \boldsymbol{r}]$ being the energy density of the overall molecule and fragment i, respectively. The total bond energy ΔE is decomposed using a Morokuma-type[82,83] energy decomposition analysis scheme into the preparation energy ΔE_{prep} and interaction energy ΔE_{int}. The preparation energy is the amount of energy needed to go from the equilibrium structure to the overall molecule. The interaction energy ΔE_{int} between two fragments, A and B is decomposed according to[84–86]

$$\Delta E_{\text{int}} = \Delta V_{\text{elstat}} + \Delta E_{\text{Pauli}} + \Delta E_{\text{oi}} + \Delta E_{\text{disp}}. \tag{1.10}$$

Here, ΔV_{elstat} is the electrostatic interaction of the unperturbed fragments. The Pauli repulsion ΔE_{Pauli} is the destabilizing interaction between occupied orbitals due to the anti-symmetric requirement of the wavefunction. The orbital interaction ΔE_{oi} is due to the relaxation of the final wavefunction by mixing virtual orbitals. The last term in Equation (1.10), ΔE_{disp}, are optional dispersion corrections. The first three contributions are shown schematically in Figure 1.1, showing a simplified molecular orbital diagram for the Pauli repulsion and the orbital interaction. The orbital interaction term is responsible for charge transfer and/or polarization effects and can be further decomposed per irreducible representation Γ of the system's point group given by

$$\Delta E_{\text{oi}} = \sum_{\Gamma} \Delta E_{\text{oi},\Gamma}. \tag{1.11}$$

The orbital interaction is of particular interest in this thesis as will be shown later on: i) it elucidates molecular orbital interactions of relevant donor-acceptor adsorption processes and ii) is used to generate additional force field potentials.

Charge distributions are determined based on the Voronoi deformation density (VDD) method.[87] Here, the spacing is partitioned in non-overlapping regions such that the region of space is closer to a reference nucleus A than to other nuclei.[88] The partial atomic VDD charge is obtained from

$$Q_A^{\text{VDD}} = -\int_{\text{Voronoi cell A}} \mathrm{d}V \left[\rho_e(r) - \sum_B \rho_B(r)\right] \tag{1.12}$$

with $\rho_e(r)$ the total electronic density and $\rho_B(r)$ the ground-state atomic density. This approach measures the change in charge density when going from the atomic charge densities to the total molecular density. A positive and negative value represents a loss and gain of electrons in the Voronoi cell of atom A, respectively.

For a more in depth introduction on electronic structure calculations, the reader is referred to Payne *et al.*,[69] Jensen[57] and Martin.[55]

1.2 Classical force field simulations

1.2.1 Molecular dynamics

Statistical mechanics allows one to relate microscopic properties to macroscopic properties of bulk matter, such as enthalpies, free energies and heat capacities.[89]

For an N-particle system, these microscopic properties are obtained from knowledge of the generalized coordinates $\boldsymbol{q}^N$ and the conjugate momenta $\boldsymbol{p}^N$, collectively known as *phase space coordinates*. A collection of microstates that describe the same macroscopic properties is known as an *ensemble*.[90] For example, the microcanonical ensemble imposes a fixed number of particles N, a fixed volume V and a constant total energy E. However, other ensembles are more convenient in order to mimic experimental conditions *e.g.*, constant temperature and/or pressure. For a one-component system, the adiabatic ensembles can be interrelated through Legendre transformations and isothermal ensembles are obtained from a series of Laplace transformations of the microcanonical ensemble.[91]

Consider an N-particle system with each particle having a generalized coordinate $\boldsymbol{q_i}$ and conjugate momentum $\boldsymbol{p_i}$. The Hamiltonian $\mathcal{H}$ can be given by

$$\mathcal{H} = \sum_i \frac{\boldsymbol{p}_i^2}{2m} + \mathcal{U}(\{\boldsymbol{q_i}\}) \tag{1.13}$$

with m being the mass of the particle and $\mathcal{U}(\{\boldsymbol{q}_i\})$ the potential energy consisting of pre-defined interatomic potentials. The origin and construction of these interatomic potentials, collectively known as a *force field*, are discussed in section 4.2. The Helmholtz free energy is then given by

$$F = -k_{\mathsf{B}} T \ln Q_{\mathsf{NVT}} \tag{1.14}$$

with k_{B} the Boltzmann constant, T the temperature and Q_{NVT} the stationary phase space density, or *partition function*, in the canonical ensemble

$$Q_{\mathsf{NVT}} = \frac{1}{h^{3N} N!} \int\int \mathrm{d}\boldsymbol{q}^N \ \mathrm{d}\boldsymbol{p}^N \exp\left[-\beta \mathcal{H}(\boldsymbol{q}^N, \boldsymbol{p}^N)\right] \tag{1.15}$$

with β being the inverse temperature, h the Planck's constant and the factor $1/N!$ arises from the fact that particles of the same species are indistinguishable. The canonical ensemble average of a phase space function $\langle A(\boldsymbol{q}^N, \boldsymbol{p}^N)\rangle$ is defined as

$$\langle A \rangle = \frac{\int\int \mathrm{d}\boldsymbol{q}^N \ \mathrm{d}\boldsymbol{p}^N A(\boldsymbol{q}^N, \boldsymbol{p}^N) \exp\left[-\beta \mathcal{H}(\boldsymbol{q}^N, \boldsymbol{p}^N)\right]}{Q_{\mathsf{NVT}}} \tag{1.16}$$

and resembles a Boltzmann-weighted average which can be calculated using Metropolis Monte Carlo simulations (see section 1.2.2). Alternatively, assuming the ergodicity hypothesis holds, the average of a phase space function given in Equation (1.16) can also be obtained from a Molecular Dynamics (MD) trajectory[90]

$$\langle A(\boldsymbol{q}^N, \boldsymbol{p}^N)\rangle = \lim_{T\to\infty} \frac{1}{T} \int_0^T \mathrm{d}t A(\boldsymbol{q}^N, \boldsymbol{p}^N). \tag{1.17}$$

MD simulations are based on integrating Newton's equations of motion. The forces f_i that act on each particle are given by the negative gradient of the *a priori* defined potential energy surface $\mathcal{U}$

$$\boldsymbol{f}_i = -\frac{\partial \mathcal{U}}{\partial \boldsymbol{r}_i}. \tag{1.18}$$

Note that $\boldsymbol{r}_i$ are Cartesian coordinates. From knowledge of the forces, the equations of motion can be integrated. Many integrators exists,[92] but a popular choice is the Verlet algorithm[93]

$$\begin{aligned} \boldsymbol{r}_i(t+\Delta t) &= 2\boldsymbol{r}_i(t) - \boldsymbol{r}_i(t-\Delta t) + \frac{\boldsymbol{f}_i(t)}{m}\Delta t^2 \\ \boldsymbol{v}_i(t) &= \frac{\boldsymbol{r}_i(t+\Delta t) - \boldsymbol{r}_i(t-\Delta t)}{2\Delta t} \end{aligned} \tag{1.19}$$

with t being the time, Δt the time-step, $\boldsymbol{r}_i$ the position, $\boldsymbol{v}_i$ the velocity, and $\boldsymbol{f}$ the force acting in particle i.

Simulating crystalline solids also requires a periodic simulation cell $\boldsymbol{h}$, spanned by three vectors $\boldsymbol{a}$, $\boldsymbol{b}$ and $\boldsymbol{c}$. The volume of the simulation cell, V, is given by

$$V = \text{det}\|\boldsymbol{h}\|. \tag{1.20}$$

The position of a particle $\boldsymbol{r}_i$ can be written as fractional coordinates $\boldsymbol{s}_i$

$$\boldsymbol{r}_i = \boldsymbol{h}\boldsymbol{s}_i = \alpha_i\boldsymbol{a} + \beta_i\boldsymbol{b} + \gamma_i\boldsymbol{c} \tag{1.21}$$

with $0 \leq \alpha_i, \beta_i, \gamma_i \leq 1$. In the case of studying constant pressure conditions with MD simulations *e.g.*, to probe structural transitions, the simulation cell $\boldsymbol{h}$ evolves over time. To allow for isotropic unit cell changes, Andersen introduced a Lagrangian that explicitly considers the time-derivative of the simulations cell in the equations of motion, generating the isoenthalpic-isobaric (NPH) ensemble.[94] Anisotropic cell shape changes were proposed by Parrinello and Rahman by extending the Andersen Lagrangian.[95,96]

A homogeneous infinitesimal strain $\boldsymbol{\epsilon}$ can be defined in terms of the simulation cell geometry by[97,98]

$$\boldsymbol{\epsilon} = \frac{1}{2}[(\boldsymbol{h_0}^{-1})^T \cdot \boldsymbol{h}^T \cdot \boldsymbol{h} \cdot \boldsymbol{h}_0^{-1} - \boldsymbol{1}] \tag{1.22}$$

where $\boldsymbol{h}_0$ and $\boldsymbol{h}$ are the reference and deformed simulation cells, respectively. The superscripts T and -1 denote the transpose and inverse, respectively and $\boldsymbol{1}$ is the identity matrix. This atomistic formulation is consistent with expressions of the strain tensor found in classical textbooks on elasticity.[97,99] By expanding the internal energy in terms of the strain tensor, the fourth-rank elastic tensor $\mathcal{C}_{\alpha\beta\nu\mu}$ can be obtained[100]

$$\mathcal{U}(\tilde{\boldsymbol{q}}, \epsilon_{\alpha\beta}) = \mathcal{U}(\tilde{\boldsymbol{q}}, 0) + V_0 \sum_{\alpha\beta} \sigma_{\alpha\beta}\epsilon_{\alpha\beta} + \frac{1}{2} V_0 \sum_{\alpha\beta\mu\nu} \mathcal{C}_{\alpha\beta\mu\nu}\epsilon_{\alpha\beta}\epsilon_{\mu\nu} \cdots \tag{1.23}$$

with $\tilde{\boldsymbol{q}}$ being the reference positions, σ_α the stress tensor and V_0 the undeformed unit cell volume. Note that within the harmonic approximation and for a stress-free structure, Equation (1.23) reduces to Equation (1). A computationally efficient approach for computing finite-temperature elastic constants is the stress-fluctuations method[97,101]

$$\begin{aligned}\mathcal{C}_{\alpha\beta\mu\nu} = \left\langle \mathcal{C}^B_{\alpha\beta\mu\nu} \right\rangle - \frac{V}{k_B T}\left[\left\langle \sigma^B_{\alpha\beta}\sigma^B_{\mu\nu} \right\rangle - \left\langle \sigma^B_{\alpha\beta} \right\rangle \left\langle \sigma^B_{\mu\nu} \right\rangle \right] \\ + \rho k_B T(\delta_{\alpha\mu}\delta_{\beta\nu} + \delta_{\alpha\nu}\delta_{\beta\mu}).\end{aligned} \tag{1.24}$$

where the first term is the *Born*-term, defined as

$$\left\langle \mathcal{C}^B_{\alpha\beta\mu\nu} \right\rangle = \frac{1}{V}\left(\frac{\partial^2 \mathcal{U}}{\partial \epsilon_{\alpha\beta}\partial \epsilon_{\mu\nu}} \right) \tag{1.25}$$

and the second and third terms of Equation (1.24) are the fluctuations of the stress tensor and an ideal gas contribution. For pair wise additive interactions, the stress tensor σ is calculated from the virial expression

$$\sigma_{\alpha\beta} = \frac{1}{V}\sum_i \left[\frac{1}{2}\sum_{j=1}^{N} (r^\alpha_j - r^\alpha_j) f^\beta_{ij} - n_d k_B T_i \right] \tag{1.26}$$

with f^α_{ij} the internal force on atom i due to atom j in the current configuration along direction α and n_d being the number of degrees of freedom. At 0 Kelvin, Equation (1.24) reduces to[102]

$$\begin{aligned}\mathcal{C}_{\alpha\beta\mu\nu} &= -\frac{1}{V}\frac{\partial \sigma_{\alpha\beta}}{\partial \epsilon_{\mu\nu}}\bigg|_{f_s=0} = \frac{1}{V}\frac{\partial^2 \mathcal{U}}{\partial \epsilon_{\alpha\beta}\partial \epsilon_{\mu\nu}}\bigg|_{f_s=0} \\ &= \frac{1}{V}\left[\underbrace{\frac{\partial^2 \mathcal{U}}{\partial \epsilon_{\alpha\beta}\partial \epsilon_{\mu\nu}}}_{\text{Born term}} - \underbrace{\frac{\partial^2 \mathcal{U}}{\partial \epsilon_{\alpha\beta}\partial r_{i\lambda}} \left(\mathcal{H}^{-1}_{ij} \right)_{i\lambda, j\xi} \frac{\partial^2 \mathcal{U}}{\partial \epsilon_{\mu\nu}\partial r_{i\xi}}}_{\text{Relaxation term}} \right] \\ &= \frac{1}{V}\left[\mathcal{H}_{\epsilon\epsilon} - \mathcal{H}_{\epsilon i}\left(\mathcal{H}_{ij} \right)^{-1} \mathcal{H}_{i\epsilon} \right].\end{aligned} \tag{1.27}$$

Note that before and after a strain is applied, the system must be in a state of zero force ($f_s = 0$). The Born term is the energy response due to a strained unit cell whereas the relaxation term accounts for the atomic relaxation since there is more than one atom in the unit cell. $\mathcal{H}_{ij}$ is the Hessian (force constants) matrix, $\mathcal{H}_{\epsilon\epsilon}$ is the second derivative and the internal energy with respect to the strains and $\mathcal{H}_{\epsilon i}$ and $\mathcal{H}_{i\epsilon}$ are cross-terms. A generalized Hessian can be constructed that contains the aforementioned terms.[103] Using robust optimization algorithms, such as the mode-following technique[104] (also known as the Baker's minimization[105]), a true local minimum on the energy surface can be obtained and hence the elastic constants are obtained for 'free'.

1.2.2 Monte Carlo

The Metropolis Monte Carlo (MC) technique allows one to determine the ensemble average of Equation (1.16) by generating new configurational states, which are accepted or rejected based on a specific acceptance criteria.[106] The momentum part of the phase space integral given in Equation (1.15) integrates out and reduces to:

$$\begin{aligned} Q_{\mathsf{NVT}} &= \frac{1}{h^{3N}N!}\int\int \mathrm{d}\boldsymbol{q}^N\ \mathrm{d}\boldsymbol{p}^N \exp\left[-\beta\mathcal{H}(\boldsymbol{q}^N,\boldsymbol{p}^N)\right] \\ &= \frac{1}{\Lambda^{3N}N!}\int \mathrm{d}\boldsymbol{q}^N \exp\left[-\beta\mathcal{U}(\boldsymbol{q}^N)\right] \end{aligned} \tag{1.28}$$

where the relation $\int_{-\infty}^{\infty} \mathrm{d}x \exp\left[-x^2\right] = \sqrt{\pi}$ is used and Λ is the thermal de Broglie wavelength defined as $\Lambda = \sqrt{h^2/(2\pi m k_B T)}$. A coordinate transformation can be adapted that introduces the fractional coordinates $\boldsymbol{s}_i$ using Equation (1.21). The partition function becomes

$$Q_{\mathsf{NVT}} = \frac{V^N}{\Lambda^{3N}N!}\int \mathrm{d}\boldsymbol{s}^N \exp\left[-\beta\mathcal{U}(\boldsymbol{s}^N;\boldsymbol{h})\right] \tag{1.29}$$

where the potential energy now depends on the fractional coordinates and parameterically on the transformation matrix.

Once an equilibrium distribution has been reached, the transition probability to go from an old configuration o to a new configuration n must not destroy the established equilibrium distribution.[106] A stricter version of this condition is the concept of *detailed balance*, which states

$$\mathcal{P}(\mathsf{o})\alpha(\mathsf{o}{\rightarrow}\mathsf{n})\mathsf{acc}(\mathsf{o}{\rightarrow}\mathsf{n}) = \mathcal{P}(\mathsf{n})\alpha(\mathsf{n}{\rightarrow}\mathsf{o})\mathsf{acc}(\mathsf{n}{\rightarrow}\mathsf{o}). \tag{1.30}$$

Here, $\mathcal{P}$ is the probability density of a new (n) or old (o) state and $\alpha(\mathsf{o}{\rightarrow}\mathsf{n})$ is the probability of generating state n from state o. In the Metropolis scheme, α is a symmetric matrix ($\alpha(\mathsf{o}{\rightarrow}\mathsf{n}) = \alpha(\mathsf{n}{\rightarrow}\mathsf{o})$) and the probability of accepting a trial move from o to n is given by $\mathsf{acc}(\mathsf{o}{\rightarrow}\mathsf{n})$. In the canonical ensemble, the probability density is given by

$$\mathcal{P} = \frac{\exp\left[-\beta\mathcal{U}(\boldsymbol{s}^N;\boldsymbol{h})\right]}{Q_{\mathsf{NVT}}} \tag{1.31}$$

and the acceptance probability that follows from the detailed balance requirement is

$$\begin{aligned} \mathcal{P}_{\mathsf{acc}}(\mathsf{o}\rightarrow\mathsf{n}) &= \mathsf{min}\Big(1, \frac{\mathcal{P}_{\mathsf{n}}}{\mathcal{P}_{\mathsf{o}}}\Big) \\ &= \mathsf{min}\Big(1, \exp\big[-\beta(\mathcal{U}_{\mathsf{n}}(\boldsymbol{s}^N;\boldsymbol{h}) - \mathcal{U}_{\mathsf{o}}(\boldsymbol{s}^N;\boldsymbol{h}))\big]\Big). \end{aligned} \tag{1.32}$$

The acceptance criterion implies that if the energy of the newly generate state is lower than that of the old state, the trial move will be accepted. Otherwise, if a

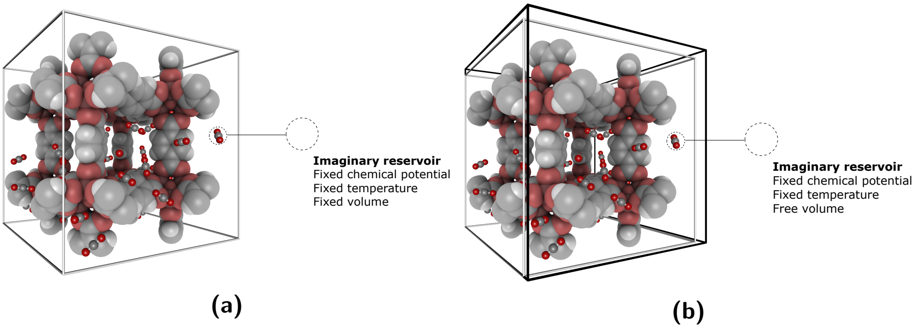

Figure 1.2: *Adsorption properties can be calculated using the (a) grand-canonical (μVT) and (b) osmotic ($\mu_1 N_2 pT$) ensembles. The bulk fluid phase is replaced by an imaginary reservoir. In the (μVT)-ensemble, the volume is fixed whereas in the ($\mu_1 N_2 pT$)-ensemble, the volume is allowed to fluctuate.*

randomly generated number on the interval [0,1) is less than acc(o→n), the move is accepted.

In this thesis, adsorption isotherms are computed using Monte Carlo simulations in the i) grand-canonical (μVT) and ii) the osmotic ($\mu_1 N_2 pT$) ensembles for rigid and flexible frameworks, respectively. This is depicted schematically in Figure 1.2.

Grand-canonical ensemble

In the grand-canonical ensemble, the chemical potential μ, unit cell volume V and temperature T are fixed, whereas the number of particles N is allowed to fluctuate.[107] To obtain chemical equilibrium between the adsorbed phase and the fluid phase, the temperature and the chemical potential of fluid inside and outside the framework material should be the same.

The partition function of the grand-canonical ensemble can be derived from an ideal gas that can exchange particles with a N-particle system. It can be shown that[108]

$$Q_{\mu\mathsf{VT}} = \sum_{N=0}^{\infty} \frac{\exp\left[\beta\mu N\right] V^N}{\Lambda^{3N} N!} \int \mathrm{d}\boldsymbol{s}^N \exp\left[-\beta\mathcal{U}(\boldsymbol{s}^N;\boldsymbol{h})\right]. \tag{1.33}$$

To sample the grand canonical ensemble, three MC trial moves can be used. These trial moves and the associated acceptance criteria are: particle displacement

$$\mathcal{P}_{\mathsf{acc}}(\mathsf{o}\rightarrow\mathsf{n}) = \mathsf{min}\Big(1, \exp\big[-\beta(\mathcal{U}_{\mathsf{n}}(\boldsymbol{s}^N;\boldsymbol{h}) - \mathcal{U}_{\mathsf{o}}(\boldsymbol{s}^N;\boldsymbol{h}))\big]\Big) \tag{1.34}$$

particle insertion

$$\mathcal{P}_{\mathsf{acc}}(\mathsf{o}\rightarrow\mathsf{n}) = \mathsf{min}\Big(1, \frac{V\exp\left[\beta\mu\right]}{\Lambda^3(N+1)} \exp\big[-\beta(\mathcal{U}_{\mathsf{n}}(\boldsymbol{s}^{N+1};\boldsymbol{h}) - \mathcal{U}_{\mathsf{o}}(\boldsymbol{s}^N;\boldsymbol{h}))\big]\Big) \tag{1.35}$$

and particle deletion

$$\mathcal{P}_{\mathsf{acc}}(\mathsf{o} \to \mathsf{n}) = \min\Big(1, \frac{\Lambda^3 N}{V \exp\left[\beta\mu\right]} \exp\left[-\beta(\mathcal{U}_{\mathsf{n}}(\boldsymbol{s}^{N-1};\boldsymbol{h}) - \mathcal{U}_{\mathsf{o}}(\boldsymbol{s}^{N};\boldsymbol{h}))\right]\Big). \tag{1.36}$$

The chemical potential is imposed by choosing a pressure that is converted into the fugacity f using an equation of state (*e.g.*, Peng-Robinson[109]). The fugacity is then related to the chemical potential via

$$\beta\mu = \beta\mu_{ID} + \ln(\beta f) \tag{1.37}$$

where μ_{ID} is the reference chemical potential.

Osmotic ensemble

The osmotic ($\mu_1 N_2 p T$) ensemble is used to study adsorption in flexible framework materials. This ensemble is only defined for a multicomponent system, as for a single component system it is not possible to vary the chemical potential, pressure and temperature independently, due to the Gibbs-Duhem relation. Fluctuations are allowed for the number of particles of species 1 (adsorbates) and the chemical potential of species 2 (framework material). The osmotic potential can be derived from the *Ray*-potential applied to a multicomponent system. The Ray-potential R was introduced in 1990 as the thermodynamic potential describing a porous, adiabatic piston between the system and the combined pressure and chemical potential reservoir.[110,111] Applying the Ray-potential as a Legendre transformation on a two-component system, the following relation is obtained

$$\mathrm{d}R = T\,\mathrm{d}S + V\,\mathrm{d}p - N_1\,\mathrm{d}\mu_1 + \mu_2\,\mathrm{d}N_2. \tag{1.38}$$

The osmotic potential Ω_{os} is a Legendre transformation of the Ray-potential with respect to the entropy

$$\begin{aligned}
\mathrm{d}\Omega_{\mathsf{os}} &= \mathrm{d}R - T\,\mathrm{d}S - S\,\mathrm{d}T \\
\mathrm{d}\Omega_{\mathsf{os}} &= \Big\{T\,\mathrm{d}S + V\,\mathrm{d}p - N_1\,\mathrm{d}\mu_1 + \mu_2\,\mathrm{d}N_2\Big\} - T\,\mathrm{d}S - S\,\mathrm{d}T \\
\mathrm{d}\Omega_{\mathsf{os}} &= -S\,\mathrm{d}T + V\,\mathrm{d}p - N_1\,\mathrm{d}\mu_1 + \mu_2\,\mathrm{d}N_2
\end{aligned} \tag{1.39}$$

with natural variables T, p, μ_1 and N_2. Although, the ($\mu_1 N_2 p T$)-ensemble was first mentioned by Stockmayer in 1950 for light scattering in multicomponent systems,[112] it was not used until 1993 by Wolf *et al.* to study pressure-composition isotherms in palladium hydride.[113] Coudert *et al.* provided a thermodynamic framework for adsorption in a flexible material showing that the osmotic potential can be calculated from the free energy of the framework phase, the adsorption isotherm of guest molecules in that phase and the pressure-dependent molar volume of the fluid.[114]

The probability density $\mathcal{P}$ for a flexible host-adsorbate system is written as[113]

$$\mathcal{P}(\boldsymbol{s}^N, V, N_{\mathsf{ads}})_{\mu_{\mathsf{ads}} N_{\mathsf{host}} pT} \propto \frac{V^N \exp\left[\beta \mu_{\mathsf{ads}} N_{\mathsf{ads}}\right]}{\Lambda^{3N_{\mathsf{ads}}} \Lambda^{3N_{\mathsf{host}}} N_{\mathsf{host}}! N_{\mathsf{ads}}!} \times \exp\big[-\beta(\mathcal{U}(\boldsymbol{s}^N; \boldsymbol{h}) + pV)\big]. \tag{1.40}$$

The acceptance probability for any of the four MC-moves (insertion, deletion, translation and volume change) is given by $\mathcal{P}_{\mathsf{accept}} = \mathsf{min}(1, \mathcal{P}'/\mathcal{P})$ with $\mathcal{P}'$ defined in Equation (1.40) as the probability of the trial state and $\mathcal{P}$ the probability of the current state. The acceptance rules for particle displacement, insertion and deletion are equivalent to those in the grand-canonical ensemble. The volume change acceptance rule is written explicitly as

$$\mathcal{P}_{\mathsf{acc}}(\mathsf{o} \to \mathsf{n}) = \mathsf{min}\Bigg(1, \left(\frac{V_{\mathsf{n}}}{V_{\mathsf{o}}}\right)^N \exp\big[-\beta p(V_{\mathsf{n}} - V_{\mathsf{o}})\big] \times \exp\big[-\beta(\mathcal{U}_{\mathsf{n}}(\boldsymbol{s}^N; \boldsymbol{h}) - \mathcal{U}_{\mathsf{o}}(\boldsymbol{s}^N; \boldsymbol{h}))\big]\Bigg). \tag{1.41}$$

Monte Carlo simulations in the osmotic ensemble can easily be an order of magnitude more expensive than in grand-canonical ensemble due to additional sampling over volume changes.[115]

All classical force field simulations in this thesis are conducted using RASPA-2.0.[116] All atomistic visualizations are generated using iRASPA.[117]

The reader is referred to textbooks by Frenkel and Smit,[108] Tuckerman,[90] Allen and Tildesley[118] and Leach[119] for a detailed introduction into classical simulation methodology.

CHAPTER 2

Kohn-Sham molecular orbital analysis of hydrated HKUST-1

A Kohn-Sham molecular orbital (MO) analysis with accompanying energy decomposition analysis is presented of the water-HKUST-1 interactions. Hybrid and metahybrid functionals show better agreement with experimental and CCSD(T) observations as compared to GGA-functionals. Upon monohydration, a Jahn-Teller distortion is observed due to Pauli repulsion between the HOMO(A1) of water and the dicopper d_{z2}-orbitals. Donor-acceptor interactions confirm the formation of a σ-bond between the two Cu(II) sites as was suggested recently using electron paramagnetic resonance. The filling of empty Cu($4s$) and Cu($4p_z$) orbitals on the opposite copper lowers the adsorption energy of the second water molecule.

Based on: J. Heinen, D. Dubbeldam and C. Fonseca Guerra, Kohn-Sham Molecular Orbital Analysis of the Coordination Bond in Anhydrous and Hydrated HKUST-1, *In preparation*, **2018**

2.1 Introduction

MOFs have been proposed as sorbent materials for carbon capture.[120] Specifically, MOFs containing open-metal sites (OMS) have drawn considerable interest due to their enhanced reactivity.[121] One such MOF is HKUST-1 [also known as $Cu_3(BTC)_2$; BTC = benzene-1,3,5-tricarboxlic acid] that contains a dicopper paddlewheel, as shown in Figure 2.1.[122]

As nearly 10% of flue gas consists of water, it is crucial for separation studies to include the effects of water.[123] It is known however that water decomposes the crystalline structure of HKUST-1.[124–127] After 24 hr exposure of water at 323 K, the surface area decreased from 1340 to 647 m^2/g.[124] Water adsorption cycling studies performed by Henninger *et al.* showed a capacity loss of 53% after 20 adsorption cycles between 40 and 140 °C.[128] A ReaxFF simulation study indicated that one water molecule per OMS is sufficient, at 550 K, to collapse the structure.[129] Andersen *et al.* argued that the coordination bond is not broken immediately, but it requires long times (kinetics is a key role) and a considerable amount of water molecules in the structure.[130] This is in agreement with Buscarino *et al.* whom proposed a three step decomposition process that involves the reversible formation of a σ-bond between the two Cu(II) sites prior to the irreversible hydrolysis of the $Cu\text{-}O_{\text{carboxylate}}$ coordination bond.[127] The irreversible hydrolysis is accompanied by a reduction of the oxidation state from Cu^{2+} to Cu^{1+}.[131]

At higher water loadings, the CO_2 saturation capacity decreases considerably.[132,133] However, weakly hydrated HKUST-1 (4 wt %) increases the CO_2

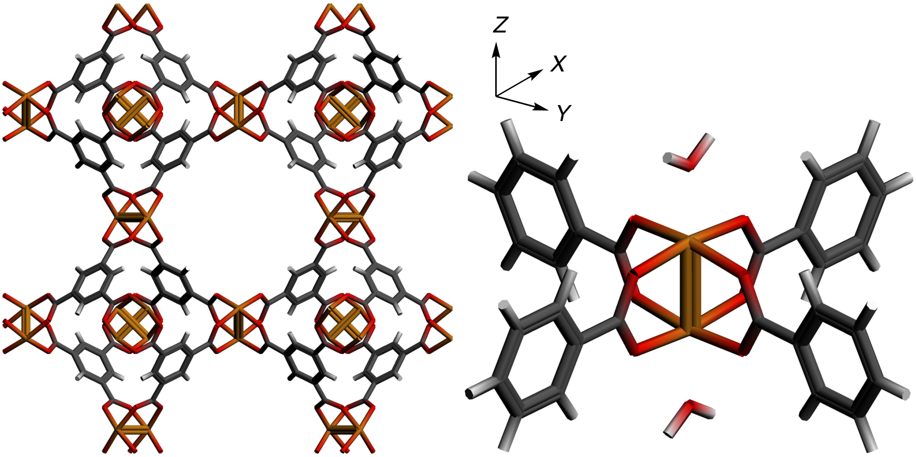

(a) (b)

Figure 2.1: *Stick representation of (a) crystallographic unit cell of HKUST-1 and (b) dihydrated open-metal site ($Cu_2(O_2C_7H_5)_4$) cluster. Color legend: C (gray), O (red), H (white), Cu (orange).*

uptake and its selectivity over methane and N_2.[133,134] This behavior has also been reported in Zn, Co and Ni-based HKUST-1 structures.[135]

Considerable theoretical work has been dedicated to understand the interaction between the OMS of HKUST-1 and water.[136–142] However, associated mechanisms remain unexplored. In this work, we provide a Kohn-Sham molecular orbital analysis with an accompanying energy decomposition analysis (EDA) scheme of water-OMS interactions in HKUST-1.

2.2 Broken-symmetry

The exact nature of the Cu(II)-Cu(II) bond in dicopper species has led to much controversy about half a century ago.[136,143–146] The dicopper paddlewheel of the OMS exhibit antiferromagnetic spin couping and has a coupling constant J in the range of -150 cm^{-1} to -200 cm^{-1}.[147,148] The ground-state wavefunction, describing an open-shell singlet state, has a multireference character. Representing open-shell polynuclear systems using single Slater determinant methods, such as density functional theory (DFT), is therefore challenging.[137,149–155] Broken-symmetry calculations provide outcome and are discussed below.

Any many-body fermionic wavefunction must be anti-symmetric as a result of the Pauli principle.[53] Consider a closed shell wavefunction of two-electrons with opposite spin. A valid wavefunction for a two-electron system is a Slater determinant which is an anti-symmetrized spin-orbital product given by

$$\begin{aligned} \psi_{\text{closed shell}} &= \frac{1}{\sqrt{2}} \begin{vmatrix} \phi(1)\alpha(1) & \phi(2)\alpha(2) \\ \phi(1)\beta(1) & \phi(2)\beta(2) \end{vmatrix} \\ &= \frac{1}{\sqrt{2}} \Big(\underbrace{\phi(1)\phi(2)}_{\text{symmetric}} \underbrace{[\alpha(1)\beta(2) - \alpha(2)\beta(1)]}_{\text{anti-symmetric}} \Big) \end{aligned} \tag{2.1}$$

where the spatial part of the wavefunction ϕ are orthogonal and symmetric and the spin-part is anti-symmetric with $\langle S^2 \rangle = 0$. In the case of an open-shell system, the wavefunctions can take multiple forms. Consider two magnetic centers a and b with spatial orbitals ϕ_a and ϕ_b containing each one electron. The magnetic coupling of two spins is given by Heisenberg-Vleck-Dirac Hamiltonian[156]

$$\hat{\mathscr{H}}_{\text{HVD}} = -2J\hat{S}_a \cdot \hat{S}_b \tag{2.2}$$

with J being the (magnetic) coupling constant describing the difference between the open-shell singlet and triplet state. The convention is $J < 0$ for antiferromagnetic spin-coupling and $J > 0$ for ferromagnetic spin-coupling. The possible wavefunctions for a two-electron system are shown schematically in Figure 2.2 with ψ_0 and ψ_1 denoting the open-shell singlet and triplet configurations. The open-shell singlet wavefunction ψ_0 can be written as

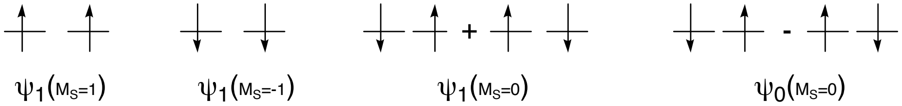

Figure 2.2: *Four possible spin-configurations for an open-shell two-electron system.* ψ_1 *and* ψ_0 *denote the triplet and singlet wavefunctions, respectively.*

$$\psi_0 = \frac{1}{\sqrt{2}}\Big(\underbrace{\phi_a(1)\phi_b(2) + \phi_b(1)\phi_a(2)}_{\text{symmetric}}\Big)\frac{1}{\sqrt{2}}\Big(\underbrace{\alpha(1)\beta(2) - \beta(1)\alpha(2)}_{\text{anti-symmetric}}\Big) \tag{2.3}$$

and the triplet wavefunctions ψ_1 are given by

$$\psi_1 = \frac{1}{\sqrt{2}}\Big(\underbrace{\phi_a(1)\phi_b(2) - \phi_b(1)\phi_a(2)}_{\text{anti-symmetric}}\Big)\underbrace{\begin{cases}\alpha(1)\alpha(2) & M_s = 1\\ \frac{1}{\sqrt{2}}(\alpha(1)\beta(2) + \beta(1)\alpha(2)) & M_s = 0\\ \beta(1)\beta(2) & M_s = 1\end{cases}}_{\text{symmetric}} \tag{2.4}$$

The spin quantum number is defined by $M_s = (N_\alpha - N_\beta)/2$ with N_x being the amount of α or β electrons. Inspection of the wavefunctions shows that two Slater determinants are needed to describe ψ_0 and $\psi_{1,0}$. By definition, Kohn-Sham DFT is a single Slater determinant method and therefore cannot, formally, describe ψ_0 and $\psi_{1,0}$.

A *broken-symmetry* wavefunction ψ_{BS} is introduced that consists of two orthogonal spatial orbitals with opposite spin[157]

$$\begin{aligned}\psi_{\text{BS}} &= \frac{1}{\sqrt{2}}\begin{vmatrix}\phi_a(1)\alpha(1) & \phi_b(1)\beta(1)\\ \phi_a(2)\alpha(2) & \phi_b(2)\beta(2)\end{vmatrix}\\ &= \frac{1}{\sqrt{2}}\Big(\psi_{1,0} + \psi_{0,0}\Big).\end{aligned} \tag{2.5}$$

Note that ψ_{BS} is not an eigenstate of spin but a wavefunction of mixed-spin states such that $\langle S^2\rangle_{\text{BS}} = 1$. The broken-symmetry wavefunction is constructed by localizing spins of the different atomic centers.[158] Calculating the expectation value of the Hamiltonian of the broken-symmetry wavefunction gives

$$\begin{aligned}E_{\text{BS}} &= \langle\psi_{\text{BS}}|\mathscr{H}_e|\psi_{\text{BS}}\rangle\\ &= \frac{1}{2}\Big(\langle\psi_{0,0}|\mathscr{H}_e|\psi_{0,0}\rangle + \langle\psi_{1,0}|\mathscr{H}_e|\psi_{1,0}\rangle\Big)\\ &= \frac{1}{2}\Big(E_{\text{S=0}} + E_{\text{S=1}}\Big)\end{aligned} \tag{2.6}$$

where $E_{\text{S=1}}$ is equivalent to the energy of a single configuration triplet wavefunction (*e.g.*, $\langle\psi_{1,1}|\mathcal{H}|\psi_{1,1}\rangle$). From Equation (2.6), the open-shell singlet energy can be calculated, but it is more common to report the coupling constant

$$J_1 = 2(E_{\mathrm{BS}} - E_{\mathrm{S=1}}). \tag{2.7}$$

Equation (2.7) was first proposed by Noodleman under the assumption that the spatial orbitals are weakly interacting (localized limit).[158] Note that in the original Noodleman paper, the coupling constant is expressed as $J = (E_{\mathrm{BS}} - E_{\mathrm{Smax}})/S^2_{\mathrm{max}}$.[158] This depends on the choice of the Heisenberg Hamiltonian. This approach has been widely used for the prediction of the coupling constant in polynuclear species.[153,159] Others have used the broken-symmetry energy as the energy of the true open-shell singlet state which is the strong delocalization limit.[149,160,161] There is still debate in literature on this topic.[162–164]

Yamaguchi *et al.* proposed an expression for the coupling constant by taken spin contamination into account[165]

$$J_2 = 2\frac{E_{\mathrm{BS}} - E_{\mathrm{T}}}{\langle S^2 \rangle_{\mathrm{T}} - \langle S^2 \rangle_{\mathrm{BS}}} \tag{2.8}$$

with $\langle S^2 \rangle$ the expectation value of the spin square operator of either spin state.

The choice of the exchange-correlation functional heavily affects the coupling constant. Part of the origin of this problem is the presence of the self-interaction error (SIE). The SIE appears due to the incomplete cancellation of the classical electrostatic repulsion of the one-electron system.[151] In the Hartree-Fock formalism, this spurious behavior is exactly canceled due to the exact exchange term.

2.3 Computational methodology

DFT calculations were performed using the ADF package.[78–80] Atomic orbitals were expanded in Slater-Type Orbitals using a TZ2P basis set. Representative HKUST-1-clusters were optimized in the triplet spin-configuration using the B3LYP-D3 functional.[166,167] The use of a cluster-model is justified since HKUST-1 shows negligible band dispersion.[155,168] The open-shell singlet energy $\Delta E^S_{\mathrm{int}}$ is calculated from the broken-symmetry state using the weak interaction regime (strong localized limit) by Noodleman *et al.*[158,169]

The broken-symmetry wavefunction has an exact value of 1.0 for the expectation value of the spin square operator $\langle S^2 \rangle_{\mathrm{bs}}$ as they can be considered as equal mixtures of the singlet ($\langle S^2 \rangle$=0) and triplet ($\langle S^2 \rangle$=2) states.[170]

The overlap integral between the two singly occupied molecular orbitals (SOMOs), S_{ab}, is approximated as proposed by Ruiz *et al.*[149]

$$S^2_{\mathrm{ab}} \approx \rho^2_{\mathrm{T}} - \rho^2_{\mathrm{bs}} \tag{2.9}$$

with ρ_{T} and ρ_{bs} being the Mulliken spin density of the metallic site of the triplet and broken-symmetry state, respectively. The interaction energies are determined by the energy decomposition analysis scheme as described in section 1.1.

2.4 Results and discussion

Considerable work has already been done on the effect of XC-functionals on coupling constants and interaction energies.[137,141,149,152,154,162,171,172] For completeness of this study, we have also calculated these values as well as the components of the energy decomposition analysis scheme.

Table 2.1 reports magnetic properties and the components of the EDA of $Cu_2(HCOO)_4{\cdot}2(H_2O)$. This cluster model was chosen since CCSD(T) interaction energies and coupling constants are available for this geometry.[154] As expected, functionals based on the generalized gradient approximation (GGA) underestimate the open-shell singlet adsorption energies ΔE^S_{int} and overestimate the coupling constants J compared to the CCSD(T) values. Upon increasing exact exchange, the coupling constant converges towards the experimental range of -150 to -200 cm^{-1}.[149] This converging trend is also observed for the expectation value of the S^2 operator, $\langle S^2 \rangle$. Larger spin delocalization is observed for GGA-functionals compared to hybrid functionals. This is evident from reduced spin densities on the magnetic sites and the larger overlap integrals between the SOMOs. The B3LYP-D3 and M06-L open-shell singlet interaction energies, -11.18 and -12.98 $\text{kcal}{\cdot}\text{mol}^{-1}$, are in reasonable agreement with the CCSD(T) value of -12.24 $\text{kcal}{\cdot}\text{mol}^{-1}$. However, their coupling constants deviate from the CCSD(T) value of -176 cm^{-1}. It must be noted that ~ 350 cm^{-1} corresponds to the 1 $\text{kcal}{\cdot}\text{mol}^{-1}$ 'chemical accuracy'.[173] The components of the EDA do not differ much which is promising for a chemical understanding of the interactions.

For dicopper species, the unpaired electrons occupy each a Cu($d_{\text{x2-y2}}$)-orbital, forming symmetric S and anti-symmetric A combinations. The relative energies of the S and A combinations affect the nature of the Cu-Cu bond.[136] GGA, meta-GGA and the hybrid functional TPSSH (10% exact exchange) functional, reported in Table 2.2, indicate that the energy ordering is $A_{\text{x2-y2}} > S_{\text{x2-y2}}$ for α-MOs (ordering for β-spin MOs is equivalent). For example, $S_{\text{x2-y2}}$ and $A_{\text{x2-y2}}$ for BLYP-D3 give -9.3 eV and -5.6 eV, respectively. A recent study using plane-wave pseudopotentials (PBE-PAW) also showed this ordering.[174] However, at increasing amounts of exact exchange, the S and A energy ordering reverses, with M06-2X forming an exception. Here, B3LYP-D3 give for $S_{\text{x2-y2}}$ and $A_{\text{x2-y2}}$, -11.8 eV and -14.6 eV, respectively. Hoffmann *et al.* also found that the $A_{\text{x2-y2}}$-orbitals are lower in energy than the $S_{\text{x2-y2}}$-obitals and suggested that in the singlet ground state this gives rise to an antibonding δ-bond.[136]

In the remainder of the text are all values calculated at the B3LYP-D3/TZ2P level. A larger cluster model, $Cu_2(O_2C_7H_5)_4$, with a benzoate as linker shown in Figure 2.1b, will be used to assess the electronic interactions.

Table 2.1: *Coupling constants J (cm^{-1}), Voronoi deformation density charge on Cu q_{VDD}, expectation value of the spin square operator $\langle S^2 \rangle$, Mulliken spin density ρ, approximated overlap integral of the SOMO's S_{ab} and components of the energy decomposition analysis scheme (kcal·mol^{-1}) of $Cu_2(HCOO)_4 \cdot 2(H_2O)$ with D_{2h} symmetry. EDA results is the average of two water molecules and ΔE^S_{int} is calculated using the projection scheme of Noodleman. Percentage of exact exchange is denoted as subscript. * Broken-symmetry SCF did not converge properly.*

	q_{VDD}	$\langle S^2 \rangle_{\text{T}}$	$\langle S^2 \rangle_{\text{BS}}$	ρ_{T}	ρ_{BS}	S_{ab}	J_1	J_2	ΔV_{elstat}	ΔE_{Pauli}	ΔE_{oi}	ΔE_{disp}	ΔE^T_{int}	ΔE^S_{int}
BLYP-D3$_0$	0.45	2.00	0.76	0.54	-0.48	0.24	-2238	-1119	-19.99	22.41	-8.02	-2.99	-8.59	-10.19
S12g-D3$_0$	0.47	2.00	0.76	0.53	-0.48	0.24	-2329	-1165	-19.06	19.88	-7.89	-2.02	-9.09	-10.76
OPBE$_0$	0.47	2.00	0.75	0.51	-0.45	0.23	-2315	-1158	-17.72	23.49	-7.15	-	-1.39	-3.05
M06-L$_0$	0.53	2.00	0.91	0.61	-0.59	0.14	-1413	-707	-17.94	14.68	-8.72	-	-11.97	-12.98
*TPSSH$_{10}$	-	2.00	0.00	0.61	0.00	0.61	11689	5844	-18.76	19.05	-8.08	-	-7.78	0.57
B3LYP-D3$_{20}$	0.55	2.00	0.98	0.64	-0.63	0.11	-776	-388	-19.29	19.56	-8.39	-2.5	-10.62	-11.18
PBE0$_{25}$	0.57	2.00	0.99	0.66	-0.66	0.10	-623	-311	-18.58	17.48	-8.58	-	-9.68	-10.13
mPW1PW$_{42.8}$	0.58	2.00	0.99	0.66	-0.66	0.10	-609	-304	-18.43	18.24	-8.53	-	-8.72	-9.16
M06-2X$_{54)}$	0.68	2.01	1.00	0.79	-0.78	0.06	-210	-104	-18.68	13.81	-9.81	-	-14.68	-14.83

Table 2.2: *Copper $d_{x2\text{-}y2}$ contributions in α-MOs of anhydrous $Cu_2(O_2C_7H_5)_4$. Symmetric and anti-symmetric combinations of the $d_{x2\text{-}y2}$-orbitals are denoted by $S_{x2\text{-}y2}$ and $A_{x2\text{-}y2}$. Percentage of exact exchange is given in parenthesis. E denotes energy level of the MO. MOs in bold have largest $d_{x2\text{-}y2}$ contribution.*

		$S_{x2\text{-}y2}$			$A_{x2\text{-}y2}$	
	#MO	Cont. (%)	E (eV)	#MO	Cont. (%)	E (eV)
BLYP-D3	17	33.0	-5.1	**12**	**33.7**	**-5.6**
(0)	16	9.0	-8.6	11	25.6	-8.0
	15	**40.7**	**-9.3**	10	10.9	-8.4
				7	21.66	-12.3
S12g-D3	17	32.1	-5.3	**12**	**32.3**	**-5.7**
(0)	16	8.6	-8.7	11	22.7	-8.2
	15	**42.5**	**-9.5**	10	15.6	-8.5
				7	20.7	-12.5
OPBE	17	32.8	-5.2	**12**	**33.2**	**-5.7**
(0)	16	9.2	-8.6	11	23.3	-8.1
	15	**41.8**	**-9.4**	10	14.6	-8.5
				7	20.3	-12.5
M06L	17	27.8	-5.6	12	27.1	-6.0
(0)	16	5.7	-8.9	11	13.2	-8.4
	15	**48.3**	**-9.9**	**10**	**27.5**	**-8.8**
				7	22.5	-12.8
TPSSH	17	23.6	-6.2	12	22.1	-6.7
(10)	16	3.6	-9.5	11	6.1	-9.0
	15	**49.5**	**-10.7**	**10**	**33.5**	**-9.5**
				7	29.1	-13.5
B3LYP-D3	17	17.5	-7.1	12	15.5	-7.6
(20)	16	1.8	-10.1	11	1.5	-9.7
	15	**39.7**	**-11.8**	10	35.8	-10.6
	14	14.8	-12.5	**7**	**37.7**	**-14.6**
	11	9.2	-15.7			
PBE0	17	14.6	-7.4	12	12.4	-7.9
(25)	16	1.45	-10.3	11	0	-9.8
	15	25.9	-12.3	10	33.9	-11.0
	14	**27.0**	**-12.9**	**7**	**42.5**	**-15.1**
	11	11.0	-16.1			
mPW1PW	17	14.5	-7.5	12	12.31	-7.9
(42.8)	16	1.4	-10.4	11	0	-9.9
	15	26.1	-12.3	10	33.7	-11.1
	14	**26.2**	**-13.0**	**7**	**42.9**	**-15.1**

	11	11.2	-16.2			
M06-2X (54)	17	6.1	-9.3	12	5.1	-9.9
	16	0	-11.7	11	0	-11.1
	15	2.2	-14.0	10	6.6	-13.4
	14	0	-15.0	**7**	**60.6**	**-18.2**
	13	28.1	-15.9			
	12	12.7	-16.8			
	11	**31.4**	**-18.4**			
	10	13.2	-20.2			

Water-Cu(II) interactions: Jahn-Teller distortion and σ-bond formation

The predominant Cu($3d$) contributions to α-spin molecular orbitals are shown in Figure 2.3 for anhydrous (D_{4h}), monohydrated (C_{2v}) and dihydrated (D_{2h}) $\mathrm{Cu_2(O_2C_7H_5)_4}$. Anhydrous and dihydrated $\mathrm{Cu_2(O_2C_7H_5)_4}$ belong to the dihedral point-group D, forming linear combinations of both Cu($3d$)-orbitals. The reduction of the point-group upon monohydration eliminates the degeneracy of the d_{yz} and d_{xz} orbitals. Here, water is adsorbed along the x-direction. Geometric parameters of anhydrous, monohydrated and dihydrated $\mathrm{Cu_2(O_2C_7H_5)_4}$ are reported in Table 2.3. The O_y-Cu-O_y angle reduces from 172 to 165.6°, causing the coordination bond to elongate. This is accompanied with an increase in the Cu-Cu distance of 0.034 Å. The most noticeable change is observed for the Cu($3d_z$)-orbital that is raised considerably in energy, from -11.1 to -9.3 eV.

The energy decomposition of the $\mathrm{Cu_2(O_2C_7H_5)_4}$-water interaction is presented in Table 2.4 and shows that the A1-irrep is most dominant contribution to the orbital interactions. Molecular orbital analysis of the A1-irrep reveals Pauli repulsion between the HOMO-1 of water and Cu($3d(z2)$)-orbital as shown in Figure 2.4. The Pauli repulsion is stabilized by favorable donor-acceptor interactions between the HOMO(A1) of water and the empty Cu($4p_z$) and Cu($4s$)-orbitals.

A recent electron paramagnetic resonance study hypothesized the formation of a σ-bond between the Cu(II)-cations upon water adsorption.[127] The vacant

Table 2.3: *Geometric parameters (Å) of anhydrous, monohydrated and dihydrated* $\mathrm{Cu_2(O_2C_7H_5)_4}$. *Water adsorbs along the* x*-direction.*

	Cu-Cu	Cu-O_x	Cu-O_y	O_y-Cu-O_y	Sym.
anhydrous	2.517	1.962	1.962	172.0	D_{4h}
monohydrated	2.551	1.979	1.997	165.6	C_{2v}
dihydrated	2.592	1.990	1.983	170.4	D_{2h}

Table 2.4: *Energy decomposition analysis (kcal·mol^{-1}) for water and $Cu_2(O_2C_7H_5)_4$. Orbital interaction components have been corrected for electronic preparation energy.*

ΔE_{Pauli}	ΔV_{elstat}	$\Delta E_{\text{oi}}^{\text{A1}}$	$\Delta E_{\text{oi}}^{\text{A2}}$	$\Delta E_{\text{oi}}^{\text{B1}}$	$\Delta E_{\text{oi}}^{\text{B2}}$	ΔE_{disp}	ΔE_{int}
27.26	-24.48	-10.15	-2.44	0.87	0.82	-3.36	-11.48

LUMO+6(A1) of $Cu_2(O_2C_7H_5)_4$, shown on the right-hand side of the MO diagram in Figure 2.4, consists of symmetric combinations of the Cu($4p_z$)-orbitals. These SFOs are populated upon water adsorption, hence forming a σ-bond. It should be noted that the occupation of this orbital appears to be functional dependent. Hybrid functionals show the filling of the symmetric Cu($4p_z$)-orbital but some GGA-functionals do not.

The higher adsorption energy of the water molecule on the opposite Cu-site (-10.13 kcal·mol^{-1}) compared to the adsorption energy of the first water molecule (-11.48 kcal·mol^{-1}) is in agreement with previous work.[138] At low water loadings this suggest that not all dicopper-sites are occupied. A rationale for this effect is the filling of the Cu($4s$) and Cu($4p_z$)-orbitals on the opposite copper-site due to electron donation in the LUMO+6(A1) as shown in Figure 2.4. Voronoi deformation density (VDD) charges confirm this charge accumulation. The copper-cations have positive VDD charges (548 mili-a.u.) in the anhydrous structure whereas the VDD charges for the monohydrated structure are less positive (505 and 541 mili-a.u.), meaning net a smaller loss of electrons.

Dihydrated $Cu_2(O_2C_7H_5)_4$ exhibits similar electronic interactions as monohydrated $Cu_2(O_2C_7H_5)_4$. The molecular orbital interaction diagram is presented in Figure 2.5. The D_{2h} point-group has symmetric (A.g) and anti-symmetric (B1.u) orbital contributions of the water molecules. The formation of the σ-bond is again evident from SFO gross population analysis as the LUMO+3(A.g) becomes populated. The Cu-Cu distance is increased by 0.041 Å and the Cu-O$_x$ distance is elongate with 0.011 Å suggesting weakening of the coordination bond. These elongations are in agreement with extended X-ray absorption fine structure (EXANES) experiments.[175]

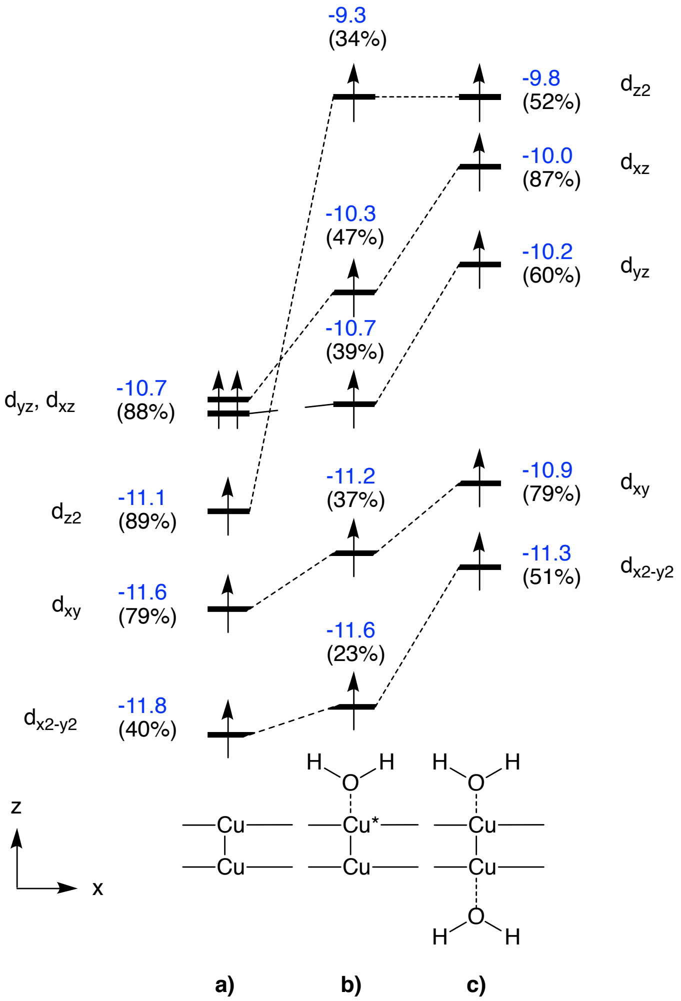

Figure 2.3: *Energy levels of α-spin molecular orbitals with predominant Cu($3d$)-character in a) anhydrous, b) monohydrated and c) dihydrated $Cu_2(O_2C_7H_5)_4$. Anhydrous and dihydrated clusters contain linear combination of the copper orbitals. The Cu($3d$)-orbitals of the monohydrated structure are of Cu*. Contributions are given in parenthesis. Energy levels (eV) are denoted in blue.*

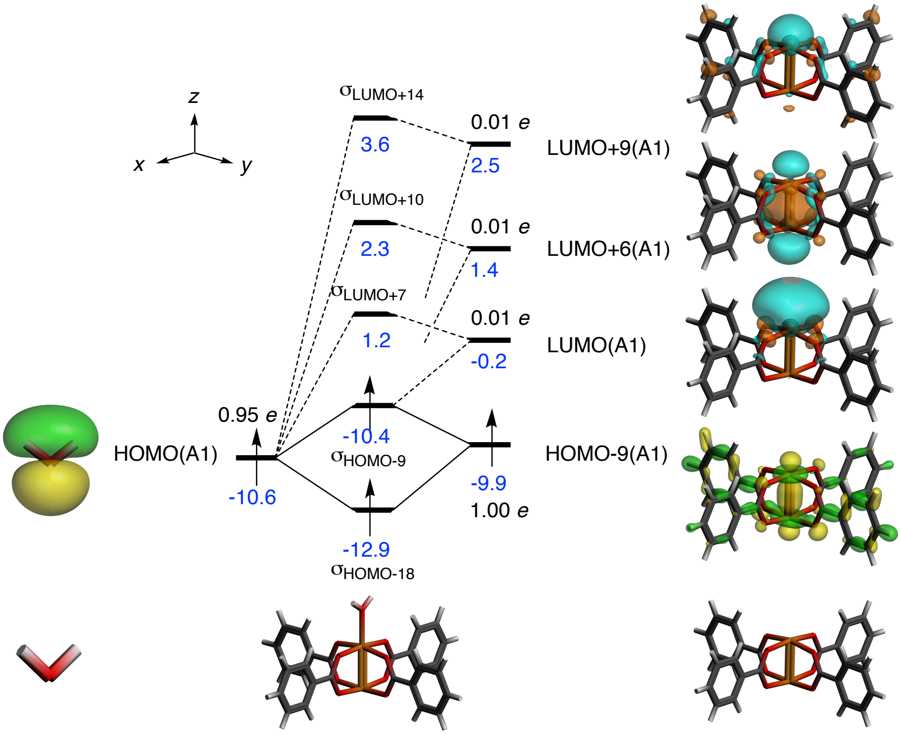

Figure 2.4: *Simplified α-spin molecular orbital interaction diagram of the A1-irrep of monohydrated $Cu_2(O_2C_7H_5)_4$. Pauli repulsion between HOMO(A1) of water and HOMO-9(A1) of $Cu_2(O_2C_7H_5)_4$ (predominantly $3d(z2)$-character) is stabilized by donor-acceptor interactions due to electron density acceptance of copper $4s$, $4pz$ and $5s$. The LUMO+6 contains symmetric $4pz$-orbitals, creating a σ-bond along Cu(II)-Cu(II). Energy levels (eV) are denoted in blue. Isovalue is 0.03 e^-/a_0^3.*

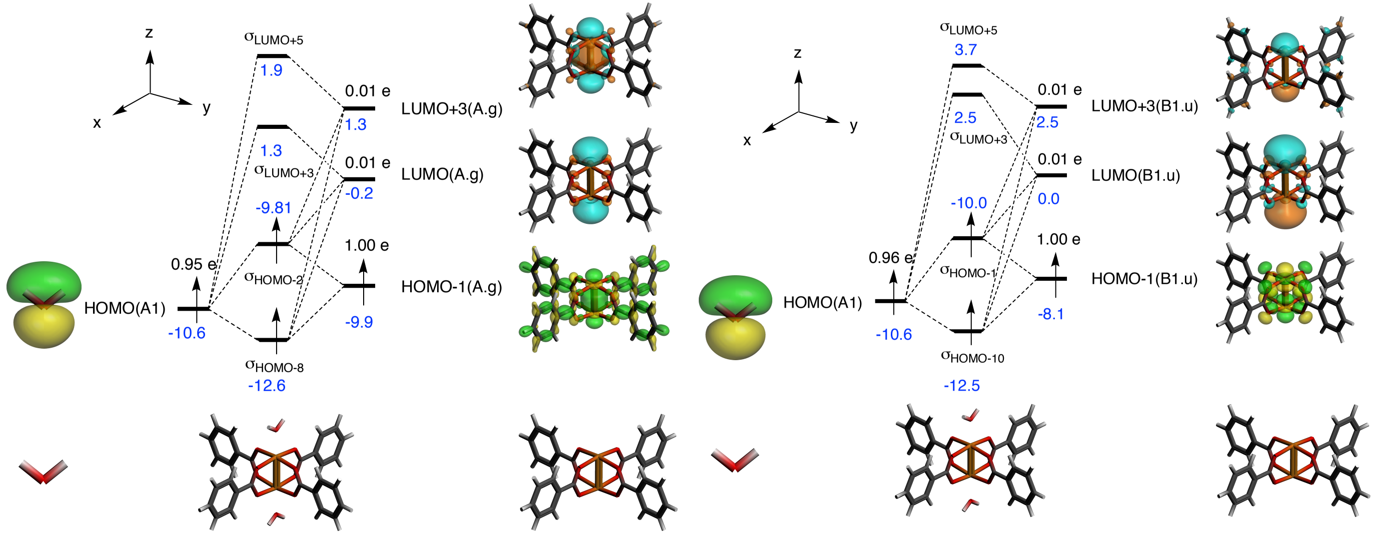

(a) *A.g* **(b)** *B1.u*

Figure 2.5: *Simplified α-spin molecular orbital interaction diagram of (a) symmetric (A.g) and (b) anti-symmetry (B1.u) water-combinations of dihydrated Cu$_2$(O$_2$C$_7$H$_5$)$_4$. Donor-acceptor interactions between the HOMO(A1) of water and the vacant Cu($4s$) and Cu($4p_z$) stabilize the Pauli repulsion between the HOMO(A1) of water and the Cu($3d_{z2}$)-orbital. Energy levels (eV) are denoted in blue. Isovalue is 0.03 e^-/a_0^3.*

2.5 Conclusion

Molecular orbital analysis combined with gross population analysis and an energy decomposition analysis scheme confirms the creation of a σ-bond between the Cu(II)-cations upon hydration of open-metal site. For monohydration, a Jahn-Teller distortion is observed due to Pauli-repulsion of the HOMO-1 of water and the Cu($3dz$)-orbital. The filling of empty orbitals on the opposite Cu-cation explains the reduced adsorption energy when water adsorbs on that Cu-site.

CHAPTER 3

Predicting multicomponent adsorption in open-metal site MOFs using energy decomposed DFT-based force field calculations

For the design of adsorptive-separation units, knowledge is required of the multicomponent adsorption behavior. Ideal adsorbed solution theory (IAST) breaks down for olefin adsorption in open-metal site (OMS) materials due to non-ideal donor-acceptor interactions. Using a density functional theory-based energy decomposition scheme, a physically justifiable classical force field is developed that incorporates the missing orbital interactions using an appropriate functional form. This first-principles derived force field shows greatly improved quantitative agreement with the inflection points, initial uptake, saturation capacity, and enthalpies of adsorption obtained from inhouse adsorption experiments. While IAST fails to make accurate predictions, the improved force field model is able to correctly predict the multicomponent behavior. It is expected that this approach is also transferable to other OMS structures, allowing the accurate study of their separation performances for olefins/paraffins and further mixtures involving complex donor-acceptor interactions.

Based on: J. Heinen, N.C. Burtch, K.S. Walton, C. Fonseca Guerra and D. Dubbeldam, *Predicting Multicomponent Adsorption Isotherms in Open-Metal Site Materials using Force Field Calculations based on Energy Decomposed Density Functional Theory*, Chemistry - A European Journal, **2016**, 22, 18045-18050

3.1 Introduction

An energy-efficient alternative for distillation techniques used in the chemical industry for olefin/paraffin separations are adsorption-based separation processes.[176] In adsorption-based separation processes, a porous material can be used as a sorbent, which acts as a molecular sieve. Most literature regarding the adsorptive separation performance of sorbents only provide single component adsorption isotherms, but information on the multicomponent adsorption behavior is crucial for the design of separation units.[177] It is extremely challenging to measure multicomponent adsorption isotherms experimentally,[178] and therefore this behavior is often predicted from single component isotherms using the well-known ideal adsorbed solution theory (IAST) introduced by Myers and Prausnitz.[179] IAST is based on three assumptions: (1) all adsorbates have access to the same surface area of the sorbent, (2) the sorbent is inert, and (3) the mixture in the adsorbed phase behaves as an ideal solution at constant temperature and spreading pressure.

The spreading pressure π can be thought of as the negative of the surface tension and can be calculated via the Gibbs isotherm[179]

$$\frac{\pi A}{RT} = \int_0^{f_i^0} q_i \, \mathrm{dln}\, f_i \tag{3.1}$$

with A the surface area of the sorbent, R the gas constant, T the temperature, f_i^0 the fugacity for component i when adsorbed, q_i the single component i adsorption isotherm and f_i the component fugacity of the bulk phase which is obtained via the Peng-Robinson equation of state.[109] At equilibrium, the spreading pressures of all components are equivalent. In an ideal adsorbed phase an analog of Raoult's law can be written

$$f_i = f_i^0(\pi) x_i \tag{3.2}$$

with x_i being the mole fraction of component i in the adsorbed phase (note that $\sum x_i = 1$). The total adsorption capacity q_T is obtained from

$$\frac{1}{q_T} = \sum_i^N \frac{x_i}{q_i} \tag{3.3}$$

with $q_i = x_i q_T$. Generally, IAST provides accurate results for MOFs.[180]

MOFs containing open-metal sites (OMS) are very promising materials for the separation olefin/paraffin mixtures.[121] Here, the bonding π-orbital of the olefin donates electron density into vacant orbitals of the metal. Simultaneously, the metal donates electron density into the antibonding π*-orbital of the olefin as explained by the Dewar-Chatt-Duncanson theory.[181–183] This bonding and back-bonding is commonly referred to as π-complexation. However, these donor-acceptor interactions also introduce non-idealities in the adsorbed phase that causes the third assumption of IAST to break down as shown later on.

Multicomponent adsorption isotherms can be directly computed using grand-canonical Monte Carlo simulations.[184,185] Unfortunately, Generic Hydrocarbon

Force Fields (GHFFs), such as from Liu *et al.*,[186] only consider electrostatic and non-covalent interactions and do not capture the donor-acceptor interactions between the OMS and the olefin. In this work, HKUST-1 is considered as sorbent material.[122] HKUST-1 is an oxo-bridged dinuclear copper(II) structure that forms a paddle-wheel structure with four main adsorption sites, as shown in Figure 3.1.[187]

A new approach for identifying and calibrating a double-bond-OMS interaction potential is developed using density functional theory calculations. To validate the Dewar-Chatt-Duncanson-theory, a molecular orbital diagram for ethylene adsorption on the OMS of HKUST-1 is constructed. Using an energy decomposition analysis scheme[84,188] as implemented in the ADF-package,[78–80] the orbital interactions missing in GHFFs are rationalized and incorporated into the force field model with an appropriate functional form. This approach allows a quantitative correct description of the interactions. The simulated single component adsorption isotherm resulting from the improved force field model also reproduces the experimental isotherm, in semi-logarithmic scale, which is important to properly analyze the low pressure regimes and the locations of inflection points.[189]

Past studies have not physically justified these functional forms and they were added rather *ad hoc*.[190–192] Sholl *et al.* reviewed recently the latest developments in first principle derived force fields and reported that two other groups use a decomposition scheme to derive force field potentials.[193] Schmidt *et al.* uses Symmetry-Adapted Perturbation Theory (SAPT) DFT to parameterize all force field potentials.[194] Gagliardi *et al.* employs the Non-Emperical MOdel po-

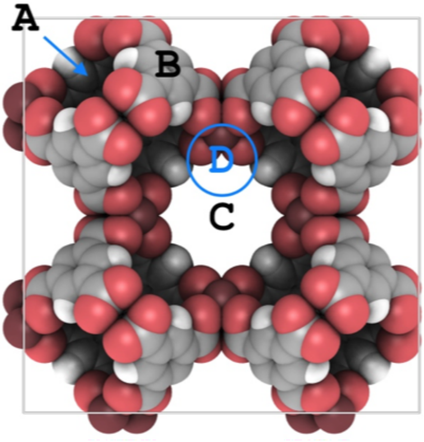

Figure 3.1: *Space filling model of the primitive unit cell of HKUST-1. HKUST-1 has four distinct adsorption sites for small molecules: (A) inside the side pocket, (B) near the linker, (C) inside the large cavities, and (D) at the open-metal site. Color legend: C (gray), O (red), H (white), Cu (brown).*

tential (NEMO) approach with computational expensive MP2 calculations as a reference.[195]

3.2 Experimental methodology

Synthesis of HKUST-1

Two synthesis routes for HKUST-1 were considered.[196,197] Reagents: copper(II) nitrate trihydrate ($Cu(NO_3)_2{\cdot}3H_2O$): Acros Chemicals, CAS: 10031-43-3, 99% pure; benzene-1,3,5-tricarboxylate (BTC): Sigma-Aldrich, CAS: 554-95-0), 95% pure; copper(II) acetate (Cu(OAc)): Acros Chemicals, CAS: 142-71-2, 99% pure.

Sample A: 1.17 g (4.84 mmol) $Cu(NO_3)_2{\cdot}3H_2O$ was dissolved in DI-H_2O and 0.49 g of BTC was dissolved in 25 mL of DMF (sonicated for 5 min). The mixture was stirred for 15 min. Sample B: 0.97 g (4.84 mmol) of Cu(OAc) was dissolved in DI-H_2O and 0.49 g of BTC was dissolved in 25 mL EtOH (sonicated for 5 min). The mixture was stirred for 35 min and sonicated for 15 min. Samples were transferred in 20 and 40 mL vials and put in a Fischer Scientific Isotemp Lab Oven at 373 K for 19 h. Samples were washed and filtered with DI-H_2O and the solvent used for BTC.

Material characterization

Powder X-ray diffraction patterns (PXRD) were recorded on an X'Pert X-ray PANalytical diffractometer with an X'accelerator module using Cu K_α ($\lambda = 1.5418$ Å) radiation at room temperature, with a step size of 0.02 in 2θ. N_2 adsorption was performed at 77 K after activation at 423 K using a Quadrasorb system (Quantachrome Instruments). The surface area was determined using BET theory and were 1950 and 1750 m^2/g for samples A and B, respectively.[10]

Measuring adsorption isotherms

A Gravimetric Analyzer (IGA-1 series, Hiden Analytical Ltd.) was used to obtain single component ethylene adsorption isotherms at $T =$ 323, 303 and 283 K and pressures up to 20 bar. Samples were activated *in situ* at 473 K under ultra-high vacuum (10^{-3} mbar) until no further weight loss was observed. A sample size of approximately 20 and 30 mg for sample A and B respectively was used for the measurements. A maximum equilibration time of 60 min was used for each point in the isotherm and at least 10 minutes were waited before recording equilibrium. Thermogravimetric analysis (TGA) was carried out in the temperature range of 303-983 K on a NET- ZSCH STA 449 F1 Jupiter under helium with a heating rate of 5 K/min and flow rate of 20 mL/min.

3.3 Computational methodology

Density functional theory calculations

The Amsterdam Density Functional (ADF)[78–80] package was used with a TZ2P-STO basis set and the M06-L exchange-correlation functional. It has been argued that the M06-L functional performs well for open-shell singlet system and when dispersion interactions are important.[154,198,199] Also, the XC-functional benchmark of the previous chapter suggests that M06-L is a good choice. Ethylene adsorption was performed using the triplet spin configuration. Hijikata *et al.* suggested that hydrogen termination was sufficient for the cluster model.[141] No significant differences were observed when comparing geometric and electronic properties of a phenyl-terminated cluster system with a hydrogen-terminated cluster. The interaction energies are calculated as described in section 1.1.

Force field calculations

Grand-canonical Monte Carlo simulations were performed using the RASPA-2.0 package.[116] Partial atomic charges and Lennard-Jones parameters were taken from Gutirrez-Sevillano *et al.*[187] and the generic DREIDING force field,[200] respectively. The Van der Waals cut-off radius was set to 12.0 Å. Configurational bias Monte Carlo was used in order to increase the acceptance ratio of insertions at higher loadings.[201–203] Lennard-Jones parameters for ethane and ethylene and the bonding parameters of ethane were used from Liu *et al.*[186] and are summarized in Table 3.1. Figure 3.2 shows HKUST-1 labels used for the force field. The helium void-fraction (0.7435) was determined using Widom particle insertion method in order to convert absolute into excess adsorption.[204] For the IAST calculations, the adsorption isotherms were fitted to a triple-site Langmuir-Freundlich model

$$q(f) = \sum_{i=1}^{3} q_{i,sat} \frac{K_i f^{n_i}}{1 + K_i f^{n_i}} \tag{3.4}$$

where i indicates the adsorption site, q is the amount of ethylene/ethane adsorption at fugacity f, $q_{i,sat}$ is the adsorption capacity of the adsorption site i, K_i is the Langmuir (affinity) constant of adsorption site i and n_i is an index of heterogeneity.

Table 3.1: *Lennard-Jones parameters and partial atomic charges taken from Gutiérrez-Sevillano et al. and DREIDING.*[187,205] *The σ-parameters of O and Cu have been modified as described in the main text. Ethylene and ethane parameters are used from Liu et al.*[186] *COM: center of mass.*

	ϵ/k_B (K)	σ (Å)	q
HKUST-1 C1	47.86	3.47	-0.156
HKUST-1 C2	47.86	3.47	0.130
HKUST-1 C3	47.86	3.47	0.494
HKUST-1 O1	48.19	2.63	-0.624
HKUST-1 H1	7.65	2.85	0.156
HKUST-1 Cu1	2.518	2.414	1.248
ethylene CH_2	93.0	3.685	0
ethylene COM	0	0	0
ethane CH_3	108.0	3.76	0

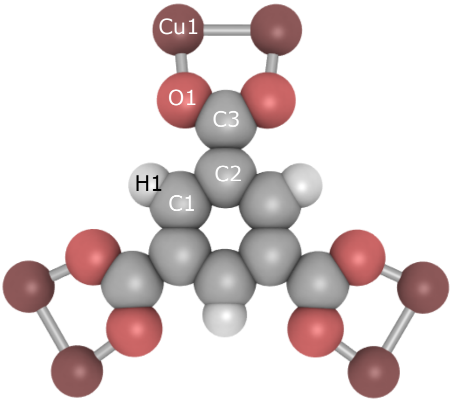

Figure 3.2: *Labels of HKUST-1 used to describe the force field. Color legend: C (gray), O (red), H (white), Cu (brown).*

The enthalpy of adsorption ΔH at constant loading q was calculated using the Clausius-Clapeyron equation and the particle-energy fluctuation theorem.[206] The Clausius-Clapeyron equation reads

$$\Delta H = R\left[\frac{\partial \ln p}{\partial(1/T)}\right]_q \tag{3.5}$$

with R being the universal gas constant, p the pressure and T the temperature. The pressure and loading are related by an isotherm model, such as the triplet-site Langmuir-Freundlich. The enthalpy of adsorption is also obtained from the particle-energy fluctuation theorem

$$\Delta H = \frac{\langle U \times N \rangle_\mu - \langle U \rangle_\mu \langle N \rangle_\mu}{\langle N^2 \rangle_\mu - \langle N \rangle_\mu \langle N \rangle_\mu} - \langle U_g \rangle - \frac{1}{\beta} \tag{3.6}$$

where $\langle \cdot \rangle$ denotes the grand-canonical average, N is the number of adsorbate molecules and μ is the chemical potential of the adsorbates, $\langle U_g \rangle$ the energy of an isolated adsorbate molecule and β is the inverse temperature.

3.4 Results and discussion

The DFT adsorption energy of ethylene at the OMS of HKUST-1, $\Delta E_{\text{ads}} =$ -10.92 kcal·mol^{-1}, is decomposed and the orbital interaction is given per its irreducible representation (irrep) of the $C_{2\text{v}}$ point group in Table 3.2. The stabilizing orbital interaction ΔE_{oi} and electrostatics ΔV_{elstat} are -9.63 and -16.27 kcal·mol^{-1}, respectively. These ratios are similar to the ratios found for other non-covalent interactions, such as hydrogen bonds.[207] The A1-irrep contributes predominantly to the orbital interactions.

The dominant donor-acceptor interactions, evident from the gross populations, that contribute to the orbital interaction energies of the A1 and B2-irreps are shown in Figure 3.3 at their equilibrium distance. In the A1-irrep, electron density is donated from the π-HOMO of ethylene into the LUMO+1 (A1) and LUMO+2 (A1) of HKUST-1 which have predominantly Cu($4s$) and Cu($4p_z$) character. The Cu($3d_{yz}$) and $2p_z$-orbitals of the adjacent oxygens donate electron density into the π-LUMO of ethylene in the B2-irrep. Here, Pauli repulsion between the HOMO(B2) of ethylene and the HOMO(B2), HOMO-1(B2) and HOMO-3(B2) of HKUST-1 is stabilized by this donor-acceptor interaction.

Table 3.2: *Bond energy analysis (kcal·mol^{-1}) of ethylene adsorbed on the OMS of HKUST-1. *metaGGA correction for ΔE_{oi}*[208]

ΔE_{ads}	$\Delta E_{\text{oi,A1}}$	$\Delta E_{\text{oi,A2}}$	$\Delta E_{\text{oi,B1}}$	$\Delta E_{\text{oi,B2}}$	ΔE^*	ΔE_{Pauli}	ΔV_{elstat}
-10.92	-6.55	-2.06	-0.81	-1.81	1.6	14.99	-16.27

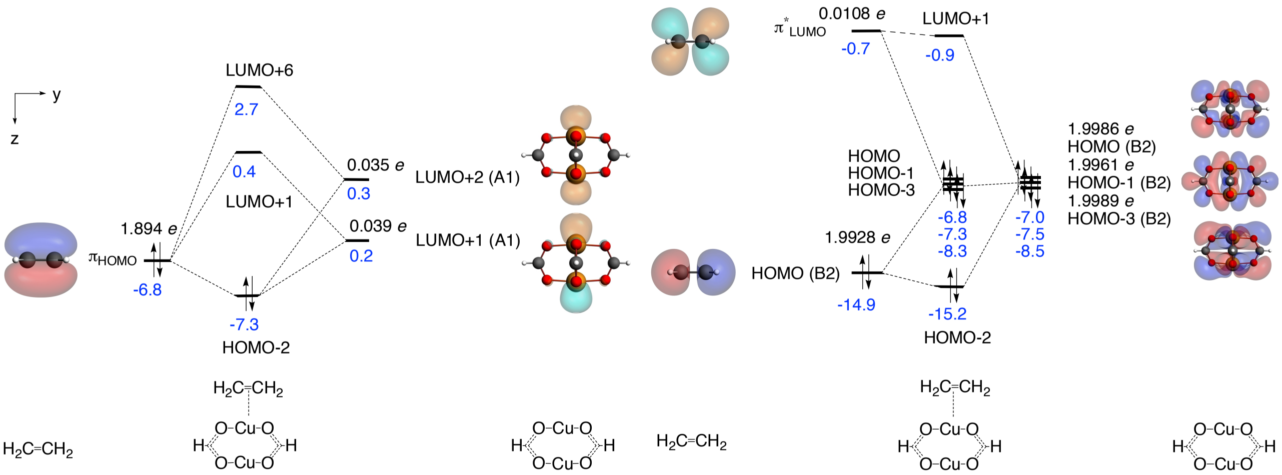

(a) *A1-irrep* **(b)** *B2-irrep*

Figure 3.3: *Molecular orbital diagrams of donor-acceptor interactions between ethylene and the OMS of HKUST-1 in the (a) A1 and (b) B2 irreducible representation. The π-HOMO and π^*-LUMO of ethylene donate and accept electron density, respectively. The Cu($4s$) and Cu($4p_z$) orbitals accept electron density, and the Cu($3d_{yz}$) orbital and O($2p_z$) and O($2p_y$) orbitals donate electron density. Energy levels (eV) are denoted in blue. Isovalue is 0.03 e^-/a_0^3.*

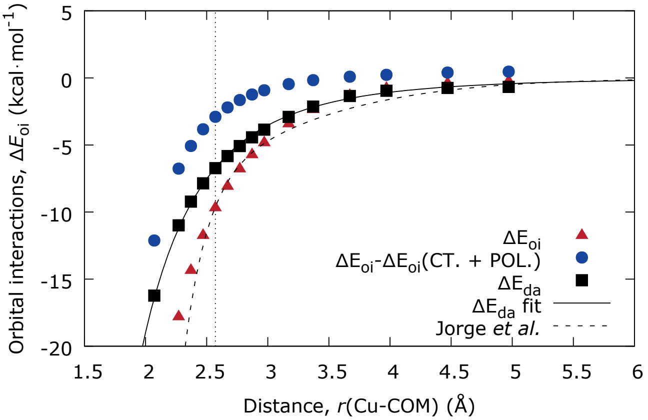

Figure 3.4: *Orbital interaction ΔE_{oi} between ethylene and the OMS of HKUST-1 as a function of Cu-Center Of Mass (COM) distance. Red triangles: all unoccupied orbitals present, blue circles: unoccupied Cu(A1) and ethylene(B2) orbitals involved in polarization and charge transfer between both fragments removed, black squares : difference between aforementioned points. Solid line: power function fitted to squares. Dashed line: Cu-π interaction energy determined by Jorge et al.*[190] *Equilibrium distance at 2.571 Å is given by the black dotted line.*

In terms of orbital theory, the difference between polarization and charge transfer is well-established. Polarization involves mixing of occupied and virtual orbitals on the same fragment whereas charge transfer involves mixing between the fragments. However, it is non-trivial to separate these effects at close *inter*molecular distances and using finite basis sets.[209,210] It can be argued that charge transfer is an extreme case of polarization when two interacting fragments are sufficiently close to one another.

Removing the unoccupied B2-irrep orbitals from the basis set of ethylene should eliminate back-bonding, if present initially, since no electron density can then be donated into the empty π^*-LUMO. This is observed in two ways. Firstly, gross populations confirm that the HOMO(B2), HOMO-1(B2) and HOMO-3(B2) of HKUST-1 are 2.000, suggesting that donation is eliminated. Secondly, Voronoi deformation density charges on ethylene confirm charge depletion upon removal of the unoccupied orbitals of ethylene in the B2-irrep.[211] Furthermore, natural orbitals for chemical valence analysis[212] showed two dominant channels that confirm charge transfer in both directions. However, this neither confirms nor excludes that polarization in ethylene occurs at their equilibrium distance.

Figure 3.4 shows the orbital interactions ΔE_{oi} between the fragments as function of the distance between Cu and the center of mass (COM) of ethylene. Removing the unoccupied orbitals from the basis set of the fragments that accept electron density, results in more positive ΔE_{oi} values, as indicated by the circles in Figure 3.4.

The difference between these two systems is given by squares and are the donor-acceptor (da) energetics that are missing in GHFFs. Fitting these data points to a power law gives the following (in kcal·mol^{-1})

$$\Delta E_{\mathrm{da}} = \frac{-336.42}{r^{4.1}}. \tag{3.7}$$

Interestingly, the functional form of Equation (3.7) is in close agreement with a 1/r^4 potential for ion-induced dipole interactions.[213] Note that the OMS-ethylene system can be considered as an ion-induced dipole interaction.

Jorge *et al.* also extracted the orbital interaction energetics using the Weeks-Chandler-Anderson (WCA)[214] separation of interaction, denoted Cu-π in their work, which is given by the black dashed line in Figure 3.4.[190,191] At equilibrium distance there is a 2.88 kcal·mol^{-1} overestimation of the orbital interactions. We argue that using the ADF decomposition scheme that calculates the orbital interaction term from first principles should provide more accurate results than using an empirical WCA-scheme for determining the missing orbital interactions.

Incorporation of Equation (3.7) as an additional functional form in the force field, generates a new adsorption site. This is evident by the formation of an extra peak in the host-adsorbate energy distribution and the adsorbate snapshots, given in Figure 3.5. Without Equation (3.7) adsorption site (A) is the strongest site for olefins, but with the addition of the new potential the OMS (D) is the dominant interaction.

Figure 3.6a shows the computed and experimental single component ethylene adsorption isotherm. Their is poor agreement between the GHFF (diamonds) and the experimental single component adsorption isotherm (open triangles) at 323 K. The saturation capacity of the GHFF is roughly 2 mol/kg too low compared to the experimental value. By plotting the isotherm in semi-log scale, the energetic-dominated regime of the isotherm becomes visible. The absence of inflection points in the isotherm suggests that essential physics (*e.g.*, adsorption sites) are missing. As a result, the loading at lower pressures and the enthalpy of adsorption are severely underestimated compared to the experimental values.

The experimental (open symbols) and the DFT-derived (closed symbols) adsorption isotherms at various temperatures show good quantitative agreement. The competition between adsorption site (A) and site (D) leads to inflections in the single component adsorption isotherm. A slightly lower saturation capacity and a less pronounced inflection in the experimental isotherm compared to the simulated isotherm is not uncommon and can be attributed to imperfections, such as defects in the HKUST-1 crystals and the influence of framework flexibility.[215] At decreasing temperature, the inflection (plateau formation) becomes more pronounced. Compared to higher temperatures, the OMS is predominantly filled first. Also, the probability distribution at peak (D) in Figure 3.5 increases, indicating competition between the OMS and other adsorption sites. In order to reduce repulsive behavior and thus reproduce classically the DFT calculated Cu-ethylene

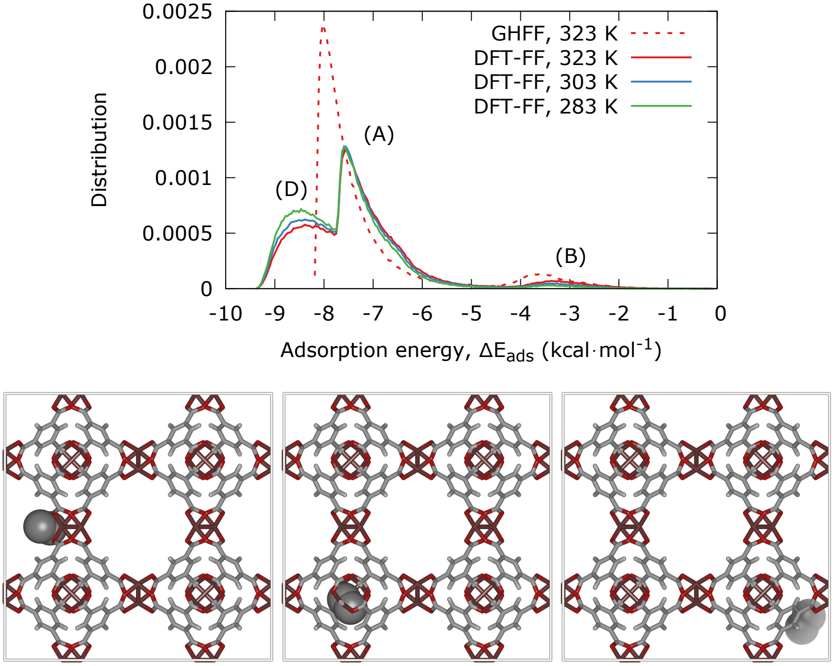

(D) *(A)* *(B)*

Figure 3.5: *(top) Host-adsorbate interaction energy using a GHFF and the DFT-derived force fields. (bottom) Snapshots of adsorbed ethylene at various sites in HKUST-1 calculated using the DFT-derived force field. Corresponding adsorption energies are (D) OMS -8.63 kcal·mol^{-1} (A) small pocket -6.53 kcal·mol^{-1} (B) aromatic ring -3.68 kcal·mol^{-1}. Color legend: C (gray), H (white), O (red), Cu (brown).*

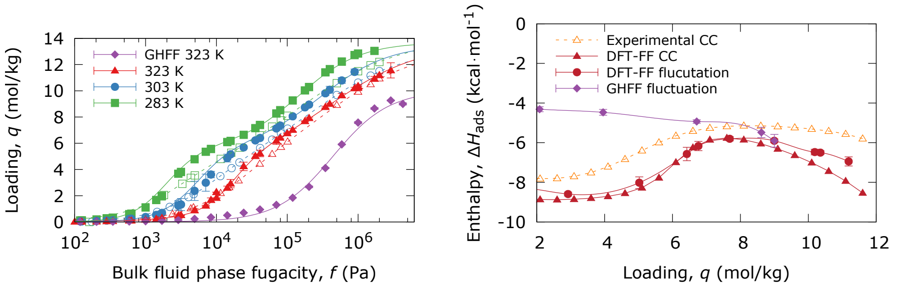

(a) **(b)**

Figure 3.6: *(a) Experimental (open symbols) and simulated (closed symbols) ethylene single component adsorption isotherms at T = 283, 303 and 323 K. A dual-site Langmuir-Freundlich model is fitted to the experimental (dashed) and simulated (solid) data points. (b) Finite-loading enthalpy of adsorption of ethylene in HKUST-1 at T = 323 K computed using the Clausius-Clapeyron (CC) equation and particle-energy fluctuation theorem.*[206]

distance, the σ values of the Cu and adjacent O had to be lowered.

The enthalpy of adsorption is plotted in Figure 3.6b. The GHFF does not qualitatively captures the experimentally observed inflections. Although the computed enthalpy of adsorption is shifted by 1-2 kcal·mol^{-1} compared to the experimental enthalpy of adsorption, the overall trend is captured very well and also agrees with the values from He *et al.*[216] The enthalpy of adsorption becomes less exothermic at around 5.5 mol/kg, corresponding to the plateau formation in the adsorption isotherm. Furthermore, the enthalpy of adsorption at infinite dilution lies at around -8 kcal·mol^{-1} which is reasonably close to the host-adsorbate energy near -8.63 kcal·mol^{-1} at peak (D) in the host-adsorbate energy distribution profile in Figure 3.5.

Figure 3.7 shows the multicomponent adsorption isotherms of an equimolar mixture of ethylene and ethane as well as the associated IAST curves for the GHFF (Figure 3.7a) and the DFT-derived force field (Figure 3.7b). Clearly, for GHFFs, IAST shows excellent agreement with the Monte Carlo simulations. However, when the OMS site (D) is properly taken into account by using the DFT-derived force fields, IAST fails at higher pressures as shown in Figure 3.7b. Primarily, the calculated isotherms differ considerably between GHFF and the DFT-derived force field. Using the GHFF, ethylene is servery underestimated over the entire pressure range. Importantly, at industrially relevant pressures, the GHFF (and IAST) incorrectly predicts that ethane is preferably adsorbed over ethylene in HKUST-1. Turing towards the DFT-derived force field (Figure 3.7b), IAST over- and underestimated ethylene and ethane saturation capacity by approximately 30% and 50%, respectively. At higher ethylene mole fractions, IAST predicts the ethylene adsorption behavior more accurately than in mixtures at lower mole fractions, although ethane loadings are still heavily underestimated in these cases.

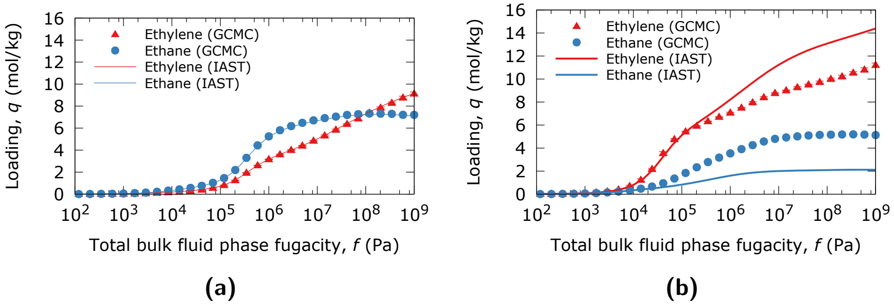

Figure 3.7: *Multicomponent adsorption isotherms of an equimolar ethylene (triangles) ethane (circles) mixture in HKUST-1 at $T = 323$ K calculated with (a) GHFF and (b) DFT-derived force field. IAST calculations are based on single component isotherms computed with the GHFF and DFT-derived force field.*

At lower ethylene mole fractions, IAST more poorly predicts the wrong saturation behavior of the entire mixture.

3.5 Conclusion

In this work, a combination of experimental and theoretical techniques was used to provide a fundamental understanding of the interaction of an unsaturated bond with an OMS. An energy decomposition analysis scheme together with the accompanying Kohn-Sham molecular orbital theory was used to get a fundamental understanding of the orbital interactions and to breakdown these interactions in chemically comprehensible terms. The dominant orbital interactions were captured in a charge-induced-dipole-like term and implemented into the force field. Using inhouse experiments, confirmation was obtained that this model is able to accurately predict adsorption isotherms that capture the isotherm inflections, heat of adsorption, initial uptake and saturation capacity in excellent agreement with experiment. Overall, this work demonstrates that using a multiscale modeling approach is important for the prediction of accurate multicomponent adsorption isotherms for mixtures containing olefin and paraffin molecules in OMS materials.

Acknowledgments

We would like to thank Ali Poursaeidesfahani for providing the IAST results, and Thijs Vlugt, Sofia Calero and Ariana Torres Knoop for useful discussion. This material is supported by The Netherlands Research Council for Chemical Sciences (NWO-CW), also through a VIDI grant (D.D.), and the National Science Foundation Graduate Research Fellowship and the Graduate Research Opportunities Worldwide (GROW) award under Grant No. DGE1148903 (N.C.B.). Work at

Georgia Tech was supported by UNCAGEME, an Energy Frontier Research Center funded by DOE, Office of Science, BES under Award #DESC0012577. We thank the Stichting Nationale Computerfaciliteiten (National Computing Facilities Foundation, NCF) for the use of supercomputing facilities.

CHAPTER 4

On flexible force fields for metal-organic frameworks

Classical force field simulations can be used to study structural, diffusion, and adsorption properties of MOFs. To account for the dynamic behavior of the material, parameterization schemes have been developed to derive force constants and the associated reference values by fitting on ab initio energies, vibrational frequencies, and elastic constants. Here, we review recent developments in flexible force field models for MOFs. Existing flexible force field models are generally able to reproduce the majority of experimentally observed structural and dynamic properties of MOFs. The lack of efficient sampling schemes for capturing stimuli-driven phase transitions, however, currently limits the full predictive potential of existing flexible force fields from being realized.

Based on: **a)** J. Heinen and D. Dubbeldam, *On Flexible Force Fields for Metal-Organic Frameworks*, WIREs Computational Molecular Science, **2018**, 8, e1363 & **b)** J. Heinen and D. Dubbeldam, Understanding and Solving Disorder in the Substitution Pattern of Amino Functionalized MIL-47(V), *Dalton Transactions*, **2016**, 45, 4309-4315

4.1 Introduction

The flexible behavior in MOFs can have important implications for application prospects by enabling, for instance, exceptional gas storage or separation performances that are not possible in traditional rigid materials.[42]

Selected large-scale flexible modes in MOFs are shown in Figure 4.1. The first two flexible modes have already been mentioned in the General introduction: a) negative thermal expansion in IRMOF-1 and b) breathing in MIL-53(Cr).

Figure 4.1a shows negative thermal expansion in IRMOF-1. The coefficient of thermal expansion can be influenced by changing the linker-length and by the presence of guest molecules.[217,218] Generally, adsorbates also stiffen the material as is evident from the increased elastic constants of Zn-MOF-74 and the increased shear and bulk modulus for ZIF-4 and ZIF-8.[219–221] Interestingly, it is argued that stiffening only occurs at high adsorbate loadings whereas at low loadings a reduction of the elastic constants is observed.[222]

The breathing mode in MIL-53(Cr) due to CO_2 adsorption is responsible for the distinctive stepped curvature of its CO_2 adsorption isotherm, displayed in Figure 3b.[25,223] Up until a loading of 2 mmol/g, the unit cell is in the *large pore* (*lp*) phase (Figure 4.1b, left), and beyond that it is in the *narrow pore* (*np*) phase (Figure 4.1b, right). These structural changes are reversible: at around 5 bar, the material transitions back towards its *lp* phase. Neimark *et al.* argued that a structural transformation is induced, if a certain threshold of adsorption-stress on the material has been reached.[224] The adsorption-stress is the derivative of the grand potential of the adsorbed phase per unit cell with respect to the unit cell volume. The predicted magnitude of the adsorption-stress needed to deform MIL-53(Cr) was found to be in agreement with the experimentally applied external mercury pressure.[225]

Figure 4.1c shows the *open* and *contracted* pore phase of MIL-88D: a chromium-based hexagonal MOF with 4-4'-biphenyldicarboxylate linkers. A swelling of 240% has been observed due to pyrdine adsorption.[28] The amplitude of the swelling can be controlled by linker functionalization which has strong applications in drug delivery.[226]

Negative gas adsorption is the spontaneous desorption of adsorbates at higher pressures and was recently observed in DUT-49 (Figure 4.1d).[227] In this structure, methane adsorption activates the *open* to *contracted* phase transition which occurs due to deformation of the linker.[228]

Another interesting phenomenon is the gate-opening behavior observed in ZIF-8 as shown in Figure 4.1e. Gate-opening occurs due to the rotation of its methyl-imidazolate linkers, which can have important implications for molecular separations and sensing devices.[229,230] The swing effect of the imidazolate linkers is expressed in an inflection point of the materials N_2 adsorption isotherm at 77 K around $p/p_0 \approx 2{\cdot}10^{-3}$ and $2{\cdot}10^{-2}$.[231] The exact transition pressure depends on the ZIF-8 particle size.[232]

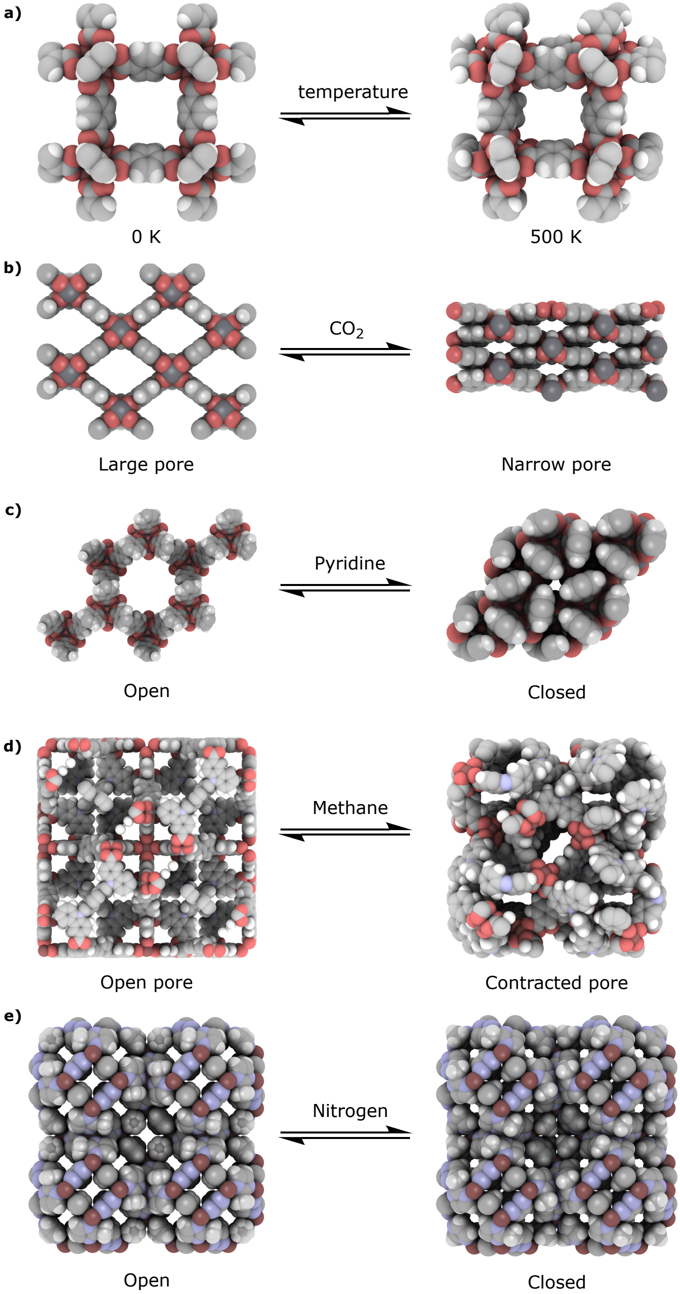

Figure 4.1: *Illustration of different flexibility behaviors reported in MOFs. (a) Negative thermal expansion in IRMOF-1, (b) breathing in MIL-53(Cr), (c) swelling in MIL-88D, (d) negative gas adsorption in DUT-49 and (e) gate-opening in ZIF-8. Color legend: C (light gray), O (red), H (white), N (blue), Cr (dark gray), Cu (brown), Zn (dark purple).*

The origin of these phenomena, as well as flexibility in MOFs in general, remains a highly active field of research.[22] Fundamental insight into these flexibility properties are usually obtained from a combination of experiments (*e.g.* terahertz vibration spectroscopy, X-ray diffraction, pair distribution functions) or *ab initio* calculations.[32,39,229] Tensorial analysis of the elastic constants has shown to be a powerful approach for elucidating flexible behavior in MOFs.[34,35,39,233,234] Softening of elastic constants can lead to negative eigenvalues of the elastic tensor. This violates the Born instability criteria and induces a phase transition.[235,236] The Born instability criteria and the assessment of the pressure-volume equation of state provides reliable information to identify mechanical stability in a broad range of MOFs.[43] Crystal-to-amorphous transitions have been attributed due to a reduction of the shear moduli.[39,221,237,238]

An interesting question is if chemical instability (*e.g.*, weak chemical bonds) is caused by mechanical instability (lowering of elastic moduli) or *vice versa*. Missing linkers in UiO-66 resulted in a decrease of the elastic moduli.[234] However, low elastic moduli imply that the material is more flexible and therefore can 'open up' more for water to hydrolyze coordination bonds.

Classical force field calculations can be used to understand MOF flexible properties. Considerable advances have already been made in this field and, as an example, several force field-calculated properties of IRMOF-1 are presented in Table 4.1. Some of these force field are discussed in the next section. Recently, Boyd *et al.* compared several generic force fields by computing bulk moduli and thermal expansion coefficients of various MOFs.[248] All force fields reproduced the experimental or *ab initio* calculated bulk moduli within 5 GPa. The expected

Table 4.1: *Lattice parameter a (Å), volumetric thermal expansion coefficient α_V (K^{-1}), bulk modulus B_0 (GPa) and Young's modulus E (GPa) of IRMOF-1. Experimental values are reported at 300 K, DFT and force field values are reported at 0 K, unless stated otherwise. [a] Young's modulus calculated using the ELATE code.,[239] [b] 10 K, [c] 300 K*

	a	$\alpha_V \cdot 10^{-6}$	B_0	E_{100}	E_{111}
Experimental[9]	25.885	-39[240]	-	7.9[241]	-
PW-91[241]	26.04	-	16.33	21.95	10.06
PBE-D3[242]	26.09	-	15.76	18.88	2.91
				17.7	2.5
Greathouse[243,244]	26.05	-36	20.0	35.5	-
				14.9	
Dubbeldam[217]	25.965	-55	17.71	2.90	22.42
Goddhard[245][b]	25.291	-23.91	19.37	42.73	5.29
				31.14	3.97
Schmid[246]	25.946	-	10.8[c]	-	-
Walsh[247]	25.901	-15.80	11.95	37.42[248]	1.19[248]

negative thermal expansion was also predicted, although the thermal expansion coefficients differ by up to 25 ppm/K.

Flexible force field models have the advantage of making material predictions at significantly lower computational costs than *ab initio* methods, provided an accurate force field model is available for the structure of interest. This motivates the discussion provided in later sections regarding different approaches for the development of suitable flexible force fields in MOFs.

4.2 Classical force field simulation methodology

The potential energy $\mathcal{U}$ appearing in Equation (1.13) consists of pre-defined interatomic potentials u expressed in physically meaningful terms such as bonding, bending and torsions

$$\begin{aligned}\mathcal{U} = &\sum_{\text{bonds}} u_b(\boldsymbol{r}) + \sum_{\text{bends}} u_\theta(\theta) + \sum_{\text{torsions}} u_\phi(\phi) + \sum_{\text{non-bonding}} u_{nb}(\boldsymbol{r}) \\ &+ \sum_{\text{out of plane bends}} u_\chi(\chi) + \sum_{\text{bond-bond}} u_{bb}(\boldsymbol{r},\boldsymbol{r'}) + \sum_{\text{bond-bend}} u_{b\theta}(\boldsymbol{r},\theta) \\ &+ \sum_{\text{bend-bend}} u_{\theta\theta'}(\theta\theta') + \sum_{\text{bond-torsion}} u_{b,\phi}(\boldsymbol{r},\phi,\boldsymbol{r'}) + \sum_{\text{bend-torsion}} u_{b,\phi}(\boldsymbol{r},\phi,\theta').\end{aligned} \tag{4.1}$$

A first order expansion of these terms (the harmonic approximation) requires only a force constant and a reference value. Equation (4.1) is therefore referred to as a *force field*. Higher order expansion and more terms in the force field make the calculations more accurate but also more expensive. There is always a trade-off between accuracy and computational cost. Specific force field potentials are sometimes required to describe polarization effects[249] or donor-acceptor interactions[250–253] in strongly interacting systems, such as open-metal site MOFs.[193,254]

Non-bonding interactions. Non-bonding interactions are usually divided into Van der Waals and electrostatic interactions. The Van der Waals interactions are dominant for physical adsorption processes.[255] For historical reasons, the (12-6) Lennard-Jones potential is widely used to describe Van der Waals interactions[256]

$$u_{ij}(r) = 4\epsilon_{ij}\left[\left(\frac{\sigma_{ij}}{r_{ij}}\right)^{12} - \left(\frac{\sigma_{ij}}{r_{ij}}\right)^{6}\right] \tag{4.2}$$

with ϵ and σ being the effective interaction and size parameters of a particle. The first term of the Lennard-Jones potential is the Pauli repulsion and dominates at short range whereas the second term is the attractive dispersion interaction. Most force fields specify the σ and ϵ per atom-type and use a set of mixing rules (*e.g.,* Lorentz-Berthelot, Jorgensen or Waldman-Halger) to calculate the interaction between two particles.

To represent the system's complex electrostatic potential classically, including multipole interactions, point charges must be assigned to the system. This can be done by minimizing an error-function of the *ab initio* calculated electron density and calculate atomic charges under the constraint that the total sum of the atomic charges equals the total charge of the system.[57] There is no unique method of constructing point charges as these are not quantum observables. For periodic systems, this can be done using the Repeating Electrostatic Potential Extracted ATomic (REPEAT) method.[257] Other commonly used periodic charge partitioning schemes include Density Derived Electrostatic and Chemical (DDEC)[138,258] and Hirshfeld.[259] Most partition schemes assign partial charges to the atoms instead of formal charges. The electrostatic energy is than computed according to

$$u_{ij}(r) = \frac{1}{8\pi\epsilon_0} \sum_{i \neq j} \frac{q_i q_j}{|\boldsymbol{r}_i - \boldsymbol{r}_j|} \tag{4.3}$$

where ϵ_0 is the electric permittivity of vacuum and q_i the partial charge of atom i. A factor $1/2$ is introduced into this expression to account for double counting. In order to avoid the non-converging behavior of Equation (4.3), the Ewald summation is used.[260]

The partial atomic charges assigned to the framework can heavily affect adsorbate uptake and separation selectivities.[261–263] Rescaling atomic charges with 0.95 and 1.05 showed an decrease (more negative) and an increase (less negative) of the coefficient of thermal expansion in IRMOF-1.[264] For structural transformations of the unit cell, the use of fixed charges becomes questionable since the true electrostatic potential energy surface also changes as the atomic positions change. Charge equilibriation schemes (CES) can provide an approximate solution by predicting atomic charges based on the current geometry and connectivity of the system.[265] The efficiency of CES also make them popular for large-scale screening studies of existing and hypothetical MOFS,[266] and, as such, these CES remain an active area of research in force field development.[267]

Barostats. To simulate lattice dynamics at finite temperature and pressure, the choice of the barostat that controls the volume changes is essential. Rogge *et al.* compared three barostat coupling schemes for reproducing cell parameters and pressure-volume behavior.[268] The Langevin[269,270] and Martyna-Tuckerman-Tobias-Klein[271,272] barostats gave similar results for reproducing lattice parameters. The bulk moduli of MIL-53(Al) and IRMOF-1 were found to be an order of magnitude larger for the Berendsen barostat[273] as compared to the other barostats.

Effect of framework flexibility. A much debated topic in literature is whether framework flexibility influences diffusion and adsorption properties. Dubbeldam *et al.* used the osmotic ensemble to assess the influence on the adsorption of CO_2 in IRMOF-1.[217] Little to no influence was found, as the equilibrium positions of the atoms in IRMOF-1 fluctuate around their equilibrium positions and large scale atomic rearrangements are absent in this structure. This was also found for CO_2 adsorption in NH_2-MIL-53(Al)[274] and in HKUST-1.[275] In Chapter 5 this is also illustrated for CO_2, CH_4 and n-hexane adsorption in MIL-47(V). Ghoufi *et al.* constructed a flexible force field that captured the *lp* to *np* and *np* to *lp* transition of carbon dioxide in MIL-53(Cr).[276] The adsorption enthalpies in both phases were in good agreement with the experimental values. When comparing the effect of framework flexibility, the rigid framework material should be obtained via a minimization procedure using the flexible force field. Most authors use an *ab initio* optimized structure as reference but this is inconsistent, since the material will move around the reference bonds, bends and torsions which are imposed by the flexible force field and these values are not necessarily the same equilibrium values found from *ab initio* calculations or experiments.[119] A requirement is therefore that the flexible structure should converge at low temperature to the rigid structure.[277] Stated oppositely, the rigid structure should be the 0 K optimized structure of the flexible model. This is important for comparing the effect of framework flexibility on adsorption processes.

It is expected that framework flexibility is crucial for confined systems.[278] However, extremely low acceptance ratio's of insertion moves involving high loadings and bulky adsorbates make this hypothesis not straightforward to test. Efficient schemes that tackle this problem are the continuous fractional component Monte Carlo (CFCMC) method by Maginn *et al.*[279] and the configuration bias continuous fractional component Monte Carlo (CBCFMC) by Torres Knoop *et al.*[280] For a mixture isotherm of xylenes in MTW, convergence is obtained using CBCFMC with about four times fewer production cycles that for configuration bias Monte Carlo.[280] However, for flexible materials, the unit cell volume change MC-move forms an additional problem. As the unit cell changes volume, all particles are displaced simultaneously which is often energetically unfavorable.[115] The most common approach to allow for unit cell volume changes is by means of a hybrid MD/MC scheme.[281,282] Here, one of the MC-moves is a short molecular dynamics run that results in higher acceptance probability.

4.3 Parameterization schemes

Developing flexible force field models involves the construction and parameterization of functional forms. The construction versus parameterization stages of determining these potentials should be distinguished. The functional form's construction involves deciding which mathematical forms should be used for the bonds, bends and torsions of the system to appropriately represent the material dynamics. For instance, this deals with the question: is a simple harmonic potential between the metal and the ligand atoms sufficient or is a more complex functional form such as the Morse potential needed. The parameterization stage deals with the separate question of: given a certain set a functional forms, what are the associated force constants and reference values that should be assigned?

Force fields for liquids and gases have been parameterized on experimental phase equilibria, typically in the form of vapour-liquid equilibrium data (TraPPE),[283,284] conformational energetics from *ab initio* calculations, (OPLS-AA)[285,286] heats of formation and vibrational spectra (MM3).[287] For solids, the choice of experimental observables with which to paramaterize the force field models is often less obvious. Zeolite force fields have been parameterized on experimental infrared spectra (Demontis *et al.*[288] and Nicholas *et al.*[289]), and *ab initio* cluster calculations (Hill and Sauer[290]). Core-shell zeolites models have been parameterized on elastic constants and relative permittivities.[291] It still remains challenging to produce accurate and transferable potentials in these systems.[292] The challenge is even greater in MOFs, due to a more diverse chemical environments and organic-inorganic linkages.

IRMOF-1 flexible force fields. The first flexible MOF force field was reported in 2006 by Greathouse and Allendorf for the water-decomposition of IRMOF-1.[243] Structural collapse of the unit cell from 3.9% water content was observed and in agreement with experimental data.[293] The authors argued that bonded Zn-O interactions result in poor volume changes upon external stimuli due to bond and angle constraints. Therefore, Zn-O interactions were modeled using non-bonding pair-interactions. Bonding force field parameters of the organic linkers were taken from the generic CVFF force field with slight modifications to better represent the experimental unit cell of IRMOF-1.[294] Inorganic force field parameters were obtained from DFT calculations on zincite (ZnO). The lattice parameter $a = 25.61$ Å was found to be in good agreement with those of reported X-ray studies of a $=$ 25.67 - 25.89 Å.[295,296]

In 2008, the authors extensively validated the force field. The lattice parameters of $a = 25.74$ Å and 26.05 Å at 0 K were obtained by extrapolating finite-temperature molecular dynamics calculations and from conjugate-gradient based energy minimizations.[244] The overestimated lattice parameter from the energy-minimization was resolved by using the mode-following technique.[105] This method eliminates negative eigenvalues of the Hessian in order to obtain a true minimum on the potential energy surface and resulted in a lattice parameter of $a = 25.698$ Å in better agreement with the molecular dynamics extrapolation. The space-group was however reduced from *Fm3*$\bar{m}$ (255) to *Fm*$\bar{3}$ (202) showing distortions of the metal-linker node.[297]

Three other flexible force fields for IRMOF-1 were introduced in 2007 by Schmid *et al.*, Dubbeldam *et al.* and Han and Goddhard III. Schmid *et al.* used a building block approach for the parameterization of IRMOF-1 based on the MM3 force field.[246] DFT-B3LYP calculations on a tetranuclear zinc benzoate cluster (Zn_4O-$(O_2CC_6H_5)_6$) were used as a reference system. Selected bond distances and vibrational frequencies were compared with experimental data.[298,299] Even though bond distances were slightly overestimated, the authors argued that the reproduction of the vibrational frequencies was more important for the lattice dynamics. By transforming the Hessian matrix, a set of force constants was obtained (excluding translation and rotational motion). Unlike, the Greathouse and Allendorf force field, the Zn-O bonds were considered partially bonded. To reproduce the characteristic asymmetric stretch of Zn_4O at around $\nu \sim$ 530 cm^{-1}, the off-diagonal terms (representing coupling interactions) were considered for the bond-bend Zn-O$_{\text{cent}}$/Zn-O$_{\text{cent}}$-Zn interactions.[300] An additional $Zn_4(O_2CH)_5$-BDC-BDC$Zn_4O(O_2CH)_5$ cluster model, was chosen for the internal torsion barrier

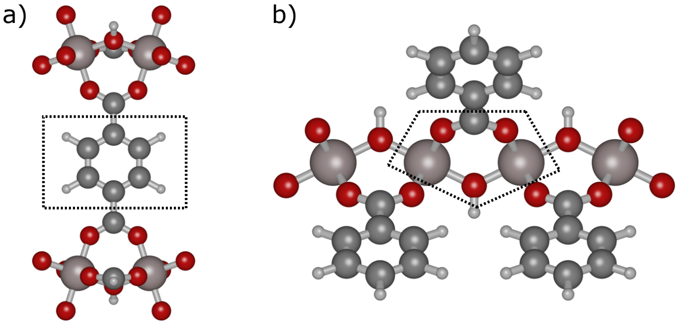

Figure 4.2: *Cluster models representing MIL-53(Al) used in QuickFF to derive force field parameters for MIL-53(Al) with (a) linker and (b) metal-oxide clusters. Terminating hydrogens are omitted. Color code: C (dark gray), O (red), H (light gray), Al (brown). Figure is a redrawn from a Figure in reference.*[301]

of BDC-linker.

Dubbeldam *et al.* reparameterized the Greathouse and Allendorf force field by reproducing the experimental lattice parameter and CO_2 and methane adsorption isotherms.[217] Here, the Zn-O interactions were also considered non-bonding. This model predicted large NTE which was later confirmed by neutron diffraction experiments and *ab initio* calculations.[302] A later refinement mapped the 0 K elastic tensor on the *ab initio* calculated tensor.[297,303]

Using the generic DREIDING[200] force field, Han and Goddard III argued that the amplitude of rotations of the Zn-O clusters and the rotations of the organic linker are increased at higher temperatures, resulting in NTE.[245] The decrease of the elastic constants upon heating is consistent with the force field of Greathouse and Allendorf[244] and with recent *ab initio* molecular dynamics.[242] The above mentioned force fields have been summarized in Table 4.1 and show good agreement with experiments and *ab initio* results.

Parameterization schemes. Table 4.2 presents the parameterizing method, charge scheme and the metal-linker interaction of various generic flexible force fields. The building block methodology is a popular approach utilizing *ab initio* calculations on non-periodic clusters to fit parameters. QuickFF is such an example.[304] Figure 4.2 shows two clusters for the parameterization of MIL-53(Al): a) for the organic linker and b) for the inorganic node. Parameterization is divided per cluster into three steps: i) determination of dihedral reference angles and multiplicities, ii) extraction of force field parameters for an internal coordinate and iii) refinement of force constants and fitting of missing dihedral force constants. Parameters of functional forms that occur in both clusters are averaged.

MOF-FF, a third generation force field of Schmid *et al.*, is also based on the building block methodology.[305] The first generation has been introduced on the preceding page.[246] In the second generation, a generic algorithm was used to derive force field potentials for the zinc benzoate and dilithium terephthalate clusters.[306]

Zn-dependent torsion Zn-O_{carb}-C_{carb}-O_{carb} were included to keep the Zn atoms in the carboxylate plain. In the third generation a new energy expression was proposed as well as a new generic parameters for Cu and Zn paddlewheel-based structures and for Zn_4O and $Zr_6(OH)_4$-based MOFs.[305]

UFF4MOF[307,308] is an extension of the original Universal Force Field (UFF)[309] that incorporates additional atom types found in the Computation-Ready Experimental (CoRE) Database.[310] The only fitted parameter is the bond (covalent) radius of the atom types which is obtained by minimizing the residual error of a training set of secondary building units from gas phase *ab initio* calculations. Only three of the nineteen minimized MOF structures using UFF had calculated lattice parameters of larger than 4% compared to the experimental values.

By extending the BTW-FF model, Gale *et al.* developed the vibrational metal-organic framework (VMOF) force field.[247,311] Here, force field parameters are explicitly fitted on DFT-PBEsol calculated phonon spectra of periodic binary oxides such as ZnO, ZrO_2, TiO_2, Al_2O_3. A modified MM3 Buckingham potential for the metal-linker interaction was needed to reproduce the *ab initio* and experimental structural and mechanical properties of the binary oxides more accurately. Inaccurate long-range dispersion interactions resulted in considerable lower bulk moduli of various MOFs compared to DFT values. The soft vibrational modes and the fingerprint regime could not be accurately reproduced due to discrepancies in the metal-oxygen stretching modes and due to the use of formal charges as was argued by the authors.[311] It must be noted that it is challenging to obtain accurate data of the low lying frequencies using experimental techniques or *ab initio* calculations.[229]

In Chapter 5, a new parameterization scheme is propsed that fits force field potentials on the elastic tensor.

Table 4.2: *Methods of parameterizing, atomic charge partition schemes and metal-linker interaction of generic parameterization schemes for flexible force fields for metal-organic frameworks.*

	Method	Charge scheme	Metal-linker interaction	Reference
QuickFF	Clusters	Point and gaussian charges[a]	Bonding [b]	304
MOF-FF	Clusters	Gaussian charges	Morse and bending[c]	305
UFF4MOF	Clusters	UFF[309]	Bonding	307,308
BTW-FF	Periodic	Effective charges[d]	Bonding and non-bonding	247
VMOF	Phonons	Charge equilibriation and formal[e]	Buckingham[f] and Coulomb	311
HBWD	Elasticity	REPEAT	Bonding, bending and torsion	312

[a] f(r_{ij}) $= 1 \rightarrow$ point charges, else erf$(\frac{r_{ij}}{d_{ij}}) \rightarrow$ Gaussian charges

[b] Bonds, bends and torsions

[c] Morse: $\frac{1}{2\alpha^2} k_b \Big[1 - \exp\left(-\alpha(r_b - r_b^{\text{ref}})\right)\Big]^2$, bend: $\frac{V_a}{2}\Big[1 + \cos\left(n\theta_a + \theta_a^0\right)\Big]$

[d] Topological analysis of Bloch states

[e] Ligands charges: equilibriation scheme of Gasteiger,[313,314] metal nodes and inorganic oxygens: formal charges.

[f] Modified MM3 Buckingham potential with A = $1.84 \cdot 10^5$, B = 12 and C = 2.25

4.4 Challenges and prospects

Finite-size effects. Finite-size effects in simulation cells can influence material and adsorption properties. For example, different linker-pair combinations in MOFs containing substituted organic linkers might explain peak broadening of XRD profiles.[315] Figure 4.3 presents four different linker-pair combinations of amino-functionalized MIL-47(V), R = -NH_2. The substitution patterns influence the electronic and mechanical stability. It was demonstrated that electronic unfavorable substitution patterns, A2B3 and A2B6, correlate with low mechanical stability.[316] Low mechanical stability relates to low values of the elastic tensor. Another example for using supercells is the case of DMOF-1 [$Zn_2(BDC)_2(DABCO)$; DABCO = 1,4-diazabicyclo[2.2.2]octane]. Figure 4.4 shows a classical optimized DMOF-1 structure using the mode-following minimization technique.[105] The lowest energy structure has two sequentially DABCO-linkers along the b-direction in the staggered configuration.[317,318] This configuration cannot be obtained using a single unit cell.

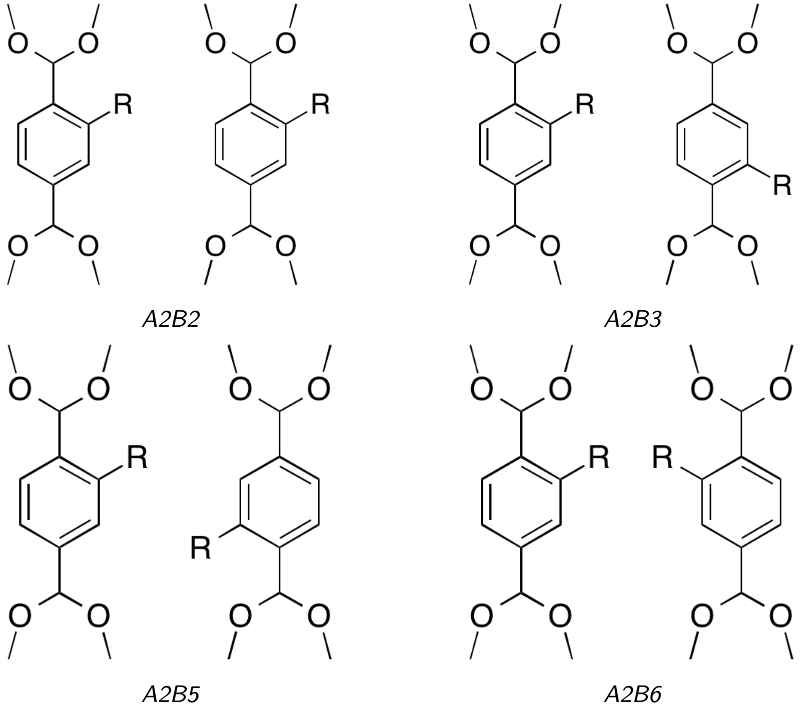

A2B2

A2B3

A2B5

A2B6

Figure 4.3: *Four proposed linker-pair combinations of substituted BDC-linkers with substituent R = -NH2. A/B refers to the left/right linker, whereas numbers indicate substituent positions. Only 2, 3, 5 and 6 are available for substitution.*

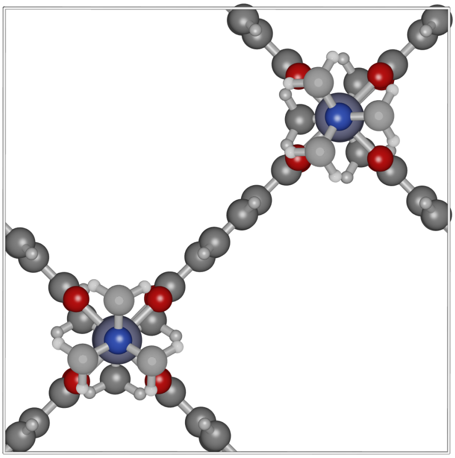

Figure 4.4: *Classically optimized DMOF-1 with $a = c =$ 15.483 Å and $b =$ 19.283 Å. The DABCO linkers are along the b-direction are in the staggered configuration. Color legend: C (dark gray), O (red), H (light gray), N (blue), Zn (dark gray).*

Sampling schemes. An important challenge for force field calculations is the development of efficient sampling schemes for large-scale structural transformations. Currently, it takes on the order of hundreds of picoseconds before a *lp* to *np* phase transition is observed in MIL-53(Al) using standard molecular dynamics.[268] This timescale is too long to sample phase space upon external stimuli. It is therefore currently not possible to study guest-induced phase transitions using osmotic Monte Carlo simulations. Demuynck *et al.* showed that umbrella sampling is an efficient method for generating free energy barriers.[319] Here, an order parameter λ is defined that describes the transition from the *lp* to the *np* phase and *vice versa*, as shown schematically in Figure 4.5.[108] The free energy barrier is however loading dependent, meaning that for each loading a separate bias potential needs to be constructed.

Continuum mechanics. The validity of finite-elasticity theory in terms of an atomistic representation is a much debated topic. Specifically, the concept of stress is ill defined at the atomic level since stress is a continuum concept (see Zimmerman *et al*. for a review on this topic).[320] Many atomistic simulation codes rely on the virial expression for the stress tensor introduced by Clausius as shown in Equation (1.26).[321]

Tsai proposed to compile the stress from momentum flux components across an area and the interatomic force components intercepted by the same area.[322] It was argued that this method and the virial approach are the same in the thermodynamic limit. Sun *et al*. proved for a one-dimensional system that the local stress from the virial formulation and from Tsai are only equivalent for homogeneous deformation within the neighborhood of an interaction-cutoff radius.[323] They ar-

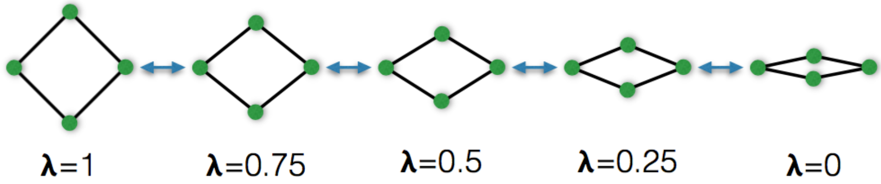

Figure 4.5: *Any movement from a large pore phase to a narrow pore phase can be described in terms of a parameter λ that ranges from 0 to 1 describing the progress of the transition. Using Umbrella sampling the free energy barrier can be biased away.*

gued that this conclusion can be extended to three dimensions. Hardy developed an expression for the Cauchy stress at a spatial point by relating density functions from continuum mechanics to masses, positions and velocities of individual particles.[324] Zimmerman *et al.* concluded that the Hardy stress converges fast to results expected from continuum mechanics at finite-temperatures or subjected to deformation.[320]

Another important continuum mechanical concept is the deformation gradient. Strains at large deformation are typically expressed in terms of the deformation gradient $\boldsymbol{F}$ which is defined as

$$\boldsymbol{F} = \frac{\partial \boldsymbol{x}}{\partial \tilde{\boldsymbol{x}}} \tag{4.4}$$

with $\tilde{\boldsymbol{x}} = \{\tilde{x}_1, \tilde{x}_2, \tilde{x}_3\}$ being a point in the reference framework and $\boldsymbol{x} = \boldsymbol{x}(\tilde{\boldsymbol{x}}) = \boldsymbol{x}(\tilde{x}_1, \tilde{x}_2, \tilde{x}_3)$ being a point in the deformed framework. Zimmerman *et al.* proposed an atomistic-scale mean-value deformation gradient relation under the restriction that any atom must have at least three neighbors which must not be coplanar nor collinear.[325] It was shown that the compatibility of the deformation gradient was indeed zero. This is equivalent that the curl of any gradient much be zero.

An interesting question which can be answered with force fields is if the elastic tensor predicts thermal expansion or *vice versa*? For axial solids, the principal coefficients of thermal expansion can be related to the elastic compliance ($\mathcal{S}_{ij} = \mathcal{C}_{ij}^{-1}$) by[326]

$$\begin{aligned} \alpha_{\perp} &= \frac{C_t}{V}\Big\{(\mathcal{S}_{11} + \mathcal{S}_{12})\gamma_{\perp} + \mathcal{S}_{13}\gamma_{\|}\Big\} \\ \alpha_{\|} &= \frac{C_t}{V}\Big\{2\mathcal{S}_{13}\gamma_{\perp} + \mathcal{S}_{33}\gamma_{\|}\Big\} \end{aligned} \tag{4.5}$$

with C_t the heat capacity under constants stress, V the unit cell volume and γ the directional Grüneisen functions. This suggests that a correct description of the elastic constants is crucial for capturing thermal expansion effects. However, the opposite cause-effect relation has also been suggested.[327]

Lastly, the increasing use and development of machine learning techniques are very promising for force field development.[328] Evolutionary approaches, such as genetic algorithms, are well suited for non-linear high-dimensional optimization issues that are involved in force field parameterization.[306] Other examples include the determination of polarizable force field parameters from *ab initio* data,[329] prediction of mechanical properties for zeolites,[330] identification of molecular characteristics that give rise to porous crystals,[331] constructing atomic forces using Bayesian interference or on-the-fly *ab initio* molecular dynamics simulations.[51,332,333]

Acknowledgments

This material is supported by The Netherlands Research Council for Chemical Sciences (NWO-CW), also through a VIDI grant (D.D.). We thank Nicholas C. Burtch for fruitful discussions and critically reading of the manuscript. We thank Ariana Torres Knoop for fruitful discussions.

CHAPTER 5

Flexible force field parameterization through fitting on the *ab initio* derived elastic tensor

Constructing functional forms and their corresponding force field parameters for the metal-linker interface of metal-organic frameworks is challenging. We propose fitting these parameters on the elastic tensor, computed from density functional theory calculations. The advantage of this top-down approach is that it becomes evident if functional forms are missing when components of the elastic tensor are off. As a proof-of-concept, a new flexible force field for MIL-47(V) is derived. Negative thermal expansion is observed and framework flexibility has a negligible effect on adsorption and transport properties for small guest molecules. This force field parametrization approach can serve as a useful tool for developing accurate flexible force field models that capture the correct mechanical behavior of the full periodic structure.

Based on: J. Heinen, N.C. Burtch, K.S. Walton and D. Dubbeldam, *Flexible Force Field Parameterization through Fitting on the Ab Initio derived Elastic Tensor*, Journal of Chemical Theory and Computation, **2017**, 13, 3722-3730

5.1 Introduction

Generating force fields for classical simulations is an art.[334] It is impossible, with a finite amount of functional forms, to perfectly reproduce the full quantum mechanical energy landscape. Therefore, the most common route is to build up the force field from chemical entities like bonds, bends and torsions, and add physical behavior in layers on top of these.

For example, Figure 5.1 shows qualitatively the computed vibrational spectrum of IRMOF-1. The high frequencies at $\nu \approx 3000$ cm^{-1} are due to C-H bond-stretching and at decreasing frequency, the bond, bend, and torsion modes appear. Even if a force field is purely harmonic in its functional form, at finite temperature the spectrum is anharmonic. The lowest vibrational frequencies, typically at $\nu <$ 500 cm^{-1} are large framework deformations which are heavily affected by long-range interactions (Van der Waals and electrostatics).[32,229]

One of the most widely used approaches to obtain parameters for flexible MOF force fields is the building block methodology as described in the previous chapter. Here, non-periodic *ab initio* calculations are performed on cluster models to extract force constants and references values.[301,304,335–337] Since long-range interactions and long-range connectivity are not present in cluster models, the obtained force field parameters do not guarantee that their independently obtained collective behavior captures the overall mechanical behavior. For example, inaccurate long-range interactions can lead to smaller bulk moduli as compared to *ab initio* calculations.[311] Parameterization on properties of periodic reference structures, such as phonons, might be more advantageous.[247,311] However, reproducing soft vibrational modes remains challenging and a large number of fitting parameters makes this procedure time-consuming. In Chapter 4 various parameterization

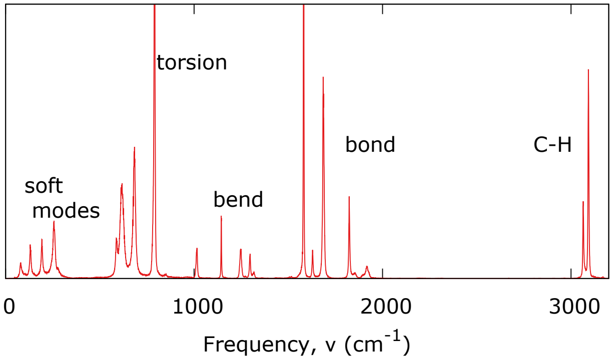

Figure 5.1: *Vibrational spectrum of IRMOF-1 at T = 298 K computed using the Fourier transform of the charge-weighted velocity auto-correlation function. Calculations are based on the Dubbeldam force field.*[297]

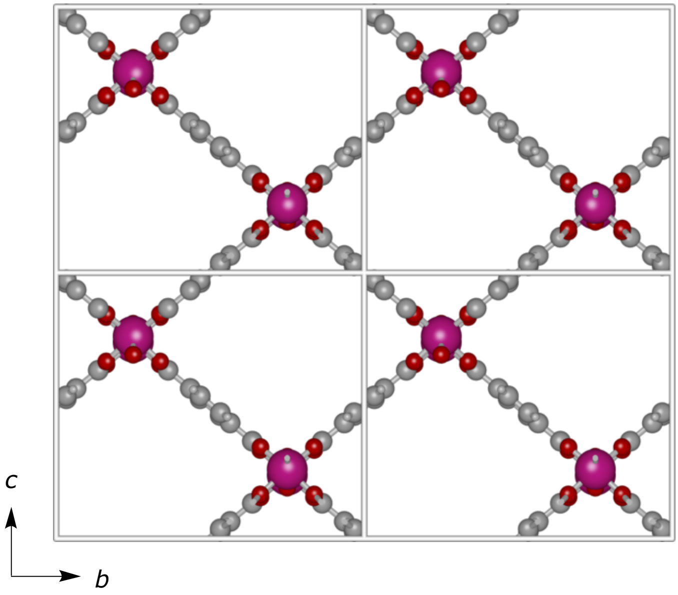

Figure 5.2: *Crystallographic unit cells (1 x 2 x 2) of MIL-47(V) viewed along the* a*-direction with* a *= 6.818 Å,* b *= 16.143 Å and* c *= 13.939 Å. Color legend: C (dark gray), O (red), H (light gray), V (pink).*

schemes have been discussed.

A new parameterization scheme is presented in this chapter that fits the flexible behavior of the hinges in MOFs on the elastic tensor. Gale *et al.* used also the elastic tensor for the optimization of core-shell zeolite models.[338] However, only a handful of parameters need to be optimized for zeolites and there is little ambiguity in the functional forms of the model. MOFs are chemically much more diverse than zeolites and the challenging part for MOFs is modeling the connection of the hinges (metal-linker interface) while making sure the model reproduces the correct mechanical behavior.

In this work, a new flexible force field for the orthorhombic MIL-47(V) is parameterized by fitting on the *ab initio* calculated elastic tensor and use this example to discuss the benefits of the methodology. MIL-47(V) consists of linear chains of corner-sharing VO_6 octahedra connected by BDC-linkers as shown in Figure 5.2.[339] The hinges in MIL-47 determine largely the mechanical behavior and modeling these correctly is *vital*. The chief advantage of fitting on the elastic tensor is that individual components of the tensor contain directional information and missing functional forms in the force fields can therefore be detected.

Reference elastic constants are computed using *ab initio* calculations and taken from previous studies. The force field parameters that describe the hinges are chosen initially with reasonable values based on previous work or chemical intuition.[340] The structure is then minimized and the elastic constants are examined. By comparing the obtained elastic constants to the *ab initio* values a new set of force field parameters is chosen. By applying this process iteratively, the final parameter set is obtained. Using our final model, it is demonstrated that the optimized model has negligible influence on the adsorption and diffusion properties of small adsorbates.

5.2 Computational methodology

5.2.1 Classical force field simulations

Initial functional forms and inorganic bonding parameters for MIL-47(V) were chosen based on chemical intuition and from previous work.[340] The organic bonding parameters were taken from the OPLS-AA force field.[285] Lennard-Jones parameters were taken from DREIDING[200] and those not found in DREIDING were taken from UFF.[309] The force field-based minimization procedure uses the mode-following technique.[104,105] This algorithm uses the analytical second-order derivative of the internal energy to obtain a true local minimum on the potential energy surface.[297] A generalized Hessian $\mathcal{H}_g$ is constructed

$$\mathcal{H}_g = \begin{pmatrix} \mathcal{H}_{ij} = \frac{\partial^2 \mathcal{U}}{\partial r_i \partial r_j} & \mathcal{H}_{i\epsilon} = \frac{\partial^2 \mathcal{U}}{\partial r_i \partial \epsilon} \\ & \\ \mathcal{H}_{\epsilon i} = \frac{\partial^2 \mathcal{U}}{\partial \epsilon \partial r_i} & \mathcal{H}_{\epsilon\epsilon} = \frac{\partial^2 \mathcal{U}}{\partial \epsilon \partial \epsilon}. \end{pmatrix} \tag{5.1}$$

with the internal energy $\mathcal{U}$, the force constant matrix $\mathcal{H}_{ij}$ (conventional Hessian) and the Born term $\mathcal{H}_{\varepsilon\varepsilon}$ being the second order derivative of the internal energy with respect to the strains. The Born term accounts for distortions of the lattice and $\mathcal{H}_{i\epsilon}$ and $\mathcal{H}_{\epsilon i}$ are cross-terms. From this generalized Hessian, the 0 K elastic constants can be calculated up to machine precision as shown in Equation (1.27).

The generalized Hessian encompasses the conventional Hessian (therefore the vibrational spectrum) as well as the gradients and second-order derivatives of the internal energy with respect to the strain. Instead of fitting a large array of vibrational frequencies, the fitting problem is reduced to fitting a smaller number of elastic constants.

The elastic constants are calculated using the energy-strain relations. Therefore the range of strains is evaluated for IRMOF-1, see Figure 5.3. To compute $\mathcal{C}_{11}$, a non-volume preserving strain ϵ is applied that transforms the reference simulation cell $\boldsymbol{h_o}$ according to

$$\boldsymbol{h} = \begin{pmatrix} 1+\epsilon & 0 & 0 \\ 0 & 1 & 0 \\ 0 & 0 & 1 \end{pmatrix} \boldsymbol{h_0} \tag{5.2}$$

where ϵ is a small distortion. Figure 5.3a illustrates that non-quadratic behavior occurs at strains smaller than -0.004. For the volume preserving strains, distortion

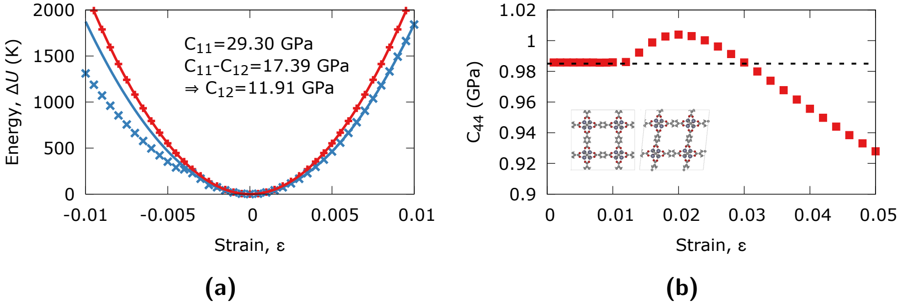

Figure 5.3: *Computing the elastic constants of IRMOF-1 from energy-strain curves. (a) Symmetric strain $\mathcal{C}_{11} - \mathcal{C}_{12}$ (in red) and asymmetric strain $\mathcal{C}_{11}$ (in blue). (b) $\mathcal{C}_{44}$ values as a function of polynomial fit-range (the converged value is obtained for strains smaller than 1% here; the dotted line denotes the value obtained from Equation (1.23)). Inset shows the structure before and after applying the $\mathcal{C}_{44}$ strain. Adapted from Ref.*[312]

can be used up to 0.01 as shown for $\mathcal{C}_{44}$ in Figure 5.3b. The small energy differences for $\mathcal{C}_{44}$ illustrate the difficulties in computing accurate energies using DFT. Often a trade-off must be made. On the one hand, a small step in the numerical differentiation needs to be made such that the domain where the functional description is valid. On the other hand, for shallow energy landscapes, a larger step is necessary to have sufficiently high energy differences that would otherwise be lost in the numerical noise.

Table 5.1 reports the 0 K elastic constants computed using the mode-following technique for selected zeolites and IRMOFs. For the monoclinic MFI structure, there are 13 independent components, but for cubic structures, such as IRMOF-1, there are only 3.[37] The elastic constants for zeolites can be up to an order of magnitude larger than for MOFs. This reflects the reduced mechanical stability. Also, the elastic constants decrease with increasing linker-length (IRMOF-1 $<$ IRMOF-10 $<$ IRMOF-16). For IRMOF-1, the elastic constants are split into two contributions: (1) the Born term, and (2) the relaxation term. As can be seen from Table 5.1, the relaxation terms for IRMOF-1 are substantial. For $\mathcal{C}_{44}$, the relaxation term is almost as large as the Born term, which explains the very small $\mathcal{C}_{44}$, $\mathcal{C}_{55}$, and $\mathcal{C}_{66}$ shear values. The large relaxation contribution to the elastic constants illustrates the need for robust optimization algorithms that prevent the system of becoming stuck in a saddle point during relaxation.

5.2.2 Density functional theory calculations

DFT calculations were performed to optimize the atomic geometry and cell parameters and to compute the elastic tensor using the projector augmented wave (PAW) method as implemented in the VASP code.[75–77,341] The valence electrons for the elements O and C include the 2s and the 2p electrons and for V they include the 4s and 3d electrons. The dispersion corrected PBE exchange-correlation functional with an energy cut-off of 600 eV was used.[167,342] K-point sampling was set to 6 x 2 x 2 using the Monkhorst-Pack scheme and a Gaussian smearing of 0.05 eV was applied.[70]

5.3 Results and discussion

MOFs have shallow energy-landscapes around the hinges and calculating mechanical properties using plane wave DFT-code can be challenging.[343] The parameters of the finite difference method, step size δ and number of displacements N, to compute the gradient of the forces is assessed.[341] As reported in Table 5.2, for $\delta = 0.02$ Å, negative eigenvalues of the elastic tensor are obtained. This violates the Born stability criteria[235,236] suggesting that the unit cell is mechanically unstable.[344] An imaginary frequency, observed for $\delta = 0.005$ Å, indicates a saddle-point on the potential energy surface. Generally, it appears that smaller step sizes give larger elastic constants. These results suggest that the numerical differentiation parameters affect whether a unit cell is considered to be stable. The lattice parameters and elastic constants from this work and from literature are presented in Table 5.3.[34,343] The reference elastic constants are the average of the three *ab initio* calculated elastic constants computed with $\delta = 0.015$ Å represented by the first three columns in Table 5.3.

Table 5.1: *Elastic constants $\mathcal{C}_{ij}$ (GPa) in Voigt notation calculated for zeolites MFI and α-quartz and IRMOF-series. The Born and relaxation contribution of the elastic constants of IRMOF-1 are given in the last two rows.*

	$\mathcal{C}_{11}$	$\mathcal{C}_{22}$	$\mathcal{C}_{33}$	$\mathcal{C}_{44}$	$\mathcal{C}_{55}$	$\mathcal{C}_{66}$	$\mathcal{C}_{12}$	$\mathcal{C}_{13}$	$\mathcal{C}_{14}$	$\mathcal{C}_{23}$	$\mathcal{C}_{24}$	$\mathcal{C}_{34}$	$\mathcal{C}_{56}$
MFI	97.71	88.99	79.36	28.65	26.27	23.09	12.09	26.49	-2.15	25.44	-7.93	-5.78	-0.78
α-quartz	94.55	94.55	116.04	49.97	49.97	38.06	18.43	19.67	-14.48	19.67	14.48	-	-14.48
IRMOF-16	12.11	12.11	12.11	0.1	0.1	0.1	3.38	3.38	-	3.38	-	-	-
IRMOF-10	15.97	15.97	15.97	0.15	0.15	0.15	3.93	3.93	-	3.93	-	-	-
IRMOF-1	29.3	29.3	29.3	0.985	0.985	0.985	11.91	11.91	-	11.91	-	-	-
- Born	71.87	71.87	71.87	27.81	27.81	27.81	20.91	20.91	-	20.91	-	-	-
- Relax	42.57	42.57	42.57	26.83	26.83	26.83	9	9	-	9	-	-	-

Table 5.2: *Elastic constants $\mathcal{C}_{ij}$ (GPa) in Voigt notation for MIL-47(V) with various step sizes δ (Å) and displacements N. The smallest and largest eigenvalues are denoted λ_1 and λ_6, respectively with negative eigenvalues denoted in red.*

N	δ	$\mathcal{C}_{11}$	$\mathcal{C}_{22}$	$\mathcal{C}_{33}$	$\mathcal{C}_{44}$	$\mathcal{C}_{55}$	$\mathcal{C}_{66}$	$\mathcal{C}_{12}$	$\mathcal{C}_{13}$	$\mathcal{C}_{23}$	λ_1	λ_6
2	0.005	45.11	85.16	34.58	46.26	7.24	10.80	24.14	16.00	49.11	4.59	125.52
	0.015	40.93	83.45	29.41	43.84	9.43	11.04	19.95	12.00	48.19	1.18	118.65
	0.020	39.90	80.61	27.33	43.45	7.05	7.22	19.00	10.49	47.04	-0.09	114.36
4	0.005	41.80	83.49	32.90	46.48	0.98	10.76	22.47	14.44	47.58	0.98	121.07
	0.015	38.13	82.86	29.70	43.72	9.89	11.42	18.74	11.43	48.10	1.32	117.32
	0.020	37.54	79.43	26.30	43.91	6.80	4.39	17.72	9.07	46.03	-0.31	111.36

After manually exploring the initial force field parameter space it becomes clear that no trial-set with the existing functional forms is able to come close to reproducing all components of the reference elastic tensor. However, by inspecting which components of the tensor are off, missing functional forms can be elucidated. The elastic constants contain directional information and bond-stretching interactions can only affect the elastic constants that are in the direction of the bond. Bends and torsions influence the perpendicular response of stress-stimuli. Therefore, not only the parameters are optimized, but also a force field with better functional forms can be obtained. This is an advantage over existing parameterization methods. An additional torsion potential (O2-V1-O1-V1) was added which was essential to reproduce the reference $\mathcal{C}_{22}$ value. The dominant changes by varying the force field parameters of this torsion were found in $\mathcal{C}_{22}$, thereby tuning this component of the elastic tensor independently.

The elastic constants of a previous flexible force field for MIL-47(V) was assessed by including a harmonic C-H vibration. Poor agreement of the elastic constants and lattice parameters was found as presented in the fourth column of Table 5.3.[340] The distribution profile of the organic linkers torsion angles using the force field from this work is significantly more narrow, which is attributed to a 3.7 larger force constant for the O2-C3-C2-C1 torsion in this work. Setting this force constant to 600 K, as done in the previous force field, results in a mechanically unstable unit cell.[344]

Table 5.3: *Elastic constants $\mathcal{C}_{ij}$ (GPa) in Voigt notation for MIL-47(V). Unit cell lengths in (Å) and angles in (°) and volume V in (Å^3). Experimental:*[339] a = *6.8179 Å*, b = *16.143 Å*, c = *13.939 Å*, β = *90.00 °*, V = *1534.15 Å^3. * This work (FF=force field).*

	Vanpoucke[343]	Ortiz[34]	PBE-D3*	FF[340]	FF*
$\mathcal{C}_{11}$	35.4	40.68	39.53	12.50	42.55
$\mathcal{C}_{22}$	67.6	62.60	83.16	37.90	70.54
$\mathcal{C}_{33}$	34.0	36.15	29.56	17.26	39.43
$\mathcal{C}_{44}$	44.2	50.83	43.78	52.73	45.02
$\mathcal{C}_{55}$	6.7	7.76	9.66	2.07	9.12
$\mathcal{C}_{66}$	8.7	9.30	11.23	13.67	10.06
$\mathcal{C}_{12}$	15.2	12.58	19.35	-12.22	9.10
$\mathcal{C}_{13}$	10.2	9.28	11.72	-8.77	6.80
$\mathcal{C}_{23}$	46.0	46.98	48.15	24.62	51.44
a	6.842	6.79	6.807	6.754	6.901
b	16.394	16.05	16.696	16.561	16.125
c	13.854	13.98	13.190	13.735	14.131
β	90.00	90.00	90.00	89.924	90.00
V	1554.1	1523.5	1499.1	1536.2	1572.6

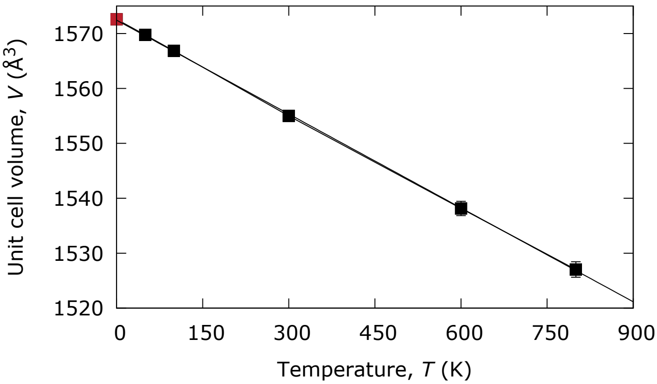

Figure 5.4: *Unit cell volume as function of temperature of MIL-47(V) from molecular dynamics simulation showing negative thermal expansion (α_V = -36.2·10^{-6} K^{-1} over a temperature range of 0 K to 800 K). Error-bars are smaller than symbol size. The volume at 0 K (in red) is obtained from the mode-following technique.*

Using the newly parameterized flexible force field, negative thermal expansion was predicted from molecular dynamics simulations in the NpT-Parrinello Rahman ensemble.[95,96] A volumetric coefficient of thermal expansion $\alpha_V =$ -36.2·10^{-6} K^{-1} over a temperature range of 0 K to 800 K was obtained as shown in Figure 5.4 and in agreement with other work.[345]

There is a ongoing debate on the influence of framework flexibility on adsorption and diffusion properties.[277,346–350] Adsorption and diffusion properties are computed of CH_4, CO_2 and n-C_6 using the newly derived flexible and a rigid force field. The force field parameters of the adsorbates were taken from the TraPPE force field.[283,351] Simulations were conducted in the osmotic $(\mu_1 N_2 pT)$[113] and grand-canonical (μVT)[107] ensembles, respectively. Figure 5.5 shows the adsorption isotherms and no significant differences between the flexible and rigid material are observed.

Secondly, self-diffusivities were computed using molecular dynamics simulations at various loadings. The self-diffusion coefficient $\mathcal{D}_s$ is obtained from the Einstein relation[108]

$$\mathcal{D}_s = \lim_{t\to\infty} \frac{1}{6t} \left\langle \sum_{i=1}^{N} \left(r_i(t) - r_i(0)^2 \right) \right\rangle \tag{5.3}$$

with t being the time, N the number of particles and r_i the center-of-mass. Figure 5.6 shows the self-diffusivities as function of loading at T = 300 and 600 K. The error-bars overlap considerably, indicating that no significant difference are found. This suggests that framework flexibility of MIL-47(V) has negligible influence on diffusion properties of small guest molecules.

Framework flexibility has negligible influence of the adsorption and transport

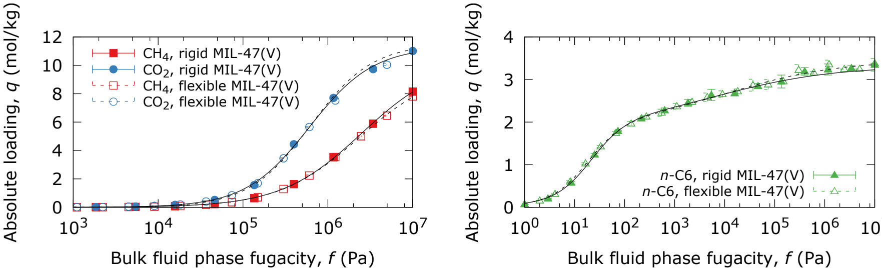

Figure 5.5: *Single component adsorption isotherms of* CO_2, CH_4 *and* n-C_6 *in MIL-47(V) at* T = *303 K using flexible (open symbols) and rigid (closed symbols) force fields. Solid and dashed lines are fitted Langmuir-Freundlich isotherms for rigid and flexible force fields, respectively.*

properties of small guest whose size is considerable smaller than the channel size of MIL-47(V). Expected is that framework flexibility has considerable impact *only* when i) adsorbates are confined[278,352] or ii) phase transitions of the framework occur.[353]

Another advantage of this approach is that the construction of flexible force fields for *functionalized* MOFs is straightforward. If the parent material reproduces the elastic constants well, than one can use functional forms and parameters from generic organic force fields to include the flexible modes of the substituted organic linkers.

5.4 Conclusion

In this work, functional forms of bonding, bending and torsion parameters of the hinges in MOFs are fitted on the *ab initio* calculated elastic constants. The step size of the numerical differentiation of the gradient of the force should be carefully

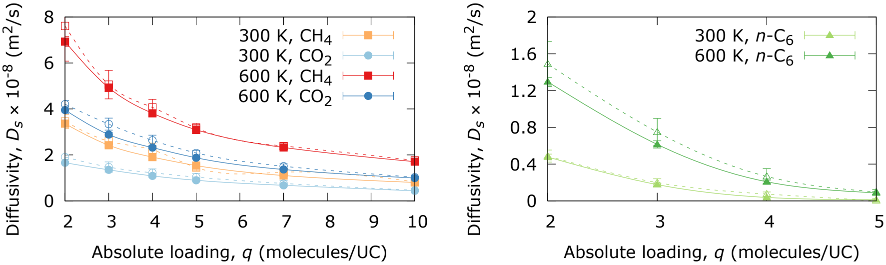

Figure 5.6: *Self-diffusivity of* CO_2, CH_4 *and* n-C_6 *in MIL-47(V) as function of absolute loading at* T = *300 K and 600 K using flexible (open symbols) and rigid (closed symbols) force fields, respectively. Lines are guidance to the eye.*

chosen. Within this parameterization approach, missing functional forms of the force field can be detected based on when components of the elastic tensor are off.

As a proof of concept, it was shown for MIL-47(V) that framework flexibility has negligible influence on the adsorption and diffusion properties for small guest molecules. Negative thermal expansion was also predicted. This procedure should, in principle, also be suitable for a broader range of crystalline materials exhibiting flexibility.

Acknowledgments

This material is supported by The Netherlands Research Council for Chemical Sciences (NWO-CW), also through a VIDI grant (D.D.), and through the Sandia National Laboratories Truman Fellowship Program, which is funded by the Laboratory Directed Research and Development (LDRD) Program (N.C.B.). We thank Stichting Nationale Computerfaciliteiten (National Computing Facilities Foundation, NCF) for the use of supercomputing facilities. We thank Ali Poursaeidesfahani and Thijs Vlugt for fruitful discussions.

CHAPTER 6

Elucidating the variable-temperature mechanical properties of a negative thermal expansion metal-organic framework

We report the first experimental study into the thermomechanical and viscoelastic properties of a MOF-material. Nanoindentations show a decrease in the Young's modulus, consistent with classical molecular dynamics simulations, and hardness of HKUST-1 with increasing temperature over the 25 - 100 °C range. Variable-temperature dynamic mechanical analysis reveals significant creep behavior, with a reduction of 56% and 88% of the hardness over 10 minutes at 25 °C and 100 °C, respectively. This result suggests that, despite the increased density that results from increasing temperature in the negative thermal expansion MOF, the thermally-induced softening due to vibrational and entropic contributions play a more dominant role in dictating the materials temperature-dependent mechanical behavior.

Based on: J. Heinen, A.D. Ready, T.D. Bennett, D. Dubbeldam, R.W. Friddle and N.C. Burtch, *Elucidating the Temperature-dependent Mechanical Properties of the Negative Thermal Expansion Metal-Organic Framework HKUST-1*, *ACS Applied Materials & Interfaces*, **2018**, 10, 21079-21083

6.1 Introduction

One of the key challenges in optimizing MOFs for various applications is the understanding of their mechanical properties.[40,42,43] Recently, tensorial analysis of MOF elastic constants using density functional theory (DFT) calculations has shed new light on mechanical properties which may be connected to large scale flexible modes such as negative thermal expansion (NTE),[32] gate-opening,[229] and negative linear compressibility.[34]

From an experimental viewpoint, hydrostatic compression in diamond anvil cells have be used to determine bulk moduli and pressure-induced amorphization behavior.[354] Another commonly used technique for mechanical characterization are nanoindentations, which have been primarily used to measure the Young's modulus and hardness of MOF single crystals and thin films.[36,40,41,241,355] The Young's modulus is a measure of a materials reversible response to strain in the Hookean limit and hardness is related to the irreversible plastic deformation of a material upon strain. A recent study by Sun *et al.* demonstrated that bimodal amplitude modulated-frequency modulated atomic force microscopy can be used to measure the Young's moduli of microcrystalline MOF nanoparticles.[356] Zeng and Tan showed that the use of high unloading strain rates using atomic force microscopy (AFM) nanoindentations can yield accurate Young's moduli for micron-sized crystals as well.[357]

Most nanoindentation studies rely on the Oliver-Pharr analysis of the load-displacement curves by assuming that the deformation is within the Hookean limit of the material.[358] These experiments neglect the time-dependent deformation of the material, known as creep. From an application's perspective, it is important that creep effects due to viscoelasticity as well as temperature effects be better understood. The thermomechanical properties of MOFs have only been studied computationally. For example, classical and first-principle simulations on IRMOF-1 showed a decrease in the elastic constants with increasing temperature.[242,244,245] This behavior was also reported for other materials that exhibit negative thermal expansion (NTE), such as ZrW_2O_8.[359,360] This observation is consistent with the understanding that materials tend to become more elastic and exhibit a reduction in their elastic constants with increasing temperature.[361–364]

Here, the viscoelastic and thermomechanical properties of the NTE MOF HKUST-1[122] are studied using variable-temperature dynamic mechanical analysis (DMA)[365] and nanoindentations combined with differential scanning calorimetry-thermogravimetric analysis and classical molecular dynamics simulations. HKUST-1 consists of dicopper paddlewheels interconnected by BTC (BTC = benzene-1,3,5-tricarboxylate) linkers, as shown in Figure 6.1. HKUST-1 has a linear coefficient of thermal expansion $\alpha_l \approx -4.5\cdot10^{-6}$ K^{-1},[30,31] and is a prototypical structure that has also been studied for its utility in humidity sensing devices, including in microcantilever sensors where the material's Young's modulus has a direct bearing on the sensor's sensitivity.[366] Further, the hardness can be related to the scratch resistance of a material, which has important implications for determining suitable handling and processing conditions for its use in electronic devices.[21] In this work, temperatures up to 100 °C are considered because of the reported irreversible changes to HKUST-1 lattice parameters above $\sim$ 127 °C.[30] Qualitative agreement between the variable-temperature behavior of the elastic moduli from the experimental nanoindentation and DMA experiments is obtained and is also supported by complimentary classical molecular dynamics simulations.

6.2 Nanoindentations

Nanoindentations remain on the most commonly used experimental methods to determine the Young's modulus and hardness of a material.[367] Here, materials are indented with a tip that has a well-defined geometry, typically a Berkovich tip (an upside-down triangular pyramid).

During the indentation process, load-displacement (P-h) data is collected from which the Young's modulus and hardness are obtained. A load-displacement curve obtained from nanoindentation experiments is shown in Figure 6.2. Here, P_{max} is the peak load that is applied during the loading segment causing a maximum displacement h_{max} of the tip into the specimen. Note, that some instruments are displacement-controlled and adjust the peak load. During the loading segment, the hardness H can be determined via

$$H = \frac{P_{\text{max}}}{A_c} \tag{6.1}$$

with A_c is the contact area that depends on the displacement h_c of the tip. For an ideal Berkovich tip, the contact area is given by the area function $A_c = 24.56 h_c^2$.

From analysis of the unloading curve, the Young's modulus can be obtained. Oliver and Pharr fitted the unloading curves to a power law of the form[358]

$$P(h) = \alpha(h - h_f)^m \tag{6.2}$$

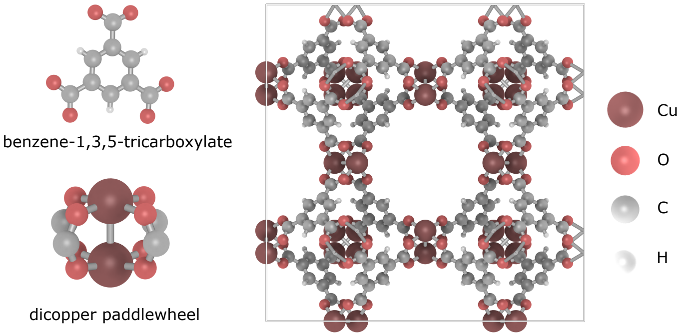

Figure 6.1: *Building units of HKUST-1 and ball-and-stick model of the unit cell along the <100> direction with a = 26.304 Å.*

with α and m being fitting parameters depending on the geometry of the tip and h_f is the final penetration depth. From this relation, the indentation modulus I can be obtained. Oliver and Pharr proposed the following relation[358]

$$I = \frac{\sqrt{\pi}}{2} \frac{1}{\beta_g} \frac{S}{\sqrt{A_c}} \tag{6.3}$$

with the elastic unloading stiffness $S = \mathrm{d}P/\mathrm{d}h$ being the slope of the unloading segment during the initial stage of unloading (dotted line in Figure 6.2) and β_g being a geometrical constant (for a Berkovich tip $\beta_g = 1.034$). The indentation modulus considers displacement in both the specimen as well as the indenter. The Young's modulus reflects the elastic recovery of the material under the indenter tip. From the indentation modulus, the Young's modulus E of the specimen can be obtained via

$$\frac{1}{I} = \frac{1-\nu^2}{E} + \frac{1-\nu_i^2}{E_i} \tag{6.4}$$

with ν being the Poisson's ratio of the specimen, E_i and ν_i being the Young's modulus and Poisson's ratio of the tip. For a diamond Berkovich tip, these values are $E_i = 1141$ GPa and $\nu_i = 0.07$. For soft materials such as MOFs, the final Young's modulus E depends significantly on the chosen Poisson's ratio ν.[39] From the *ab initio* calculated elastic tensor for HKUST-1, a Poisson's ratio of $\nu = 0.433$ was found.[32]

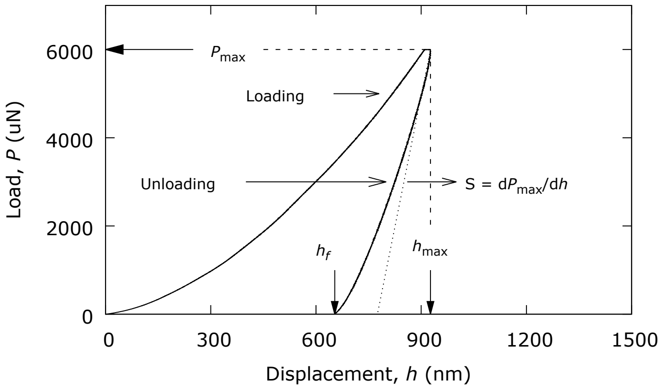

Figure 6.2: *Load-displacement curve obtained from indentation on a HKUST-1 single crystal at room temperature. The elastic unloading stiffness S is proportional to the indentation modulus.*

6.3 Dynamic mechanical analysis

The time-dependency of plastic deformation, known as *creep* can be studied using dynamic mechanical analysis (DMA).[365] DMA uses an oscillating force (stress) to probe the material and records to the material's response (strain) over a period of time as shown schematically in Figure 6.3. This technique has been widely used to the study thermal transitions in glasses and polymers.

The applied oscillating stress σ at a constant load is given by

$$\sigma(t) = \sigma_0 \sin \omega t \tag{6.5}$$

with σ_0 the load amplitude and ω the frequency. The materials response is

$$\epsilon(t) = \epsilon_0 \sin(\omega t + \delta) \tag{6.6}$$

and lags by the phase change δ. From DMA, one obtains the storage E' and loss E'' moduli which are related to the elastic recovery (stored energy of the elastic region) and energy loss due to heat dissipation, respectively. For a purely elastic solid $\delta = 0°$ and for a purely viscous response $\delta = 90°$. The ratio of the storage and loss modulus is the phase angle δ

$$\tan(\delta) = \frac{E'}{E''} \tag{6.7}$$

which is an indicator of a sample's viscoelastic behavior.

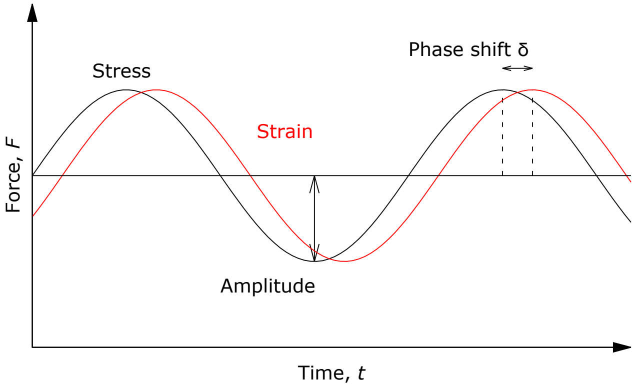

Figure 6.3: *An oscillating force is applied to a small area of the crystal (stress) and the response of the material (strain) is measured. The phase shift δ is the ratio between the elastic and viscoelastic regime of the material.*

6.4 Experimental methodology

Single crystal synthesis

Single crystals of HKUST-1 were synthesized solvothermally according to literature procedures.[368] Here, 0.49 g of copper nitrate trihydrate ($Cu(NO_3)_2{\cdot}3H_2O$) was dissolved in 3 mL of deionized water and 0.24 g of benzene-1,3,5-tricarboxylic acid (BTC) was dissolved in 3 mL of ethanol. Subsequently, 3 mL of DMF and 12 mL of glacial acetic acid (modulator) were added. The mixture was sonicated for t = 2 min at $T = 55$ °C. Thereafter, the vials were placed in a sand bath and placed in a Fisher Scientific 825F Isotemp oven for $t = 3$ days at $T = 55$ °C. The crystals were washed 3 times with ethanol and then left immersed in ethanol until their subsequent characterization.

Material characterization

Ground single crystals (SC) powder diffraction patterns were recorded using a PAN Analyical powder X-ray diffractometer with Cu-K_α ($\lambda = 1.5418$ Å) radiation at room temperature with a step size of 0.04° in 2θ. Commercial HKUST-1 from Sigma-Aldrich was recorded as reference as well as a simulated pattern (CCDC: 112954).

Nitrogen adsorption isotherms were collected at 77 K for the activated HKUST-1 SC sample using a Micrometrics ASAP 2020 surface area and porosity analyzer. The crystals were activated at room temperature by drawing ultra-high vacuum for 12 hr. Pressure points over a range of $p/p_0 < 0.05$ were used for the BET theory.[369] A BET surface area $S_{\text{BET}} = 1509$ m^2/g was obtained from the N_2 adsorption isotherm.

Nanoindentation and dynamic mechanical analysis

All mechanical properties were measured using a Hysitron TI 950 nanoindenter (load-controlled) utilizing a xSol 600 temperature control stage with a diamond Berkovich tip. Single crystals were glued on glass slides using Mikrostik polyvinyl chloride adhesive (Ted Pella, Inc.) and the crystals were activated *in-situ* under nitrogen flow (1.5 mL/min) at 100 °C for 1 hr, using a ramp rate of 10 °C/min from room temperature, until the blue to purple color change indicative of solvent removal was observed. Figure 6.4 shows time-dependent optical images obtained during activation of a separate crystal.[175,370] Differential scanning calorimetry (Mettler Toledo TGA/DSC 3+) and combined differential scanning calorimetry-thermogravimetric analysis (Mettler Toledo DSC 822e) were performed using a ramp rate of 3 °C/min under argon. Samples were *in-situ* activated for 6 and 8 hours at $T = 100$ °C, respectively. Both instruments showed no thermal transition over the 25 - 100 °C temperature range.

The Young's modulus E and hardness H values were obtained from repeated measurements of load-displacement curves, following the Oliver-Pharr method.[358]

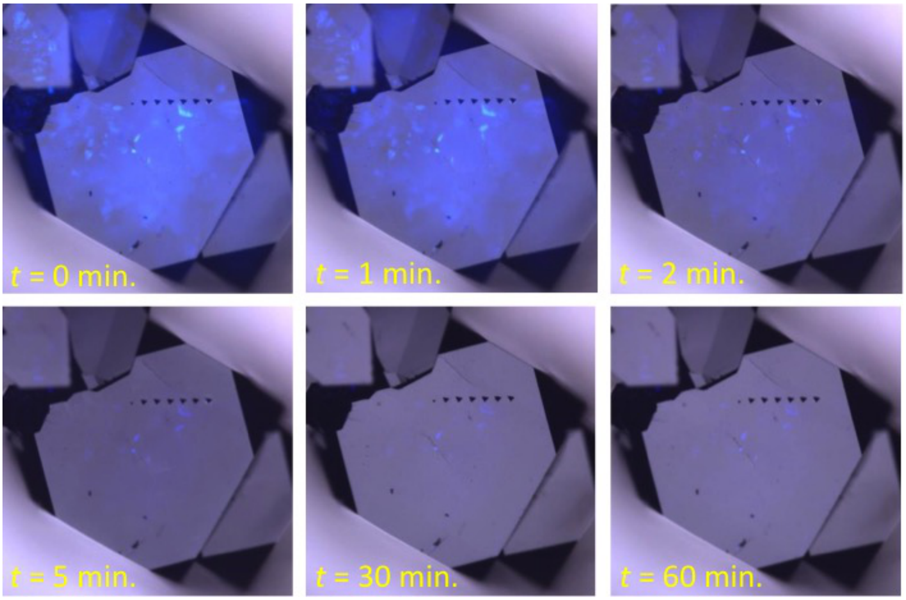

Figure 6.4: *Optical microscopy images of a HKUST-1 crystal facet followed over time during in-situ activation under a nitrogen flow.*

A maximum peak load of 8000 μN was specified with an *inter*-indent spacing of 40 μm. DMA measurements were performed by measuring the storage modulus E' and hardness values with a constant load of $P =$ 3000 μN, an amplitude of 50 μN, a frequency of 220 Hz and a *inter*-indent spacing of 25 μm. For nine different temperatures, five creep tests per temperature were performed on the crystal. The available surface area on an individual crystal's facet required that measurements with each of the different techniques be performed on different single crystals, in order to minimize effects due to adjacent residual indents. Variable-temperature measurements that were reported for a given technique, however, were all performed on the same crystal facet.

6.5 Computational methodology

Classical molecular dynamics simulations were performed based on the Zhao *et al.* force field[275] and implemented into RASPA-2.0.[116] The minimized structure yielded a lattice parameter $a =$ 26.361 Å in good agreement with experiments $a =$ 26.304 Å.[122] The 0 K elastic constants obtained from the energy-strain relation, see Equation (1.23), are shown in Figure 6.5a. The force field values tend to overestimate the DFT-calculated elastic constants (caption Figure 6.5b). It must be noted that the Zhao force field is not parameterized on the materials

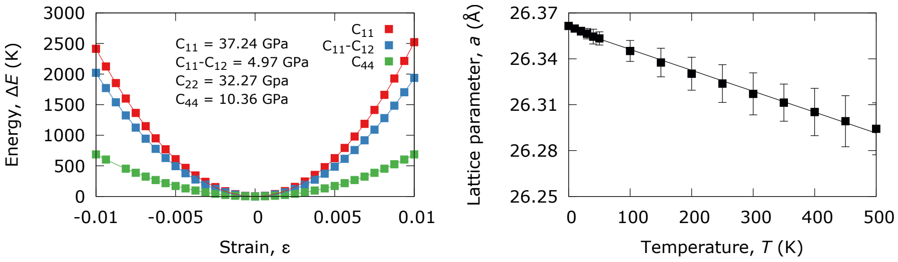

(a) **(b)**

Figure 6.5: *(a) Elastic constants at 0 K from energy-strain curves. DFT B3LYP-D3 (PW91) values are* $\mathcal{C}_{11} = 27.54(31.8)$, $\mathcal{C}_{12} = 25.78(21.2)$ *and* $\mathcal{C}_{44} = 5.27(12.7)$ *GPa.*[32,371] *(b) Lattice parameter* a *as a function of temperature* T *showing negative thermal expansion with* α_L = *-4.5·10*$^{-6}$ *K*$^{-1}$.

mechanical properties, partially contributing to the discrepancies with the DFT values. However, the purpose of this study is to assess trends in elastic constants due to temperature-effects.

Temperature-dependent lattice parameters were obtained by averaging over five separate molecular dynamics simulations using the Parrinello Rahman (PR) barostat[96] with a chained ($n = 5$) Nose-Hoover thermostat.[372,373] Each $NpTPR$ simulation was initialized for 200 ps and sampling was 1 ns with a timestep of 0.5 fs. The obtained linear coefficient of thermal expansion (CTE) over the temperature interval $T =$ 100 - 500 K is $\alpha_L =$ -4.7·10^{-6} K^{-1} (see Figure 6.5b) which is in good agreement with the experimental CTE of $\alpha_L =$ -4.5·10^{-6} K^{-1}.[30] Using the stress-fluctuation formula,[97,374] shown in Equation (1.24), finite-temperature isothermal elastic constants were calculated from canonical molecular dynamics simulations. Five NVT-simulations were conducted per temperature with different starting configurations using the lattice parameter obtained from the $NpTPR$ calculations. Each NVT-simulation has an initialization time of 400 ps and a sampling time of 8 ns with a time-step of 1 fs. Each component of the elastic tensor are averaged over their symmetric equivalent values (*e.g.* $\mathcal{C}_{11} = (\mathcal{C}_{11} + \mathcal{C}_{22} + \mathcal{C}_{33})/3$). Importantly. these finite-temperature values converge at low temperatures towards the 0 K values from the mode-following technique.

6.6 Results and discussion

To convert the indentation modulus to the Young's modulus, the Poisson's ratio proposed by Bundschuh *et al.* of $\nu = 0.433$ was used.[355] Under this assumption, the indentation modulus of 7.88 ± 1.15 GPa at room temperature produces a Young's modulus of E = 6.45 ± 0.94 GPa (averaged over indents from 4000 to 8000 μN). This value is lower than those obtained for HKUST-1 thin films (9.3

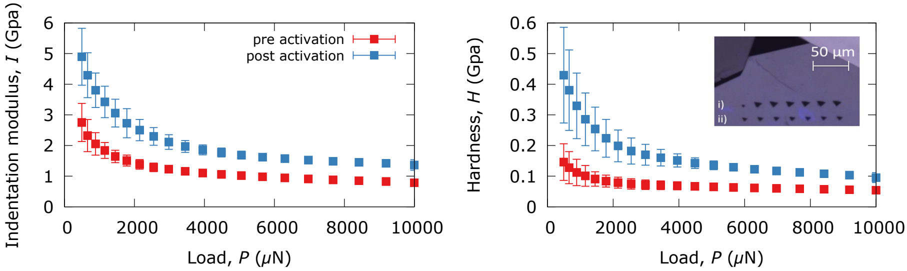

(a) **(b)**

Figure 6.6: *(a) Indentation modulus and (b) hardness for a non-activated and activated crystal facet. Inset is optical images of crystal facet. Error-bars are standard deviations of six indents.*

GPa) and monoliths (9.3 ± 0.3 GPa).[18,355] The choice of the Poisson's ratio of the sample can significantly influence the Young's modulus for MOF materials, however.[39] For example, a value of $\nu = 0.02$ gives E = 7.09 ± 0.85 GPa, which is in reasonable agreement with the theoretical value of E = 8.1 GPa.[32]

After *in-situ* activation, the material becomes harder and less elastic, as can been seen from Figure 6.6a and 6.6b. It is known that upon solvent evacuation, the HKUST-1 unit cell shrinks and the framework thus becomes more dense.[175] A more dense material would be consistent with an increased degree of resistance from the framework surface towards deformation by the indenter tip. Figure 6.7a and 6.7b show optical images of the pre and post-activated crystal-facet. Upon increasing temperature an NTE material also undergoes a contraction and representative AFM images show smaller residual indents at higher temperatures (Figure 6.7c) suggesting that the material becomes harder. However, the variable-temperature Young's modulus and hardness as function of applied load, shown in Figure 6.8a and 6.8b, obtained from nanoindentations show the opposite behavior. We find that the Young's modulus decreases to 6.28 ± 0.72, 3.99 ± 0.70 and 1.16 ± 0.34 GPa at T = 50, 75 and 100 °C, respectively. Variable-temperature elastic constants from molecular dynamics simulations (Figure 6.8c) confirm softening of the material with increasing temperature. While the effect of temperature on the simulated and experimental moduli values are qualitatively consistent, the quantitative differences between these results can be explained by the employed force field not being parameterized on the materials mechanical properties and that the simulated (bulk) values are calculated in the limit of zero strain whereas moduli obtained from indentation experiments are at finite strains. Most solids exhibit a zero slope in their elastic properties at cryogenic temperatures, such as MgO and copper.[364,375] However, interestingly, HKUST-1 exhibits a decay of its calculated isothermal elastic constants at these temperatures.

A similar correlation is also observed for the hardness (Figure 6.8b), where the maximum displacement at constant load increases with increasing temperature,

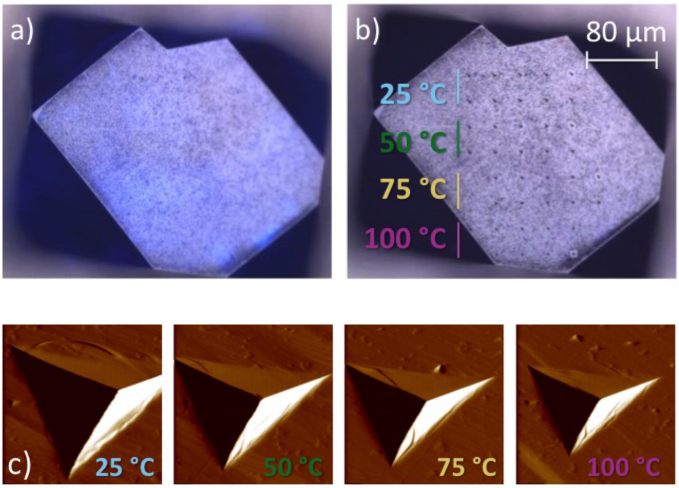

Figure 6.7: *(a) Pre-activated and (b) in-situ activated HKUST-1 crystal facet with residual indents. (c) AFM images of representative residual indents (scan size: 10 x 10* μm*).*

as can be seen from representative load-displacement curves in Figure 6.8d. The residual indents, however, as observed from the AFM images, become smaller at higher temperatures. This seemingly contradicts the decrease in the hardness that is observed, but can be better understood through the Young's modulus and viscoelastic analysis that is investigated through the DMA experiments in the following section.

Variable-temperature creep tests using DMA experiments were performed on a separate single crystal. Figure 6.9a, 6.9b and 6.9c show the time-evolution of the contact depth, hardness and storage modulus, respectively, for nine creep measurements, with each measurement representing a different temperature in the interval of 25 - 100 °C. The residual indents from these measurements are shown in Figure 6.9d. We find that the amount of creep, captured by the increase in contact depth over time, becomes increasingly larger at higher temperatures. This time-dependent creep has a considerable impact on the mechanical properties, with the hardness (Figure 6.9b) decaying from $\sim$ 0.64 to 0.28 GPa and from $\sim$ 0.40 to 0.05 GPa after only ten minutes at 25 and 100 °C, respectively.

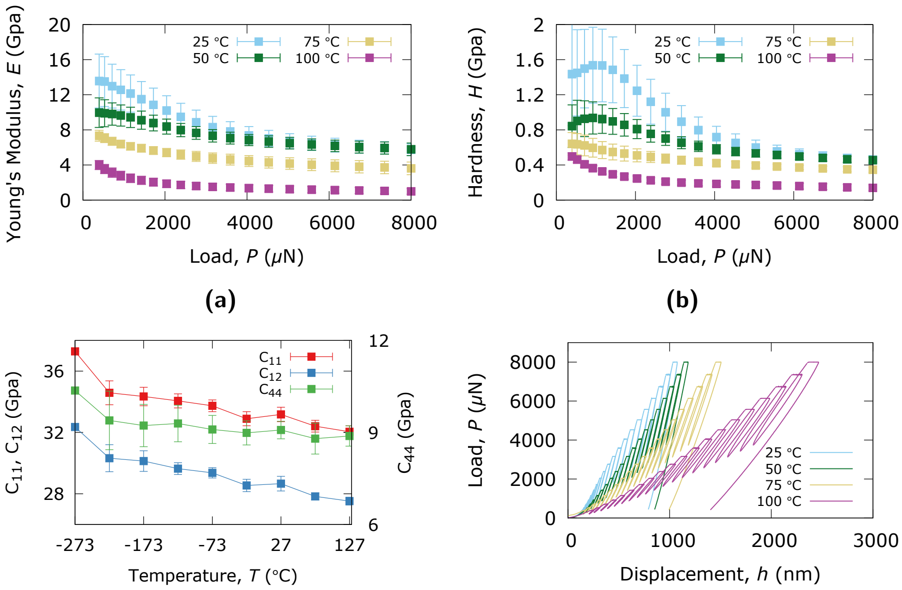

(a) **(b)** **(c)** **(d)**

Figure 6.8: *(a) Young's modulus as a function of load at various temperatures. (b) Hardness as a function of load at various temperatures. Error-bars of nanoindentations are standard deviations of ten indents for each temperature on the same crystal facet. (c) Variable-temperature elastic constants from molecular dynamics simulations. Lines are guidance to the eye. (d) Representative load-displacement curves at various temperatures.*

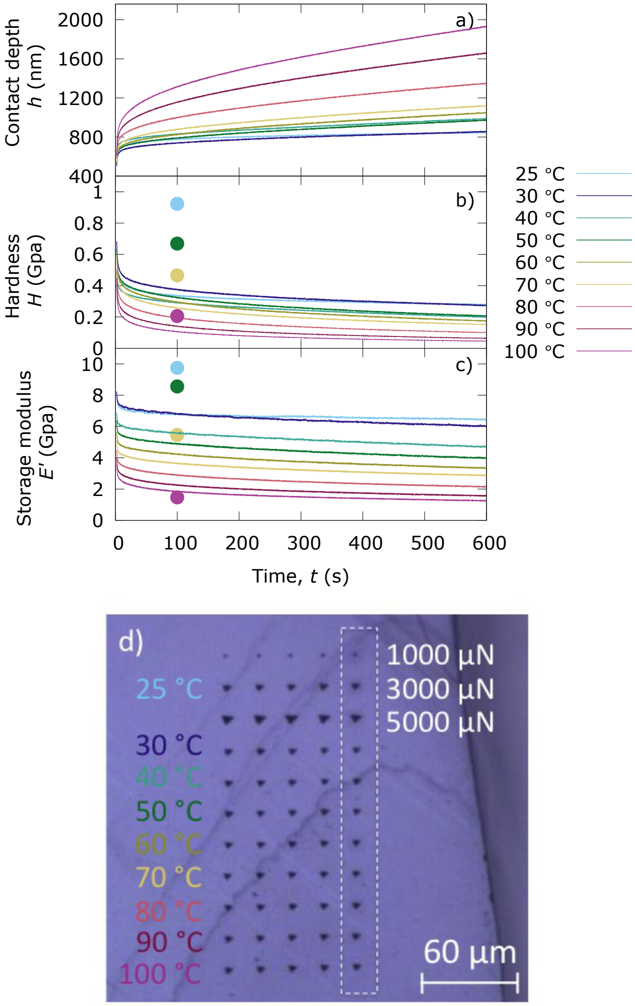

Figure 6.9: *Time evolution from 25 - 100 °C of the (a) contact depth (b) hardness and (c) storage modulus. Each temperature corresponds to a different position on the crystal facet. Each line represent a single creep test with sampling 20 times every second. Circles denote hardness and Young's moduli values from previous nanoindentations at P = 3000 μN. (d) Optical image of crystal facets subjected to creep analysis tests. Creep results are from indents in dashed rectangle at P = 3000 μN.*

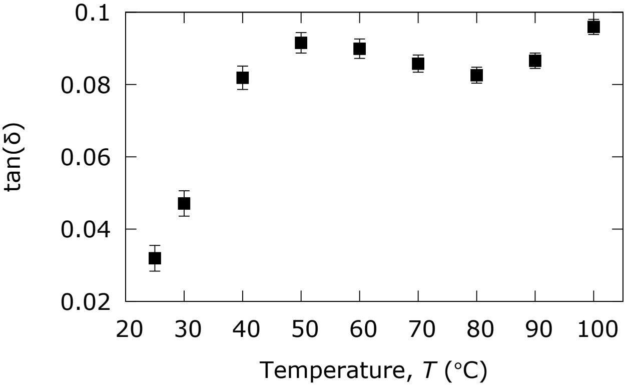

Figure 6.10: $\tan\delta$ *as function of temperature. Error-bars are standard deviations of five oscillating indents per temperature with every oscillating indents over* t *= 600 s with sampling 20 times every second*

This is consistent with the quasistatic nanoindentation results, where at higher loads the indent displacement becomes larger and the hardness decreases (see Figure 6.8b). The relative change of the hardness over time increases with increasing temperature. The storage modulus E', related to the energy stored in the material, follows a similar trend as the hardness and Young's modulus from nanoindentations (Figure 6.9c). The $\tan(\delta)$-value, which is a measurement of the viscoelasticity of a material, does not change appreciably over time. At room temperature, $\tan(\delta)$ = 0.032 ± 0.004 and this increases at T = 100 °C to 0.096 ± 0.002 indicating that the viscous contributions increase relative to the elastic contributions in the material with increasing temperatures (Figure 6.10).

To conclude, quasistatic nanoindentations, DMA experiments and classical molecular simulations show softening of HKUST-1 at increasing temperature, despite the material exhibiting NTE. The creep behavior we observe is substantial, with a reduction of 56% and 88% in the hardness after ten minutes at 25 °C and 100 °C, respectively. This first experimental study into the temperature-dependency of MOF elasticity and hardness properties provides important insight into the expected stability and performance characteristics of MOFs for a number of applications where a comprehensive mechanical property understanding is critical.

Acknowledgments

N.C.B. acknowledges the support of the Sandia National Laboratories Truman Fellowship Program and N.C.B. and R.W.F. acknowledge support by the Sandia National Laboratories Laboratory Directed Research and Development (LDRD) Program. Sandia National Laboratories is a multimission laboratory managed and operated by National Technology and Engineering Solutions of Sandia, LLC., a wholly owned subsidiary of Honeywell International, Inc., for the U.S. Department of Energy's National Nuclear Security Administration under contract DE-NA0003525. T.D.B. acknowledges the support of the Royal Society for a University Research Fellowship. J.H. acknowledges the support of the University of Amsterdam for an UvA385 grant. We acknowledge Jonathan Zimmerman for fruitful discussions. This work describes objective technical results and analysis. Any subjective views or opinions that might be expressed in this work do not necessarily represent the views of the U.S. Department of Energy or the United States Government.

Summary

Metal-organic frameworks (MOFs), or porous coordination polymers, have gained considerable interest in the past two decades due to their potential in a plethora of technological applications. These nanoporous materials consist of metal nodes interconnected by organic linker molecules forming an extended network. MOF-materials containing open-metal sites (OMS) are promising materials for the adsorptive separation of olefin/paraffin mixtures. Current technologies for *e.g.*, ethylene/ethane separations rely on expensive high-pressure cryogenic distillations. Open-metal sites interact more strongly with olefins compared to paraffins, which can lead to higher adsorption selectivities. Kohn-Sham density functional theory (KS-DFT) calculations provide useful electronic insight into these adsorption processes. However, the associated molecular orbital interactions are often unknown.

Chapter 2 reports a KS molecular orbital analysis of water adsorption on the OMS of the MOF HKUST-1. Hybrid functionals show better agreement with experimental magnetic and electronic properties than generalized gradient approximated (GGA) functionals. Analysis of the molecular orbitals reveals a Jahn-Teller distortion upon water adsorption due to antibonding interactions between the Cu($3d_{z2}$) and the highest occupied molecular orbital of water in the A1 irreducible representation. Donor-acceptor interactions show that empty Cu($4s$) and Cu($4p_z$)-orbitals on the opposite Cu-sites are populated, thereby explaining the reduced adsorption energy of the second adsorbed water molecule. A σ-bond is established between the two Cu-cations as was recently suggested using electron paramagnetic resonance.

HKUST-1 is, due to the open-metal site, an excellent candidate material for the adsorptive separation of ethylene/ethane mixtures. Knowledge of the multicomponent adsorption behavior is important to assess the full potential of the sorbent material. Measuring multicomponent adsorption isotherms experiment-

ally is rather challenging. Therefore, the ideal adsorbed solution theory (IAST) is widely used. Chapter 3 demonstrates that this theory breaks down in HKUST-1 for ethylene/ethane mixtures. Using KS-DFT molecular orbital analysis and an energy decomposition analysis scheme, a new force field potential is constructed that accounts for the donor-acceptor interactions between the open-metal site and ethylene that are missing in standard hydrocarbon force fields. The computed single component ethylene adsorption isotherm is in excellent agreement with the experimental adsorption isotherm in semi-logarithmic scale. By computing the multicomponent adsorption isotherms directly, it becomes clear that IAST fails at industrially relevant pressures. This suggests that a multiscale modeling approach is crucial in predicting complex adsorption behavior.

A key challenge for the commercialization of MOF-materials is to increase their mechanical stability. Therefore, an understanding of MOF mechanical properties is critical for their integration with technological applications. The majority of the reported mechanical properties are obtained from room temperature experiments or 0 Kelvin *ab initio* calculations. Typically, significant discrepancies are observed between the *ab initio* and room temperature values. An important reason for this discrepancy is temperature effects. Previously, thermomechanical properties of MOF-materials were unknown. Thermomechanical properties are not only important from an application perspective, such as in sensor devices and fixed-bed reactors, but also from a fundamental understanding of elasticity in MOFs.

In Chapter 4, state-of-the-art flexible force field models, which form an essential tool in predicting mechanical properties of MOFs, are reviewed. Various parameterization schemes, including the building block methodology and periodic phonons are discussed. Most (generic) force fields are able to reasonably reproduce lattice parameters, coefficients of thermal expansion and bulk moduli. However, there are still major challenges to overcome in order for force fields to be used to their full potential, such as the development of efficient sampling schemes.

Thermomechanical properties can be determined from knowledge of the variable-temperature elastic constants. Therefore, in Chapter 5, a new parameterization scheme is proposed that fits flexible force fields on the *ab initio* calculated elastic tensor. Furthermore, it is shown that framework flexibility has negligible influence on the adsorption and diffusion of small guest molecules in MIL-47(V).

Experimental thermomechanical and creep properties of HKUST-1 are presented in Chapter 6. Although HKUST-1 becomes denser due to negative thermal expansion, single crystal nanoindentations and dynamic mechanical analysis show a reduction of the Young's modulus and hardness upon increasing temperature. These findings are consistent with softening of the isothermal elastic constants calculated from classical molecular dynamics simulations. Creep analysis shows a large decrease of the aforementioned mechanical properties. These findings suggest that one has to rethink the use of HKUST-1 in technological applications.

Samenvatting

Metaal-organische roosters (metal-organic frameworks: MOF's), ofwel poreuze coördinatie polymeren, hebben aanzienlijk interesse gewekt in de afgelopen twee decennia vanwege de potentie in vele technologische toepassingen. Deze nanoporeuze materialen vormen uitgebreide netwerken bestaande uit metaalclusters die onderling verbonden zijn door organische 'linker' moleculen. MOF-materialen die vrije metaal posities (open-metal sites: OMS) bevatten zijn veelbelovende materialen voor de adsorptieve scheiding van olefine-paraffinemengsels. Huidige technologieën voor bijvoorbeeld etheen-ethaanscheidingen zijn gebaseerd op kostbare cryogene distillaties die opereren bij hoge druk. Vrij metaal posities hebben een sterkere interactie met olefinen dan met paraffinen en daardoor kan een hogere adsorptieselectiviteit worden behaald. Kohn-Sham dichtheidsfunctionaaltheorie (KS-DFT) kan electronisch inzicht bieden in dergelijke adsorptieprocessen. Desalniettemin zijn de daarbij horende molecuulorbitaal-interacties vaak niet bekend.

In hoofdstuk 2 wordt een Kohn-Sham molecuulorbitaalanalyse vermeld van wateradsorptie op een OMS in HKUST-1. Hybride functionalen komen beter overeen met experimenteel gemeten magnetische en electronische eigenschappen dan gegeneraliseerde gradiëntbenaderde functionalen. Molecuulorbitaalanalyse toont aan dat er een Jahn-Teller verstoring optreedt als water adsorbeert, vanwege de antibindende interactie tussen de Cu($3d_{\mathrm{z2}}$) en de hoogste bezette molecuulorbitaal van water in de A1 irreducibele representatie. Donor-acceptatie interacties tonen aan dat de lege Cu($4s$) en Cu($4p_z$)-orbitalen van het andere koperkation bezet worden. Dit verklaart de lagere adsorptie-energie van het tweede watermolecuul. Een σ-binding ontstaat tussen de twee koperkationen wat onlangs gesuggereerd werd op basis van electron paramagnetisch resonantie.

HKUST-1 is, vanwege de vrije metaal positie, een uitstekend materiaal voor de adsorptieve scheiding van etheen-ethaanmengsels. Het is belangrijk om inzicht te hebben in de multicomponentenadsorptie om de potentie van een adsorptiemateriaal vast te stellen. Het meten van multicomponentenadsorptie-isothermen is uitdagend. Daarom wordt vaak de ideaaladsorptiemengseltheorie (IAST) gebruikt. Hoofdstuk 3 laat zien dat deze theorie niet bruikbaar is in HKUST-1 voor etheen-ethaanmengsels. Door gebruik te maken van Kohn-Sham molecuulorbitaalanalyse en de bijbehorende energie decompositie-analyse, is een nieuwe krachtveldpotentiaal ontwikkeld die de donor-acceptatie interactie tussen etheen en de vrije metaal positie beschrijft die in standaard koolwaterstofkrachtvelden ontbreekt. De berekende ééncomponentadsorptie-isotherm komt erg goed overeen met de experimentele adsorptie-isotherm in semi-logaritmische schaal. Door het uitrekenen van de multicomponentenadsorptie-isotherm wordt aangetoond dat IAST niet bruikbaar is bij industrieel relevante druk. Deze resultaten suggereren dat een 'multiscale modeling' benadering cruciaal is om complex adsorptiegedrag te voorspellen.

Een belangrijke uitdaging in het commercialiseren van MOF-materialen is het vergroten van de mechanische stabiliteit. Het begrijpen van mechanische eigenschappen van MOF's is dus van belang voor de integratie in technologische toepassingen. Het merendeel van de gerapporteerde mechanische eigenschappen wordt verkregen door experimenten uitgevoerd op kamertemperatuur of door middel van *ab initio* 0 Kelvin computerberekeningen. Het is eigenaardig dat experimentele en berekende mechanische eigenschappen vaak slecht overeenkomen met elkaar. Een belangrijke reden voor deze afwijkingen zijn temperatuureffecten. Tot op heden zijn thermo-mechanische eigenschappen van MOF-materialen onbekend. Thermo-mechanische eigenschappen zijn niet alleen belangrijk vanuit een toepassingsperspectief, voor bijvoorbeeld sensorapparaten en vastbedreactoren, maar ook voor een fundamenteel begrip van elasticiteit in MOF's.

In hoofdstuk 4 worden moderne flexibele krachtveldmodellen bediscussieerd die een belangrijk hulpmiddel vormen in het voorspellen van mechanische eigenschappen in MOF's. Verschillende parameterizatie-schema's, waaronder de bouwsteen en periodieke fononen methoden, worden besproken. De meeste krachtvelden zijn in staat om de roosterparameters, coëfficienten van thermische expansie en bulkmoduli redelijk te voorspellen. Om krachtvelden tot hun volledige recht te laten komen, blijven grote uitdagingen bestaan zoals het ontwikkelen van efficiënte meetschema's.

Thermo-mechanische eigenschappen kunnen worden afgeleid vanuit de temperatuurafhankelijke elasticiteitsconstanten. Om deze reden wordt in hoofdstuk 5 een nieuw schema geïntroduceerd waarbij krachtveldpotentialen geparametriseerd worden op de *ab initio* berekende elasticiteitstensor. Er wordt aangetoond dat materiaalflexibiliteit een verwaarloosbaar effect heeft op de adsorptie en diffusie van kleine gastmoleculen in MIL-47(V).

Experimentele thermo-mechanische effecten en kruipeffecten van HKUST-1 worden gepresenteerd in hoofdstuk 6. Ondanks dat HKUST-1 een hogere dichtheid krijgt vanwege negatieve thermische expansie, laten éénkristalnanoindentatie experimenten een verlaging van de Youngs modulus en hardheid zien, bij verhoogde temperatuur. Deze bevindingen zijn consistent met een verlaging van de isothermische elasticiteitsconstanten verkregen uit klassieke moleculaire dynamica simulaties. Kruipanalyse laat een aanzienlijke verlaging zien van de hierboven genoemde mechanische eigenschappen. Deze bevindingen suggereren dat men het gebruik van HKUST-1 in technologische passingen wellicht moet herzien.

Bibliography

[1] Sholl, D. S.; P.Lively, R. *Nature* **2016**, *532*, 435–437.

[2] Humphrey, J.; Keller, G. *Separation Process Technology*; McGraw-Hill, 1997.

[3] Laboratory, O. R. N. Materials for Separation Technologies: Energy and Emission Reduction Opportunities. 2005.

[4] Kulprathipanja, S. *Zeolites in Industrial Separation and Catalysis*; Wiley-VCH, 2009.

[5] Yang, R. T. *Gas Separation by Adsorption Processes*; Imperial College Press, 1997.

[6] Li, J.-R.; Kuppler, R. J.; Zhou, H.-C. *Chem. Soc. Rev.* **2009**, *38*, 1477–1504.

[7] Van de Voorde, B.; Bueken, B.; Denayer, J.; De Vos, D. *Chem. Soc. Rev.* **2014**, *43*, 5766–5788.

[8] Krishna, R. *RSC Adv.* **2015**, *5*, 52269–52295.

[9] Li, H.; Eddaoudi, M.; O'Keeffe, M.; Yagh, O. M. *Nature* **1999**, *402*, 276–279.

[10] Brunauer, S.; Emmett, P. H.; Teller, E. *J. Am. Chem. Soc.* **1938**, *60*, 309–319.

[11] Wilmer, C. E.; Leaf, M.; Lee, C. Y.; Farha, O. K.; Hauser, B. G.; Hupp, J. T.; Snurr, R. Q. *Nat. Chem.* **2012**, *4*, 83–89.

[12] Chung, Y. G.; Camp, J.; Haranczyk, M.; Sikora, B. J.; Bury, W.; Krungleviciute, V.; Yildirim, T.; Farha, O. K.; Sholl, D. S.; Snurr, R. Q. *Chem. Mater.* **2014**, *26*, 6185–6192.

[13] Düren, T.; Sarkisov, L.; Yaghi, O. M.; Snurr, R. Q. *Langmuir* **2004**, *20*, 2683–2689.

[14] Farha, O. K.; Eryazici, I.; Jeong, N. C.; Hauser, B. G.; Wilmer, C. E.; Sarjeant, A. A.; Snurr, R. Q.; Nguyen, S. T.; Yazaydn, A. .; Hupp, J. T. *J. Am. Chem. Soc.* **2012**, *134*, 15016–15021.

[15] Torres Knoop, A.; Dubbeldam, D. *ChemPhysChem* **2015**, *16*, 2046–2067.

[16] Knoop, A. T. PhD thesis: Entropy-driven separations in nanoporous materials. 2016.

[17] Ariana, T.; Rajamani, K.; David, D. *Angew. Chem. Int. Ed.* **2014**, *53*, 7774–7778.

[18] Tian, T.; Zeng, Z.; Vulpe, D.; Casco, M. E.; Divitini, G.; Midgley, P. A.; Silvestre-Albero, J.; Tan, J.-C.; Moghadam, P. Z.; Fairen-Jimenez, D. *Nat. Mater.* **2017**, *17*, 174–179.

[19] Rogge, S. M. J.; Bavykina, A.; Hajek, J.; Garcia, H.; Olivos-Suarez, A. I.; Sepulveda-Escribano, A.; Vimont, A.; Clet, G.; Bazin, P.; Kapteijn, F.; Daturi, M.; Ramos-Fernandez, E. V.; Llabres i Xamena, F. X.; Van Speybroeck, V.; Gascon, J. *Chem. Soc. Rev.* **2017**, *46*, 3134–3184.

[20] Kotzabasaki, M.; Froudakis, G. E. *Inorg. Chem. Front.* **2018**, *5*, 1255–1272.

[21] Stassen, I.; Burtch, N. C.; Talin, A.; Falcaro, P.; Allendorf, M.; Ameloot, R. *Chem. Soc. Rev.* **2017**, *46*, 3185–3241.

[22] Schneemann, A.; Bon, V.; Schwedler, I.; Senkovska, I.; Kaskel, S.; Fischer, R. A. *Chem. Soc. Rev.* **2014**, *43*, 6062–6096.

[23] Chang, Z.; Yang, D.-H.; Xu, J.; Hu, T.-L.; Bu, X.-H. *Adv. Mater.* **2015**, *27*, 5432–5441.

[24] Coudert, F.-X. *Chem. Mater.* **2015**, *27*, 1905–1916.

[25] Serre, C.; Millange, F.; Thouvenot, C.; Nogus, M.; Marsolier, G.; Lour, D.; Frey, G. *J. Am. Chem. Soc.* **2002**, *124*, 13519–13526.

[26] Millange, F.; Serre, C.; Ferey, G. *Chem. Commun.* **2002**, 822–823.

[27] Horcajada, P.; Gref, R.; Baati, T.; Allan, P. K.; Maurin, G.; Couvreur, P.; Férey, G.; Morris, R. E.; Serre, C. *Chem. Rev.* **2012**, *112*, 1232–1268.

[28] Serre, C.; Bourrelly, S.; Vimont, A.; Ramsahye, N.; Maurin, G.; Llewellyn, P.; Daturi, M.; Filinchuk, Y.; Leynaud, O.; Barnes, P.; Frey, G. *Adv. Mater.* **2007**, *19*, 2246–2251.

[29] Miller, W.; Smith, C. W.; Mackenzie, D. S.; Evans, K. E. *J. Mater. Sci.* **2009**, *44*, 5441–5451.

[30] Wu, Y.; Kobayashi, A.; Halder, G.; Peterson, V.; Chapman, K.; Lock, N.; Southon, P.; Kepert, C. *Angew. Chem. Int. Ed.* **2008**, *47*, 8929–8932.

[31] Peterson, V.; Kearley, G.; Wu, Y.; Ramirez-Cuesta, A.; Kemner, E.; Kepert, C. *Angew. Chem. Int. Ed.* **2010**, *49*, 585–588.

[32] Ryder, M. R.; Civalleri, B.; Cinque, G.; Tan, J.-C. *CrystEngComm* **2016**, *18*, 4303–4312.

[33] Ryder, M. R.; Van de Voorde, B.; Civalleri, B.; Bennett, T. D.; Mukhopadhyay, S.; Cinque, G.; Fernandez-Alonso, F.; De Vos, D.; Rudić, S.; Tan, J.-C. *Phys. Rev. Lett.* **2017**, *118*, 255502.

[34] Ortiz, A. U.; Boutin, A.; Fuchs, A. H.; Coudert, F.-X. C. *Phys. Rev. Lett.* **2012**, *109*, 195502.

[35] Ortiz, A. U.; Boutin, A.; Fuchs, A. H.; Coudert, F.-X. *J. Chem. Phys.* **2013**, *138*, 174703.

[36] Henke, S.; Li, W.; Cheetham, A. K. *Chem. Sci.* **2014**, *5*, 2392–2397.

[37] Nye, J. F. *Physical Properties of Crystals*; Oxford University Press, 1957.

[38] Voigt, W. *Lehrbuch der Kristallphysiki*; B. G. Teubner, Leipzig and Berlin, 1910.

[39] Tan, J.-C.; Civalleri, B.; Lin, C.-C.; Valenzano, L.; Galvelis, R.; Chen, P.-F.; Bennett, T. D.; Mellot-Draznieks, C.; Zicovich-Wilson, C. M.; Cheetham, A. K. *Phys. Rev. Lett.* **2012**, *108*, 095502.

[40] Tan, J. C.; Cheetham, A. K. *Chem. Soc. Rev.* **2011**, *40*, 1059–1080.

[41] Li, W.; Henke, S.; Cheetham, A. K. *APL Materials* **2014**, *2*, 123902.

[42] Burtch, N. C.; Heinen, J.; Bennett, T. D.; Dubbeldam, D.; Allendorf, M. D. *Adv. Mater.* **2017**, 1704124.

[43] Rogge, S. M. J.; Waroquier, M.; Van Speybroeck, V. *Acc. Chem. Res.* **2018**, *51*, 138–148.

[44] Rubio-Martinez, M.; Avci-Camur, C.; Thornton, A. W.; Imaz, I.; Maspoch, D.; Hill, M. R. *Chem. Soc. Rev.* **2017**, *46*, 3453–3480.

[45] Noorden, R. V.; Maher, B.; Nuzzo, R. *Nature* **2014**, *514*, 550–553.

[46] Nobel Prizes in chemistry of 1998 and 2013 awarded to computational chemists. `https://www.nobelprize.org/nobel_prizes/chemistry/laureates/`, Accessed: 2018-02-11.

[47] Wu, H.; Zhou, W.; Yildirim, T. *J. Am. Chem. Soc.* **2007**, *129*, 5314–5315.

[48] Top 500 list. `http://www.top500.org`, List of June 2018. Accessed: 04-07-2018.

[49] Supercomputing's Super Energy Needs, and What to Do About Them. https://cacm.acm.org/news/192296-supercomputings-super-energy-needs-and-what-to-do-about-them/fulltext, Accessed: 12-06-2018.

[50] Tan, J. C.; Bennett, T. D.; Cheetham, A. K. *Proc. Natl. Acad. Sci.* **2010**, *107*, 9938–9943.

[51] Botu, V.; Batra, R.; Chapman, J.; Ramprasad, R. *J. Phys. Chem. C* **2017**, *121*, 511–522.

[52] Kandala, A.; Mezzacapo, A.; Temme, K.; Takita, M.; Brink, M.; Chow, J. M.; Gambetta, J. M. *Nature* **2017**, *549*, 242–246.

[53] McWeeny, R. *Methods of Molecular Quantum Mechanics*, 2nd ed.; Academic Press, 1978.

[54] Griffiths, D. J. *Introduction to Quantum Mechanics*; Pearson Education, Inc., 2005.

[55] Martin, R. M. *Electronic Structure: Basic Theory and Practical Methods*, 7th ed.; Cambridge University Press, 2013.

[56] Born, M.; Oppenheimer, R. *Ann. Phys.* **1927**, *389*, 457–484.

[57] Jensen, F. *Introduction to Computational Chemistry*; John Wiley & Sons, Ltd., 2009.

[58] Bernhard, S. H. *Wiley Interdiscip. Rev. Comput. Mol. Sci.* **2011**, *1*, 790–809.

[59] Becke, A. D. *J. Chem. Phys.* **2014**, *140*, 18A301.

[60] Hohenberg, P.; Kohn, W. *Phys. Rev.* **1964**, *136*, B864–B871.

[61] Kohn, W.; Sham, L. J. *Phys. Rev.* **1965**, *140*, A1133–A1138.

[62] Perdew, J. P.; Schmidt, K. *AIP Conf. Proc.* **2001**, *577*, 1–20.

[63] Mardirossian, N.; Head-Gordon, M. *Mol. Phys.* **2017**, *115*, 2315–2372.

[64] Peverati, R.; Truhlar, D. G. *Philos. Trans. A Math Phys. Eng. Sci.* **2014**, *372*.

[65] Kepp, K. P. *Science* **2017**, *356*, 496–496.

[66] Medvedev, M. G.; Bushmarinov, I. S.; Sun, J.; Perdew, J. P.; Lyssenko, K. A. *Science* **2017**, *356*, 496–496.

[67] Hammes-Schiffer, S. *Science* **2017**, *355*, 28–29.

[68] The annual popularity poll for density functionals: edition 2017. `http://www.marcelswart.eu/dft-poll/newsitem.pdf`, Access: 13-06-2018.

[69] Payne, M. C.; Teter, M. P.; Allan, D. C.; Arias, T. A.; Joannopoulos, J. D. *Rev. Mod. Phys.* **1992**, *64*, 1045–1097.

[70] Monkhorst, H. J.; Pack, J. D. *Phys. Rev. B* **1976**, *13*, 5188–5192.

[71] Hamann, D. R.; Schlüter, M.; Chiang, C. *Phys. Rev. Lett.* **1979**, *43*, 1494–1497.

[72] Vanderbilt, D. *Phys. Rev. B* **1990**, *41*, 7892–7895.

[73] Troullier, N.; Martins, J. L. *Phys. Rev. B* **1991**, *43*, 1993–2006.

[74] Blöchl, P. E. *Phys. Rev. B* **1994**, *50*, 17953–17979.

[75] Kresse, G.; Joubert, D. *Phys. Rev. B* **1999**, *59*, 1758–1775.

[76] Kresse, G.; Hafner, J. *Phys. Rev. B* **1993**, *47*, 558–561.

[77] Kresse, G.; Furthmüller, J. *Phys. Rev. B* **1996**, *54*, 11169–11186.

[78] Velde, G. T.; Bickelhaupt, F. M.; Baerends, E. J.; Fonseca Guerra, C.; Gisbergen, S. J. A. V.; Snijders, J. G.; Ziegler, T. *J. Comp. Chem.* **2001**, *22*, 931–967.

[79] Baerends, E. J. et al. ADF2016, SCM, Theoretical Chemistry, Vrije Universiteit, Amsterdam, The Netherlands, https://www.scm.com.

[80] Fonseca Guerra, C.; Snijders, J. G.; te Velde, G. T.; Baerends, E. J. *Theor. Chem. Acc.* **1998**, *99*, 391–403.

[81] Slater, J. C. *Phys. Rev.* **1930**, *36*, 57–64.

[82] Morokuma, K. *J. Chem. Phys.* **1971**, *55*, 1236–1244.

[83] Kazuo, K.; Keiji, M. *Int. J. Quantum Chem.* **1976**, *10*, 325–340.

[84] Ziegler, T.; Rauk, A. *Inorg. Chem.* **1979**, *18*, 1755–1759.

[85] Ziegler, T.; Rauk, A. *Inorg. Chem.* **1979**, *18*, 1558–1565.

[86] Bickelhaupt, F. M.; Baerends, E. J. *Rev. Comput. Chem.*; John Wiley & Sons, Inc., 2007; pp 1–86.

[87] Fonseca Guerra, C.; Handgraaf, J. W.; Baerends, E. J.; Bickelhaupt, F. M. *J. Comp. Chem.* **2003**, *25*, 189–210.

[88] Voronoi, G. *J. Reine. Angew. Math.* **1908**, *134*, 198–287.

[89] Pathria, R. K. *Statistical Mechanics*; Pergamon Press, 1986.

[90] Tuckerman, M. *Statistical Mechanics: Theory and Molecular Simulations*; Oxford University Press, New York, 2010.

[91] Graben, H.; Ray, J. R. *Mol. Phys.* **1993**, *80*, 1183–1193.

[92] Berendsen, H. J. C.; van Gunsteren, W. F. Practical algorithms for dynamics simulations. 1986.

[93] Verlet, L. *Phys. Rev.* **1967**, *159*, 98–103.

[94] Andersen, H. C. *J. Chem. Phys.* **1980**, *72*, 2384–2393.

[95] Parrinello, M.; Rahman, A. *Phys. Rev. Lett.* **1980**, *45*, 1196–1199.

[96] Parrinello, M.; Rahman, A. *J. Appl. Phys.* **1981**, *52*, 7182–7190.

[97] Ray, J. R.; Rahman, A. *J. Chem. Phys.* **1984**, *80*, 4423–4428.

[98] Ray, J. R.; Moody, M. C.; Rahman, A. *Phys. Rev. B* **1985**, *32*, 733–735.

[99] Landau, L. D.; Lifshitz, E. M. *Theory of Elasticity*, 3rd ed.; Elsevier Ltd., 1986.

[100] Wallace, D. C. *Thermodynamics of Crystals*; John Wiley & Sons, 1972.

[101] Van Workum, K.; Yoshimoto, K.; de Pablo, J. J.; Douglas, J. F. *Phys. Rev. E* **2005**, *71*, 061102.

[102] Lutsko, J. F. *J. Appl. Phys.* **1989**, *65*, 2991–2997.

[103] Bučko, T.; Hafner, J.; Ángyán, J. G. *J. Chem. Phys.* **2005**, *122*, 124508.

[104] Banerjee, A.; Adams, N.; Simons, J.; Shepard, R. *J. Phys. Chem.* **1985**, *89*, 52–57.

[105] Baker, J. *J. Comput. Chem.* **1986**, *7*, 385–395.

[106] Metropolis, N.; Rosenbluth, A. W.; Rosenbluth, M. N.; Teller, A. H.; Teller, E. *J. Chem. Phys.* **1953**, *21*, 1087–1092.

[107] Nicholson D, P. N. *Computer simulation and the statistical mechanics of adsorption*; New York: Academic Press, 1988.

[108] Frenkel, D.; Smit, B. *Understanding Molecular Simulation: From Algorithms to Applications*, 2nd ed.; Academic Press, 2001.

[109] Peng, D.-Y.; Robinson, D. B. *Ind. Eng. Chem. Fundam.* **1976**, *15*, 59–64.

[110] Ray, J. R.; Graben, H. W. *J. Chem. Phys.* **1990**, *93*, 4296–4298.

[111] Graben, H. W.; Ray, J. R. *Phys. Rev. A* **1991**, *43*, 4100–4103.

[112] Stockmayer, W. H. *J. Chem. Phys.* **1950**, *18*, 58–61.

[113] Wolf, R. J.; Lee, M. W.; Davis, R. C. *Phys. Rev. B* **1993**, *48*, 12415–12418.

[114] Coudert, F.-X.; Jeffroy, M.; Fuchs, A. H.; Boutin, A.; Mellot-Draznieks, C. *J. Am. Chem. Soc.* **2008**, *130*, 14294–14302.

[115] Coudert, F.-X.; Boutin, A.; Jeffroy, M.; Mellot-Draznieks, C.; Fuchs, A. H. *ChemPhysChem* **2011**, *12*, 247–258.

[116] Dubbeldam, D.; Calero, S.; Ellis, D. E.; Snurr, R. Q. *Mol. Simul.* **2016**, *42*, 81–101.

[117] Dubbeldam, D.; Calero, S.; Vlugt, T. J. *Mol. Simul.* **2018**, *44*, 653–676.

[118] Allen, M.; Tildesley, D. *Computer Simulation of Liquids*; Clarendon Press, Oxford, 1987.

[119] Leach, A. *Molecular Modelling: Principles and Applications*, 2nd ed.; Prentice Hall, Longman, Essex, England, 2001.

[120] Huck, J. M.; Lin, L.-C.; Berger, A. H.; Shahrak, M. N.; Martin, R. L.; Bhown, A. S.; Haranczyk, M.; Reuter, K.; Smit, B. *Energy Environ. Sci.* **2014**, *7*, 4132–4146.

[121] Jiang, J. *Metal-Organic Frameworks Materials Modeling towards Potential Engineering Applications*; Pan Stanford Publishing, 2015.

[122] Chui, S.; S. Lo, J. C.; A. Orpen, I. W. *Science* **1999**, *283*, 1148–1150.

[123] Lin, L.-C.; Berger, A. H.; Martin, R. L.; Kim, J.; Swisher, J. A.; Jariwala, K.; Rycroft, C. H.; Bhown, A. S.; Deem, M. W.; Haranczyk, M.; Smit, B. *Nat. Mater.* **2012**, *11*, 633–641.

[124] Ksgens, P.; Rose, M.; Senkovska, I.; Frde, H.; Henschel, A.; Siegle, S.; Kaskel, S. *Micropor. Mesopor. Mat.* **2009**, *120*, 325– 330.

[125] DeCoste, J. B.; Peterson, G. W.; Schindler, B. J.; Killops, K. L.; Browe, M. A.; Mahle, J. J. *J. Mater. Chem. A* **2013**, *1*, 11922–11932.

[126] Burtch, N. C.; Jasuja, H.; Walton, K. S. *Chem. Rev.* **2014**, *114*, 10575–10612.

[127] Todaro, M.; Buscarino, G.; Sciortino, L.; Alessi, A.; Messina, F.; Taddei, M.; Ranocchiari, M.; Cannas, M.; Gelardi, F. M. *J. Phys. Chem. C* **2016**, *120*, 12879–12889.

[128] Henninger, S. K.; Jeremias, F.; Kummer, H.; Janiak, C. *Eur. J. Inorg. Chem.* **2012**, *2012*, 2625–2634.

[129] Huang, L.; Bandosz, T.; Joshi, K. L.; van Duin, A. C. T.; Gubbins, K. E. *J. Chem. Phys.* **2013**, *138*, 034102.

[130] Singh, M. P.; Dhumal, N. R.; Kim, H. J.; Kiefer, J.; Anderson, J. A. *J. Phys. Chem. C* **2016**, *120*, 17323–17333.

[131] Fang, Z.; Drholt, J. P.; Kauer, M.; Zhang, W.; Lochenie, C.; Jee, B.; Albada, B.; Metzler-Nolte, N.; Pppl, A.; Weber, B.; Muhler, M.; Wang, Y.; Schmid, R.; Fischer, R. A. *J. Am. Chem. Soc.* **2014**, *136*, 9627–9636.

[132] Liu, J.; Wang, Y.; Benin, A. I.; Jakubczak, P.; Willis, R. R.; LeVan, M. D. *Langmuir* **2010**, *26*, 14301–14307.

[133] Yu, J.; Ma, Y.; Balbuena, P. B. *Langmuir* **2012**, *28*, 8064–8071.

[134] Yazaydın, A.; Benin, A. I.; Faheem, S. A.; Jakubczak, P.; Low, J. J.; Willis, R. R.; Snurr, R. Q. *Chem. Mater.* **2009**, *21*, 1425–1430.

[135] Yu, J.; Wu, Y.; Balbuena, P. B. *ACS Sustain. Chem. Eng.* **2016**, *4*, 2387–2394.

[136] Hay, P. J.; Thibeault, J. C.; Hoffmann, R. *J. Am. Chem. Soc.* **1975**, *97*, 4884–4899.

[137] Grajciar, L.; Bludský, O.; Nachtigall, P. *J. Phys. Chem. Lett.* **2010**, *1*, 3354–3359.

[138] Manz, T. A.; Sholl, D. S. *J. Chem. Theory Comput.* **2010**, *6*, 2455–2468.

[139] Bureekaew, S.; Amirjalayer, S.; Schmid, R. *J. Mater. Chem.* **2012**, *22*, 10249–10254.

[140] Toda, J.; Fischer, M.; Jorge, M.; Gomes, J. R. B. *Chem. Phys. Lett.* **2013**, *587*, 7–13.

[141] Hijikata, Y.; Sakaki, S. *Inorg. Chem.* **2014**, *53*, 2417–2426.

[142] Alzahrani, K. A. H.; Deeth, R. J. *Dalton Trans.* **2016**, *45*, 11944–11948.

[143] Figgis, B. N.; Martin, R. L. *J. Chem. Soc.* **1956**, 3837–3846.

[144] Tonnet, M. L.; Yamada, S.; Ross, I. G. *Trans. Faraday Soc.* **1964**, *60*, 840–849.

[145] Royer, D. J. *Inorg. Chem.* **1965**, *4*, 1830–1832.

[146] Goodgame, D. M. L.; Hill, N. J.; Marsham, D. F.; Skapski, A. C.; Smart, M. L.; Troughton, P. G. H. *J. Chem. Soc. D* **1969**, 629–630.

[147] Pöppl, A.; Kunz, S.; Himsl, D.; Hartmann, M. *J Phys. Chem. C* **2008**, *112*, 2678–2684.

[148] Zhang, X. X.; Chui, S. S.-Y.; Williams, I. D. *J. Appl. Phys.* **2000**, *87*, 6007–6009.

[149] Ruiz, E.; Cano, J.; Alvarez, S.; Alemany, P. *J. Comp. Chem.* **1999**, *20*, 1391–1400.

[150] Eliseo, R.; Antonio, R.; Joan, C.; Santiago, A.; Pere, A. *J. Comp. Chem.* **2003**, *24*, 982–989.

[151] Koch, W.; Holthausen, M. C. *A Chemist's Guide to Density Functional Theory*; Wiley-VCH Verlag GmbH, 2001.

[152] Valero, R.; Costa, R.; de P. R. Moreira, I.; Truhlar, D. G.; Illas, F. *J. Chem. Phys.* **2008**, *128*, 114103.

[153] Neese, F. *Coord. Chem. Rev.* **2009**, *253*, 526 – 563.

[154] Grajciar, L.; Nachtigall, P.; Bludsk, O.; Rube, M. *J. Chem. Theory Comput.* **2015**, *11*, 230–238.

[155] Gu, Z.-G.; Heinke, L.; Wöll, C.; Neumann, T.; Wenzel, W.; Li, Q.; Fink, K.; Gordan, O. D.; Zahn, D. R. T. *Appl. Phys. Lett.* **2015**, *107*, 183301.

[156] Heisenberg, W. *Z. Phys.* **1928**, *49*, 619.

[157] Noodleman, L.; Case, D. A. In *Density-Functional Theory of Spin Polarization and Spin Coupling in Iron-Sulfur Clusters*; Cammack, R., Ed.; Adv. Inorg. Chem.; Academic Press, 1992; Vol. 38; pp 423 – 470.

[158] Noodleman, L. *J. Chem. Phys.* **1981**, *74*, 5737–5743.

[159] Cramer, C. J.; Truhlar, D. G. *Phys. Chem. Chem. Phys.* **2009**, *11*, 10757–10816.

[160] Perdew, J. P.; Ernzerhof, M.; Burke, K.; Savin, A. *Int. J. Quantum Chem.* **1997**, *61*, 197–205.

[161] Garikoitz, B.; Oscar, C.; Urko, G.; P., G. J.; Antonio, L.; Martín, M.; Pascual, R. *Eur. J. Inorg. Chem.* **2005**, *2005*, 2586–2589.

[162] Ruiz, E.; Alvarez, S.; Cano, J.; Polo, V. *J. Chem. Phys.* **2005**, *123*, 164110.

[163] Adamo, C.; Barone, V.; Bencini, A.; Broer, R.; Filatov, M.; Harrison, N. M.; Illas, F.; Malrieu, J. P.; de P. R. Moreira, I. *J. Chem. Phys.* **2006**, *124*, 107101.

[164] Ruiz, E.; Cano, J.; Alvarez, S.; Polo, V. *J. Chem. Phys.* **2006**, *124*, 107102.

[165] Yamaguchi, K.; Jensen, F.; Dorigo, A.; Houk, K. *Chem. Phys. Lett.* **1988**, *149*, 537–542.

[166] Stephens, P. J.; Devlin, F. J.; Chabalowski, C. F.; Frisch, M. J. *J. Phys. Chem.* **1994**, *98*, 11623–11627.

[167] Grimme, S.; Antony, J.; Ehrlich, S.; Krieg, H. *J. Chem. Phys.* **2010**, *132*, 154104.

[168] Hendon, C. H.; Walsh, A. *Chem. Sci.* **2015**, *6*, 3674–3683.

[169] Noodleman, L.; Baerends, E. J. *J. Am. Chem. Soc.* **1984**, *106*, 2316–2327.

[170] Cramer, C. J. *Essentials of Computational Chemistry: Theories and Models*; John Wiley & Sons, Ltd, 2002.

[171] Caballol, R.; ; Castell, O.; Illas, F.; ; de P. R. Moreira, I.; Malrieu, J. P. *J. Phys. Chem. A* **1997**, *101*, 7860–7866.

[172] Ferreira, D. E.; Almeida, W. B. D.; Neves, A.; Rocha, W. R. *Comput. Theor. Chem.* **2012**, *979*, 89 – 95.

[173] Pople, J. A. *Rev. Mod. Phys.* **1999**, *71*, 1267–1274.

[174] Bak, J. H.; Le, V.-D.; Kang, J.; Wei, S.-H.; Kim, Y.-H. *J. Phys. Chem. C* **2012**, *116*, 7386–7392.

[175] Prestipino, C.; Regli, L.; Vitillo, J. G.; Bonino, F.; Damin, A.; Lamberti, C.; Zecchina, A.; Solari, P. L.; Kongshaug, K. O.; Bordiga, S. *Chem. Mater.* **2006**, *18*, 1337–1346.

[176] Yang, R. T. *Gas separation by adsorption processes*; Imperial College Press, 2008.

[177] A. B. D Haan, H., .; Bosch *Industrial Separation Processes: Fundamentals*; De Gruyter, 2013.

[178] Talu, O. *Adv. Colloid Interface Sci.* **1998**, *7677*, 227–269.

[179] Myers, A. L.; Prausnitz, J. M. *AIChE J.* **1965**, *11*, 121–127.

[180] Cessford, N. F.; Seaton, N. A.; Düren, T. *Ind. Eng. Chem. Res.* **2012**, *51*, 4911–4921.

[181] Dewar, M. *Bull. Soc. Chim. Fr.* **1951**, *18*, C79.

[182] J. Chatt, L. A. D. *J. Chem. Soc.* **1953**, 2939–2947.

[183] J. Chatt, L. M. V., L. A. Duncanson *J. Chem. Soc.* **1955**, 4456–4460.

[184] T. Düren, R. Q. S., Y. S. Bae *Chem. Soc. Rev.* **2009**, *38*, 1237–1247.

[185] Dubbeldam, D.; Knoop, A. T.; Walton, K. S. *Mol. Simul.* **2013**, *39*, 1253–1292.

[186] Liu, B.; Smit, B.; Rey, F.; S. Valencia, S. C. *J. Phys. Chem. C* **2008**, *112*, 2492–2498.

[187] Gutiérrez-Sevillano, J. J.; Vicent-Luna, J. M.; Dubbeldam, D.; Calero, S. *J. Phys. Chem. C* **2013**, *117*, 11357–11366.

[188] T. Ziegler, A. R. *Theor. Chim. Acta.* **1977**, *46*, 110.

[189] Dubbeldam, D.; Calero, S.; Vlugt, T. J. H.; Krishna, R.; Maesen, T. L. M.; Beerdsen, E.; Smit, B. *Phys. Rev. Lett.* **2004**, *93*, 088302.

[190] Fischer, M.; Fröba, J. G. M.; Jorge, M. *Langmuir* **2012**, *28*, 8537–8549.

[191] Jorge, M.; Fischer, M.; Gomes, J. R. B.; Siquet, C.; Santos, J. C.; Rodrigues, A. E. *Ind. Eng. Chem. Res.* **2014**, *53*, 15475–15487.

[192] Chen, L.; Grajciar, L.; Nachtigall, P.; Düren, T. *J. Phys. Chem. C* **2011**, *115*, 23074–23080.

[193] Fang, H.; Demir, H.; Kamakoti, P.; Sholl, D. S. *J. Mater. Chem. A* **2014**, *2*, 274–291.

[194] McDaniel, J. G.; Schmidt, J. *Annu. Rev. Phys. Chem.* **2016**, *67*, 467– 488.

[195] Dzubak, A. L.; Lin, L. C.; Kim, J.; Swisher, J. A.; Poloni, R.; Maximoff, S. N.; Smit, B.; Gagliardi, L. *Nat. Chem.* **2012**, *4*, 810–816.

[196] Marx, S.; Kleist, W.; Baiker, A. *J. Catal.* **2011**, *281*, 76–87.

[197] Schlesinger, M.; Schulze, S.; Hietschold, M.; Mehring, M. *Micro. Mesopor. Mater.* **2010**, *132*, 121–127.

[198] Zhao, Y.; Truhlar, D. G. *J. Chem. Phys.* **2006**, *125*, 194101.

[199] Valero, R.; Costa, R.; de P. R. Moreira, I.; Truhlar, D. G.; Illas, F. *J. Chem. Phys.* **2008**, *128*, 114103.

[200] Mayo, S. L.; Olafson, B. D.; Goddard, W. A. *J. Phys Chem.* **1990**, *94*, 8897–8909.

[201] Siepmann, J. I. *Mol. Phys.* **1990**, *70*, 1145–1158.

[202] Siepmann, J. I.; Frenkel, D. *Mol. Phys.* **1992**, *75*, 59–70.

[203] Frenkel, D.; Mooij, G. C. A. M.; Smit, B. *J. Phys.: Condens. Matter* **1992**, *4*, 3053.

[204] Orhan, T.; L., M. A. *AIChE J.* **2004**, *47*, 1160–1168.

[205] Mayo, S. L.; Olafson, B. D.; Goddard, W. A. *J. Phys. Chem.* **1990**, *94*, 8897–8909.

[206] Karavias, A. L. F.; Myers, L. *Langmuir* **1991**, *7*, 3118–3126.

[207] Fonseca Guerra, C.; Bickelhaupt, F. M.; Baerends, E. J. *ChemPhysChem* **2004**, *5*, 481487.

[208] The transition state scheme computes the orbital interaction per symmetry contribution. For metaGGA functionals a correction is added to the orbital interactions, since an approximate Fock operator is used. See also, Scientific Computing & Modelling NV, ADF Manual, Release 2014, page 21.

[209] van Santen, R. A.; Baerends, E. J. In *Theoretical treatment of large molecules and their interactions*; Maksic, Z., Ed.; Springer, 1999; pp 323–389.

[210] Kaplan, I. G. *Intermolecular Interactions: Physical Picture, Computational Methods and Model Potentials*; John Wiley & Sons, Ltd, 2006.

[211] Fonseca Guerra, C.; Handgraaf, J. W.; Baerends, E. J.; Bickelhaupt, F. M. *J. Comp. Chem.* **2004**, *25*, 189–210.

[212] Mitoraj, M. P.; Michalak, A.; Ziegler, T. *J. Chem. Theory and Comput.* **2009**, *5*, 962–975.

[213] Israelachvili, J. N. *Intermolecular and Surface Forces*, 3rd ed.; Academic Press, 2011.

[214] Weeks, J. D.; Chandler, D.; Andersen, H. C. *J. Chem. Phys.* **1971**, *54*, 5237–5247.

[215] Petkov, P. S.; Vayssilov, G. N.; Liu, J.; Shekhah, O.; Wang, Y.; Wll, C.; Heine, T. *ChemPhysChem* **2012**, *13*, 2025–2029.

[216] He, Y.; Krishna, R.; Chen, B. *Energy Environ. Sci.* **2012**, *5*, 9107–9120.

[217] Dubbeldam, D.; Walton, K.; Ellis, D.; Snurr, R. *Angew. Chem. Int. Ed.* **2007**, *46*, 4496–4499.

[218] Balestra, S. R. G.; Bueno-Perez, R.; Hamad, S.; Dubbeldam, D.; Ruiz-Salvador, A. R.; Calero, S. *Chem. Mater.* **2016**, *28*, 8296–8304.

[219] Canepa, P.; Tan, K.; Du, Y.; Lu, H.; Chabal, Y. J.; Thonhauser, T. *J. Mater. Chem. A* **2015**, *3*, 986–995.

[220] Bennett, T. D.; Simoncic, P.; Moggach, S. A.; Gozzo, F.; Macchi, P.; Keen, D. A.; Tan, J.-C.; Cheetham, A. K. *Chem. Commun.* **2011**, *47*, 7983–7985.

[221] Ortiz, A. U.; Boutin, A.; Fuchs, A. H.; Coudert, F.-X. *J. Phys. Chem. Lett.* **2013**, *4*, 1861–1865.

[222] Mouhat, F.; Bousquet, D.; Boutin, A.; Boussel du Bourg, L.; Coudert, F.-X.; Fuchs, A. H. *J. Phys. Chem. Lett.* **2015**, *6*, 4265–4269.

[223] Llewellyn, P. L.; Maurin, G.; Devic, T.; Loera-Serna, S.; Rosenbach, N.; Serre, C.; Bourrelly, S.; Horcajada, P.; Filinchuk, Y.; Frey, G. *J. Am. Chem. Soc.* **2008**, *130*, 12808–12814.

[224] Neimark, A. V.; Coudert, F.-X.; Boutin, A.; Fuchs, A. H. *J. Phys. Chem. Lett.* **2010**, *1*, 445–449.

[225] Neimark, A. V.; Coudert, F.-X.; Triguero, C.; Boutin, A.; Fuchs, A. H.; Beurroies, I.; Denoyel, R. *Langmuir* **2011**, *27*, 4734–4741.

[226] Horcajada, P. et al. *J. Am. Chem. Soc.* **2011**, *133*, 17839–17847.

[227] Krause, S.; Bon, V.; Senkovska, I.; Stoeck, U.; Wallacher, D.; Többens, D. M.; Zander, S.; Pillai, R. S.; Maurin, G.; Coudert, F.-X.; Kaskel, S. *Nature* **2016**, *532*, 348–352.

[228] Evans, J. D.; Bocquet, L.; Coudert, F.-X. *Chem* **2016**, *1*, 873 – 886.

[229] Ryder, M. R.; Civalleri, B.; Bennett, T. D.; Henke, S.; Rudić, S.; Cinque, G.; Fernandez-Alonso, F.; Tan, J.-C. *Phys. Rev. Lett.* **2014**, *113*, 215502.

[230] Casco, M. E.; Cheng, Y. Q.; Daemen, L. L.; Fairen-Jimenez, D.; Ramos-Fernandez, E. V.; Ramirez-Cuesta, A. J.; Silvestre-Albero, J. *Chem. Commun.* **2016**, *52*, 3639–3642.

[231] Fairen-Jimenez, D.; Moggach, S. A.; Wharmby, M. T.; Wright, P. A.; Parsons, S.; Dren, T. *J. Am. Chem. Soc.* **2011**, *133*, 8900–8902.

[232] Tanaka, S.; Fujita, K.; Miyake, Y.; Miyamoto, M.; Hasegawa, Y.; Makino, T.; Van der Perre, S.; Cousin Saint Remi, J.; Van Assche, T.; Baron, G. V.; Denayer, J. F. M. *J. Phys. Chem. C* **2015**, *119*, 28430–28439.

[233] Ryder, M. R.; Civalleri, B.; Tan, J.-C. *Phys. Chem. Chem. Phys.* **2016**, *18*, 9079–9087.

[234] Bennett, T. D.; Cheetham, A. K.; Fuchs, A. H.; Coudert, F.-X. *Nat. Chem.* **2017**, *9*, 11–16.

[235] Born, M. *Math. Proc. Camb. Phil. Soc.* **1940**, *36*.

[236] Born, M.; Huang, K. *Dynamics Theory of Crystal Lattices*; Oxford University Press, Oxford, UK, 1954.

[237] Rehn, L. E.; Okamoto, P. R.; Pearson, J.; R.Bhadra,; Grimsditch, M. *Phys. Rev. Lett.* **1987**, *59*, 2987.

[238] Koike, J. *Phys. Rev. B* **1993**, *47*, 7700–7704.

[239] Gaillac, R.; Pullumbi, P.; Coudert, F.-X. *J. Phys.: Condens. Matter* **2016**, *28*, 275201.

[240] Lock, N.; Wu, Y.; Christensen, M.; Cameron, L. J.; Peterson, V. K.; Bridgeman, A. J.; Kepert, C. J.; Iversen, B. B. *J. Phys. Chem, ,* **2010**, *114*, 16181–16186.

[241] Bahr, D. F.; Reid, J. A.; Mook, W. M.; Bauer, C. A.; Stumpf, R.; Skulan, A. J.; Moody, N. R.; Simmons, B. A.; Shindel, M. M.; Allendorf, M. D. *Phys. Rev. B* **2007**, *76*, 184106.

[242] Banlusan, K.; Strachan, A. *J. Chem. Phys.* **2017**, *146*, 184705.

[243] Greathouse, J. A.; Allendorf, M. D. *J. Am. Chem. Soc.* **2006**, *128*, 10678–10679.

[244] Greathouse, J. A.; Allendorf, M. D. *J. Phys. Chem. C* **2008**, *112*, 5795–5802.

[245] Han, S. S.; III, W. A. G. *J. Phys. Chem. C* **2007**, *111*, 15185–15191.

[246] Tafipolsky, M.; Amirjalayer, S.; Schmid, R. *J. Comp. Chem.* **2007**, *28*, 1169–1176.

[247] Bristow, J. K.; Tiana, D.; Walsh, A. *J. Chem. Theory Comput.* **2014**, *10*, 4644–4652.

[248] Boyd, P. G.; Moosavi, S. M.; Witman, M.; Smit, B. *J. Phys. Chem. Lett.* **2017**, *8*, 357–363.

[249] Becker, T. M.; Heinen, J.; Dubbeldam, D.; Lin, L.-C.; Vlugt, T. J. H. *J. Phys. Chem. C* **2017**, *121*, 4659–4673.

[250] Dzubak, A. L.; Lin, L.-C.; Kim, J.; Swisher, J. A.; Poloni, R.; Maximoff, S. N.; Smit, B.; Gagliardi, L. *Nat. Chem.* **2012**, *4*, 810–816.

[251] Heinen, J.; Burtch, N. C.; Walton, K. S.; Fonseca Guerra, C.; Dubbeldam, D. *Chem. Eur. J.* **2016**, *22*, 18045–18050.

[252] Kulkarni, A. R.; Sholl, D. S. *J. Phys. Chem. C* **2016**, *120*, 23044–23054.

[253] Campbell, C.; Ferreiro-Rangel, C. A.; Fischer, M.; Gomes, J. R. B.; Jorge, M. *J. Phys. Chem. C* **2017**, *121*, 441–458.

[254] Sun, L.; Deng, W.-Q. *WIREs Comput. Mol. Sci.* **2017**, *7*, 1–15.

[255] James A. Schwarz, C. I. C. *Surfaces of Nanoparticles and Porous Materials*; CRC Press, 1999.

[256] *Proc. R. Soc. Lond. A Math. Phys. Sci.* **1924**, *106*, 463–477.

[257] Campa, C.; Mussard, B.; Woo, T. K. *J. Chem. Theory Comput.* **2009**, *5*, 2866–2878.

[258] Manz, T. A.; Sholl, D. S. *J. Chem. Theory Comput.* **2012**, *8*, 2844–2867.

[259] Hirshfeld, F. L. *Theor. Chim. Acta* **1977**, *44*, 129–138.

[260] Ewald, P. *Ann. Phys.* **1921**, *369*, 253287.

[261] Walton, K. S.; Millward, A. R.; Dubbeldam, D.; Frost, H.; Low, J. J.; Yaghi, O. M.; Snurr, R. Q. *J. Am. Chem. Soc.* **2008**, *130*, 406–407.

[262] Castillo, J. M.; Vlugt, T. J. H.; Calero, S. *J. Phys. Chem. C* **2008**, *112*, 15934–15939.

[263] Zheng, C.; Liu, D.; Yang, Q.; Zhong, C.; Mi, J. *Ind. Eng. Chem. Res.* **2009**, *48*, 10479–10484.

[264] Hamad, S.; Balestra, S. R.; Bueno-Perez, R.; Calero, S.; Ruiz-Salvador, A. R. *J. Solid State Chem.* **2015**, *223*, 144–151.

[265] Rappe, A. K.; Goddard, W. A. *J. Phys. Chem.* **1991**, *95*, 3358–3363.

[266] Wilmer, C. E.; Snurr, R. Q. *Chem. Eng. J.* **2011**, *171*, 775 – 781.

[267] Bauer, B. A.; Patel, S. *Theor. Chem. Acc.* **2012**, *131*, 1153.

[268] Rogge, S.; Vanduyfhuys, L.; Ghysels, A.; Waroquier, M.; Verstraelen, T.; Maurin, G.; Van Speybroeck, V. *J. Chem. Theory Comput.* **2015**, *11*, 5583–5597.

[269] Feller, S. E.; Zhang, Y.; Pastor, R. W.; Brooks, B. R. *J. Chem. Phys.* **1995**, *103*, 4613–4621.

[270] Quigley, D.; Probert, M. I. J. *J. Chem. Phys.* **2004**, *120*, 11432–11441.

[271] Martyna, G. J.; Tobias, D. J.; Klein, M. L. *J. Chem. Phys.* **1994**, *101*, 4177–4189.

[272] Martyna, G. J.; Tuckerman, M. E.; Tobias, D. J.; Klein, M. L. *Mol. Phys.* **1996**, *87*, 1117–1157.

[273] Berendsen, H. J. C.; Postma, J. P. M.; van Gunsteren, W. F.; DiNola, A.; Haak, J. R. *J. Chem. Phys.* **1984**, *81*, 3684–3690.

[274] Garcia-Perez, E.; Serra-Crespo, P.; Hamad, S.; Kapteijn, F.; Gascon, J. *Phys. Chem. Chem. Phys.* **2014**, *16*, 16060–16066.

[275] Zhao, L.; Yang, Q.; Ma, Q.; Zhong, C.; Mi, J.; Liu, D. *J. Mol. Model.* **2011**, *17*, 227–234.

[276] Ghoufi, A.; Subercaze, A.; Ma, Q.; Yot, P.; Ke, Y.; Puente-Orench, I.; Devic, T.; Guillerm, V.; Zhong, C.; Serre, C.; Frey, G.; Maurin, G. *J. Phys. Chem. C* **2012**, *116*, 13289–13295.

[277] Schenk, M.; Vlugt, T. *J. Phys. Chem. B* **2002**, *106*, 12757–12763.

[278] Gee, J. A.; Sholl, D. S. *J. Phys. Chem. C* **2016**, *120*, 370–376.

[279] Shi, W.; Maginn, E. J. *J. Chem. Theory Comput.* **2007**, *3*, 1451–1463.

[280] Torres Knoop, A.; Balaji, S. P.; Vlugt, T. J. H.; Dubbeldam, D. *J. Chem. Theory Comput.* **2014**, *10*, 942–952.

[281] Chempath, S.; Clark, L. A.; Snurr, R. Q. *J. Chem. Phys.* **2003**, *118*, 7635–7643.

[282] Duane, S.; Kennedy, A.; Pendleton, B. J.; Roweth, D. *Phys. Lett. B* **1987**, *195*, 216–222.

[283] Martin, M. G.; ; Siepmann, J. I. *J. Phys. Chem. B* **1998**, *102*, 2569–2577.

[284] Martin, M. G.; Siepmann, J. I. *J. Phys. Chem. B* **1999**, *103*, 4508–4517.

[285] Jorgensen, W. L.; Tirado-Rives, J. *J. Am. Chem. Soc.* **1988**, *110*, 1657–1666.

[286] Jorgensen, W. L.; Maxwell, D. S.; Tirado-Rives, J. *J. Am. Chem. Soc.* **1996**, *118*, 11225–11236.

[287] Allinger, N. L.; Yuh, Y. H.; Lii, J. H. *J. Am. Chem. Soc.* **1989**, *111*, 8551–8566.

[288] Demontis, P.; Suffritti, G. B.; Quartieri, S.; Fois, E. S.; Gamba, A. *J. Phys. Chem.* **1988**, *92*, 867–871.

[289] Nicholas, J. B.; Hopfinger, A. J.; Trouw, F. R.; Iton, L. E. *J. Am. Chem. Soc.* **1991**, *113*, 4792–4800.

[290] Hill, J.-R.; Sauer, J. *J. Phys. Chem.* **1995**, *99*, 9536–9550.

[291] Bush, T. S.; Gale, J. D.; Catlow, C. R. A.; Battle, P. D. *J. Mater. Chem.* **1994**, *4*, 831–837.

[292] Bueno-Pérez, R.; Calero, S.; Dubbeldam, D.; Ania, C. O.; Parra, J. B.; Zaderenko, A. P.; Merkling, P. J. *J. Phys. Chem. C* **2012**, *116*, 25797–25805.

[293] Huang, L.; Wang, H.; Chen, J.; Wang, Z.; Sun, J.; Zhao, D.; Yan, Y. *Micropor. Mesopor. Mat.* **2003**, *58*, 105–114.

[294] Dauber-Osguthorpe, P.; Roberts, V. A.; Osguthorpe, D. J.; Wolff, J.; Genest, M.; Hagler, A. T. *Proteins: Struct., Funct., Bioinf.* **1988**, *4*, 31–47.

[295] Eddaoudi, M.; Kim, J.; Rosi, N.; Vodak, D.; Wachter, J.; Keeffe, M. O.; Yaghi, O. *Science* **2002**, *295*, 469–472.

[296] Rowsell, J. L. C.; Spencer, E. C.; Eckert, J.; Howard, J. A. K.; Yaghi, O. M. *Science* **2005**, *309*, 1350–1354.

[297] Dubbeldam, D.; Krishna, R.; Snurr, R. Q. *J. Phys. Chem. C* **2009**, *113*, 19317–19327.

[298] Clegg, W.; Harbron, D. R.; Homan, C. D.; Hunt, P. A.; Little, I. R.; Straughan, B. P. *Inorg. Chim. Acta.* **1991**, *186*, 51–60.

[299] Ming-cai, Y.; Chi-wei, W.; Chang-chun, A.; Liang-jie, Y.; Ju-tang, S. *Wuhan Univ. J. Nat. Sci.* **2004**, *9*, 939–942.

[300] Hermes, S.; Schroder, F.; Amirjalayer, S.; Schmid, R.; Fischer, R. A. *J. Mater. Chem.* **2006**, *16*, 2464–2472.

[301] Vanduyfhuys, L.; Verstraelen, T.; Vandichel, M.; Waroquier, M.; Van Speybroeck, V. *J. Chem. Theory Comput.* **2012**, *8*, 3217–3231.

[302] Zhou, W.; Wu, H.; Yildirim, T.; Simpson, J. R.; Walker, A. R. H. *Phys. Rev. B* **2008**, *78*, 054114.

[303] Samanta, A.; Furuta, T.; Li, J. *J. Chem. Phys.* **2006**, *125*, 084714.

[304] Vanduyfhuys, L.; Vandenbrande, S.; Verstraelen, T.; Schmid, R.; Waroquier, M.; Van Speybroeck, V. *J. Comput. Chem.* **2015**, *36*, 1015–1027.

[305] Bureekaew, S.; Amirjalayer, S.; Tafipolsky, M.; Spickermann, C.; Roy, T. K.; Schmid, R. *Phys. Status Solidi B* **2013**, *250*, 1128–1141.

[306] Tafipolsky, M.; Schmid, R. *J. Phys. Chem. B* **2009**, *113*, 1341–1352.

[307] Addicoat, M. A.; Vankova, N.; Akter, I. F.; Heine, T. *J. Chem. Theory Comput.* **2014**, *10*, 880–891.

[308] Coupry, D. E.; Addicoat, M. A.; Heine, T. *J. Chem. Theory Comput.* **2016**, *12*, 5215–5225.

[309] Rappe, A. K.; Casewit, C. J.; Colwell, K. S.; Goddard, W. A.; Skiff, W. M. *J. Am. Chem. Soc.* **1992**, *114*, 10024–10035.

[310] Chung, Y. G.; Camp, J.; Haranczyk, M.; Sikora, B. J.; Bury, W.; Krungleviciute, V.; Yildirim, T.; Farha, O. K.; Sholl, D. S.; Snurr, R. Q. *Chem. Mater.* **2014**, *26*, 6185–6192.

[311] Bristow, J. K.; Skelton, J. M.; Svane, K. L.; Walsh, A.; Gale, J. D. *Phys. Chem. Chem. Phys.* **2016**, *18*, 29316–29329.

[312] J.Heinen,; Burtch, N. C.; Walton, K. S.; Dubbeldam, D. *J. Chem. Theory Comput.* **2017**, *13*, 3722–3730.

[313] Gasteiger, J.; Marsili, M. *Tetrahedron Lett.* **1978**, *19*, 3181–3184.

[314] Gasteiger, J.; Marsili, M. *Tetrahedron* **1980**, *36*, 3219–3228.

[315] Munn, A. S.; Pillai, R. S.; Biswas, S.; Stock, N.; Maurin, G.; Walton, R. I. *Dalton Trans.* **2016**, *45*, 4162–4168.

[316] Heinen, J.; Dubbeldam, D. *Dalton Trans.* **2016**, *45*, 4309–4315.

[317] Grosch, J. S.; Paesani, F. *J. Am. Chem. Soc.* **2012**, *134*, 4207–4215.

[318] Burtch, N. C.; Jasuja, H.; Dubbeldam, D.; Walton, K. S. *J. Am. Chem. Soc.* **2013**, *135*, 7172–7180.

[319] Demuynck, R.; Rogge, S. M. J.; Vanduyfhuys, L.; Wieme, J.; Waroquier, M.; Van Speybroeck, V. *J. Chem. Theory Comput.* **2017**, *13*, 5861–5873.

[320] Zimmerman, J. A.; WebbIII, E. B.; Hoyt, J. J.; Jones, R. E.; Klein, P. A.; Bammann, D. J. *Model. Simul. Mater. Sci. Eng.* **2004**, *12*, S319.

[321] Clausius, R. *Phil. Mag.* **1870**, *40*, 122–127.

[322] Tsai, D. H. *J. Chem. Phys.* **1979**, *70*, 1375–1382.

[323] Sun, Z. H.; Wang, X. X.; Soh, A. K.; Wu, H. A. *Model. Simul. Mater. Sci. Eng.* **2006**, *14*, 423.

[324] Hardy, R. J. *J. Chem. Phys.* **1982**, *76*, 622–628.

[325] Zimmerman, J. A.; Bammann, D. J.; Gao, H. *Int. J. Solids Struct.* **2009**, *46*, 238–253.

[326] Munn, R. W. *J. Phys. C: Solid State Phys.* **1972**, *5*, 535–542.

[327] Wang, Y.; Wang, J. J.; Zhang, H.; Manga, V. R.; Shang, S. L.; Chen, L.-Q.; Liu, Z.-K. *J. Phys.: Condens. Matter* **2010**, *22*, 225404.

[328] McCall, J. *J. Comput. Appl. Math.* **2005**, *184*, 205–222.

[329] Li, Y.; Li, H.; Pickard, F. C.; Narayanan, B.; Sen, F. G.; Chan, M. K. Y.; Sankaranarayanan, S. K. R. S.; Brooks, B. R.; Roux, B. *J. Chem. Theory Comput.* **2017**, *13*, 4492–4503.

[330] Evans, J. D.; Coudert, F.-X. *Chem. Mater.* **2017**, *29*, 7833–7839.

[331] Evans, J. D.; Huang, D. M.; Haranczyk, M.; Thornton, A. W.; Sumby, C. J.; Doonan, C. J. *CrystEngComm* **2016**, *18*, 4133–4141.

[332] Li, Z.; Kermode, J. R.; De Vita, A. *Phys. Rev. Lett.* **2015**, *114*, 096405.

[333] Huan, T. D.; Batra, R.; Chapman, J.; Krishnan, S.; Chen, L.; Ramprasad, R. *npj comput. mater.* **2017**, *3*, 37.

[334] Bowen, J.; Allinger, N. In *Rev. Comp. Ch.*; Lipkowitz, K., Boyd, D. B., Eds.; Wiley Online Library: New Jersey, USA, 1991; Vol. 2; pp 81–97.

[335] Tafipolsky, M.; Schmid, R. *J. Phys. Chem. B* **2009**, *113*, 1341–1352.

[336] Grosch, J. S.; Paesani, F. *J. Am. Chem. Soc.* **2012**, *134*, 4207–4215.

[337] Bureekaew, S.; Amirjalayer, S.; Tafipolsky, M.; Spickermann, C.; Roy, T. K.; Schmid, R. *Phys. Status Solidi (b)* **2013**, *250*, 1128–1141.

[338] Gale, J.; Rohl, A. *Mol. Simul.* **2003**, *29*, 291–341.

[339] Barthelet, K.; Marrot, J.; Riou, D.; Frey, G. *Angew. Chem. Int. Ed.* **2002**, *41*, 281–284.

[340] Yot, P. G.; Ma, Q.; Haines, J.; Yang, Q.; Ghoufi, A.; Devic, T.; Serre, C.; Dmitriev, V.; Ferey, G.; Zhong, C.; Maurin, G. *Chem. Sci.* **2012**, *3*, 1100–1104.

[341] Le Page, Y.; Saxe, P. *Phys. Rev. B* **2002**, *65*, 104104.

[342] Perdew, J. P.; Burke, K.; Ernzerhof, M. *Phys. Rev. Lett.* **1996**, *77*, 3865–3868.

[343] Vanpoucke, D. E. P.; Lejaeghere, K.; Van Speybroeck, V.; Waroquier, M.; Ghysels, A. *J. Phys. Chem. C* **2015**, *119*, 23752–23766.

[344] Mouhat, F.; Coudert, F.-X. *Phys. Rev. B* **2014**, *90*, 224104.

[345] Wieme, J.; Vanduyfhuys, L.; Rogge, S. M. J.; Waroquier, M.; Speybroeck, V. V. *J. Phys. Chem. C* **2016**, *120*, 14934–14947.

[346] Garcia-Perez, E.; Serra-Crespo, P.; Hamad, S.; Kapteijn, F.; Gascon, J. *Phys. Chem. Chem. Phys.* **2014**, *16*, 16060–16066.

[347] Dubbeldam, D.; Walton, K. S. In *Materials Modeling towards Engineering Applications*; Jiang, J., Ed.; Pan Stanford Publishing Pte Ltd., 2015.

[348] Kopelevich, D.; Chang, H. *J. Chem. Phys.* **2001**, *114*, 3776–3789.

[349] Ford, D. C.; Dubbeldam, D.; Snurr, R. Q. *Diffus. Fundam. III* **2009**, *11*, 1–8.

[350] Parkes, M. V.; Demir, H.; Teich-McGoldrick, S. L.; Sholl, D. S.; Greathouse, J. A.; Allendorf, M. D. *Micropor. Mesopor. Mat.* **2014**, *194*, 190–199.

[351] Potoff, J. J.; Siepmann, J. I. *AIChE J.* **2001**, *47*, 1676–1682.

[352] Clark, L. A.; Snurr, R. Q. *Chem. Phys. Lett.* **1999**, *308*, 155–159.

[353] Bourrelly, S.; Llewellyn, P. L.; Serre, C.; Millange, F.; Loiseau, T.; Férey, G. *J. Am. Chem. Soc.* **2005**, *127*, 13519–13521.

[354] Gándara, F.; Bennett, T. D. *IUCrJ* **2014**, *1*, 563–570.

[355] Bundschuh, S.; Kraft, O.; Arslan, H. K.; Gliemann, H.; Weidler, P. G.; Wll, C. *Appl. Phys. Lett.* **2012**, *101*, 101910.

[356] Sun, Y.; Hu, Z.; Zhao, D.; Zeng, K. *ACS Appl. Mater. Interfaces* **2017**, *9*, 32202–32210.

[357] Zeng, Z.; Tan, J.-C. *ACS Appl. Mater. Interfaces* **2017**, *9*, 39839–39854.

[358] Oliver, W.; Pharr, G. *J. Mater. Res.* **1992**, *7*, 1564–1583.

[359] Evans, J. S. O.; David, W. I. F.; Sleight, A. W. *Acta Crystallogr. B* **1999**, *55*, 333–340.

[360] Drymiotis, F. R.; Ledbetter, H.; Betts, J. B.; Kimura, T.; Lashley, J. C.; Migliori, A.; Ramirez, A. P.; Kowach, G. R.; Van Duijn, J. *Phys. Rev. Lett.* **2004**, *93*, 025502.

[361] Andrews, J. P. *Proc. Phys. Soc. London* **1924**, *37*, 169.

[362] Kimball, A. L.; Lovell, D. E. *Phys. Rev.* **1925**, *26*, 121–124.

[363] Wachtman, J. B.; Tefft, W. E.; Lam, D. G.; Apstein, C. S. *Phys. Rev.* **1961**, *122*, 1754–1759.

[364] Ledbetter, H. *Mater. Sci. Eng. A* **2006**, *442*, 31–34.

[365] Menard, K. P. *Dynamic Mechanical Analysis: A Practical Introduction*; CRC Press, 1999.

[366] Venkatasubramanian, A.; Lee, J.-H.; Stavila, V.; Robinson, A.; Allendorf, M. D.; Hesketh, P. J. *Sens. Actuator B-Chem.* **2012**, *168*, 256–262.

[367] Ramamurty, U.; Jang, J.-i. *CrystEngComm* **2014**, *16*, 12–23.

[368] Tovar, T. M.; Zhao, J.; Nunn, W. T.; Barton, H. F.; Peterson, G. W.; Parsons, G. N.; LeVan, M. D. *J. Am. Chem. Soc.* **2016**, *138*, 11449–11452.

[369] Walton, K. S.; Snurr, R. Q. *J. Am. Chem. Soc.* **2007**, *129*, 8552–8556.

[370] Schlichte, K.; Kratzke, T.; Kaskel, S. *Microp. Mesopor. Mat.* **2004**, *73*, 81–88.

[371] Watanabe, T.; Sholl, D. S. *J. Chem. Phys.* **2010**, *133*, 094509.

[372] Nosé, S. *J. Chem. Phys.* **1984**, *81*, 511–519.

[373] Hoover, W. G. *Phys. Rev. A* **1985**, *31*, 1695–1697.

[374] Workum, K. V.; Gao, G.; Schall, J. D.; Harrison, J. A. *J. Chem. Phys.* **2006**, *125*, 144506.

[375] Anderson, O. L. *Phys. Rev.* **1966**, *144*, 553–557.

List of publications

1. J. Heinen, D. Dubbeldam and C. Fonseca Guerra, Kohn-Sham Molecular Orbital Analysis of the Coordination Bond in Anhydrous and Hydrated HKUST-1, *In preparation*, **2018**

2. J. Lahnsteiner, G. Kresse, J. Heinen, M. Bokdam, The Finite Temperature Structure of the MAPbI3 Perovskite: Comparing Density Functional Approximations and Force Fields to Experiment, *Physical Review Materials*, **2018**, 2, 073604

3. N.C. Burtch, C.R. Morelock, Y. Jiao, J. Heinen, J.T. Hungerford, A.A. Yakovenko, W. Xu, D. Dubbeldam, K.S. Walton, In Situ Visualization of Loading-Dependent Water Effects in a Stable Metal-Organic Framework, *Under revision*, **2018**

4. J. Heinen, A.D. Ready, T.D. Bennett, D. Dubbeldam, R.W. Friddle and N.C. Burtch, Elucidating the Temperature-Dependent Mechanical Properties of the Negative Thermal Expansion Metal-Organic Framework, *ACS Applied Materials & Interfaces*, **2018**, 10, 21079-21083

5. J. Heinen and D. Dubbeldam, On Flexible Force Fields for Metal-Organic Frameworks: Recent Developments and Future Prospects, *WIREs Computational Molecular Science*, **2018**, 8, e1363

6. N.C. Burtch, J. Heinen, T.D. Bennett, D. Dubbeldam and M.D. Allendorf, Mechanical Properties in Metal-Organic Frameworks: Emerging Opportunities and Challenges for Device Functionality and Technological Applications, *Advanced Materials*, **2017**, 1704124

7. J. Heinen, N.C. Burtch, K.S. Walton and D. Dubbeldam, Flexible Force Field Parameterization through Fitting on the Ab Initio derived Elastic Tensor, *Journal of Chemical Theory and Computation* **2017**, 13, 3722-3730

8. T.M. Becker, J. Heinen, D. Dubbeldam, L. Lin, and T.J.H. Vlugt, Polarizable Force Fields for CO_2 and CH_4 Adsorption in M-MOF-74, *Journal of Physical Chemistry C*, **2017**, 121, 4659-4673

9. J. Heinen, N.C. Burtch, K.S. Walton, C. Fonseca Guerra and D. Dubbeldam, Predicting Multicomponent Adsorption Isotherms in Open-Metal Site Materials using Force Field Calculations based on Energy Decomposed Density Functional Theory, *Chemistry - A European Journal*, **2016**, 22, 18045-18050

10. J. Heinen and D. Dubbeldam, Understanding and Solving Disorder in Substitution Pattern of Amino Functionalized MIL-47(V), *Dalton Transactions*, **2016**, 45, 4309-4315

11. A. Torres Knoop, J. Heinen, R. Krishna, and D. Dubbeldam, Entropic Separation of Styrene/Ethylbenzene Mixtures by Exploitation of Subtle Differences in Molecular Configurations in Ordered Crystalline Nanoporous Adsorbents, *Langmuir*, **2015**, 31, 3771-3778

Acknowledgments

Nu het proefschrift afgerond is wil ik graag een aantal mensen bedanken.

Allereerst wil ik mijn dagelijkse begeleider David bedanken. Ik heb erg dankbaar om een begeleider zoals jij te mogen hebben. Je hebt me elke kans geboden om mijn onderzoek in richten zoals ik dat wou. Mijn kennis is enorm toegenomen de afgelopen jaren. Elke wetenschapper zou een voorbeeld moeten nemen aan jouw nuchterheid. De wetenschappelijke en minder wetenschappelijke discussies tijdens de KFC-lunches waren altijd erg goed! Ten tweede wil ik mijn promotor Evert Jan bedanken voor alle hulp en begeleiding tijdens zowel mijn promotie als mijn studie. Sinds mijn tweede jaar van mijn scheikundestudie ben ik aan de Computational Chemistry group blijven plakken. Dankzij jou was het ook mogelijk om mijn afstudeerstage bij Albemarle Catalysts te doen. Hier heb ik tevens het genoegen gehad om onder de begeleiding van Jaap te mogen werken.

Ariana, besides doing some projects together and experiencing the Georgia Tech culture, I am very grateful that you were my mentor in the early stages of my PhD. Speaking of Georgia Tech: Krista, thank you for hosting me in your group. I really enjoyed the Southern hospitality.

My research stays in the USA would not have been possible without Nick. Nick, it has been a privilege to work with you. I have learned a lot from you and I am very grateful that you gave me twice the opportunity to come to Sandia.

My project at Sandia could not been successful without Austin and Ray. Austin, it was a pleasure to work with you and I am very confident that you will be a great scientist. Ray, thank you for your teachings on mechanical characterization and valuable discussions. Shout out to Andreas, Sam, Pavithra, Mathias and Ruben for having a nice time over there! Mark, thanks for the BBQ party at your place! Thomas, many thanks for your being involved in this project and your valuable input.

Célia, ik wil je heel erg bedanken voor onze quantumchemie-samenwerking en vele interessante discussies. Ik heb erg veel van je geleerd. Also, a big thanks to my fellow quantum chemistry teaching assistents Stephanie and Sara. I think we made a great team!

A PhD life is not complete without colleagues. Throughout the years, I have met many nice 'MolSimmers'. Specifically, the trip to Porto with some of you will have long-lasting memories. Peter, Bernd and Jocylene, it is always nice to talk with all of you about (non)-scientific topics! Arthur, jou ken ik het langst en vele (South Park) herinneringen zullen me bijblijven (oooh I Member). The Indian quintet: Adithya, Ambuj, Arjun, Nitish and Rakesh. You guys really made the group more dynamic but do remember that I played in a movie with Shahrukh Khan. To the computational polymer girls, Verena and Yuliia: although your backgrounds are in physics and mathematics, you are now officially chemists! Luckily, I also had nice office mates Albertoooo, Ivan, Sander and Eva. Thanks for tolerating me and for the many nice discussions about, usually, random stuff. Also, thanks to David S. for comments on my summary and your legen... wait for it...dary presentations.

Thijs, although we didn't collaborate intensively, I always felt very welcome at your group in Delft. Ali and Tim, we started our PhD journey together and I am looking forward to your PhD defenses. Shout-out to the other Delftenaren: Sayed, Reza, Noura, Sebastian, Martijn, Mahinder, Remco, Christos, Hirad and Mate.

Due to personal circumstances, I was frequently in Vienna. Luckily, I was adopted very soon by several computational physicists. Menno, Jonathan and Martijn, thank you for hosting me once in a while.

Een belangrijk onderdeel van deze reis zijn de mensen die ik tijdens mijn studie heb ontmoet. Met name het scheikunde cohort 2009/2010: Lukas, Sven, Abel, Martijn en Tom. Met jullie erbij was de studie en het promotie-onderzoek een stuk aangenamer! Behalve het cohort 2009/2010, heb ik veel andere mensen mogen leren kennen: Nikki, Kasper, Chu Chu, Rolf, Tessel, Rebecca, Tommy, Christiaan, en Stijn. Het is altijd zeer gezellig met jullie!

Desondanks dat het alweer negen jaar sinds ieder zijn eigen weg opging ben ik altijd blij als we met de SNL-groep weer bij elkaar zijn. Matthias, Mark, Peter, Alex, Oliver en Raph, thanks voor lange vriendschap.

Uiteraard ook dank aan mijn UCT-familie. Sommigen van jullie ken ik al meer dan 15 jaar en dat schept speciale banden. Met name, Sifu Wai, wil ik bedanken voor zijn jarenlange support en vriendschap.

Pa en ma, bedankt voor al jullie steun, interesse en liefde de afgelopen jaren. Het voelt altijd erg fijn om weer 'thuis' te kunnen komen bij jullie. Kars, ik ben altijd erg onder de indruk geweest van je RoboCup-wedstrijden en van je afstudeeropdracht. Het is tof om een broer te hebben die veel slimmer is dan ik.

Claire, het belangrijkste wat ik de afgelopen jaren heb gekregen is jouw liefde en oneindige steun. Ik kijk erg uit naar onze avondturen in het buitenland danwel in Nederland.